THE UNIVERSITY OF CHICAGO

FRAGMENTATION-BASED QUANTUM CHEMISTRY ON CLASSICAL AND QUANTUM COMPUTERS

A DISSERTATION SUBMITTED TO
THE FACULTY OF THE DIVISION OF THE PHYSICAL SCIENCES
IN CANDIDACY FOR THE DEGREE OF
DOCTOR OF PHILOSOPHY

DEPARTMENT OF CHEMISTRY

BY
ABHISHEK MITRA

CHICAGO, ILLINOIS
AUGUST 2024

Dedicated to my parents, for their endless love, support, and belief in me.

TABLE OF CONTENTS

LIST OF FIGURES

LIST OF TABLES

ACKNOWLEDGMENTS

Firstly, I would like to express my deepest gratitude to my research advisor, Professor Laura Gagliardi, for her outstanding guidance and constant support throughout my entire PhD journey. I am particularly grateful to Laura for encouraging me to tackle the most challenging problems, to think creatively while critically evaluating my own ideas, and to always consider the broader scientific impact of my work. She has consistently motivated me to broaden my scientific horizons and explore new frontiers in solving theoretical chemistry problems. Laura has provided me with exciting opportunities that have allowed me to interact with individuals both within and outside my area of expertise, thereby solidifying and extending my scientific understanding and helping me develop as a scientist. Finally, I would like to thank Laura for introducing me to the world of method development in quantum chemistry and, most recently, for guiding me into doing so using quantum computing architecture.

I would now like to thank my co-advisor, Dr. Stephen Gray, at the Argonne Chemical Laboratory. Stephen has not only been an exceptional scientific advisor in our collaborative quantum computing project but has also been instrumental in helping me explore career opportunities. He has proven to be a vast resource, and I continually learn something new in each of our discussions. For this, I am immensely grateful.

I would like to thank my committee members, Prof. Laura Gagliardi, Prof. David Mazziotti, and Prof. Giulia Galli, for their time, feedback on my research, and advice on future career steps. I am thankful to collaborate with Prof. Galli on an exciting project, and I hope to collaborate with Prof. Mazziotti in the future.

I would like to thank Hung Pham for being a wonderful mentor during the first year of my PhD. He introduced me to the PySCF software and taught me about quantum embedding, especially during 2019-2020 when COVID-19 severely affected in-person communication. Hung has been one of my closest friends and an important mentor ever since. I would also like to thank Prachi Sharma for mentoring me in my first year, teaching me about

multireference quantum chemistry, and introducing me to the OpenMolcas software. Prachi has also remained a close friend and mentor throughout my PhD. I want to thank Debmalya Ray for his mentorship during my initial days. I am grateful to have had such amazing group members and friends.

I want to thank Dr. Matthew Hermes, a staff scientist in the Gagliardi Group, for helping me understand basic scientific concepts, develop coding and technical skills, and cultivate critical thinking during my entire PhD. Matt has been a great scientist to work with, and I am fortunate that he has been a coauthor on seven of my published papers. Additionally, I would like to thank Paul Calio, Gautam Stroscio, Thais Scott, Ruhee D Cunha, Silvia Escayola, Soumi Haldar, Shreya Verma, Joanna Wang, and Riddhish Pandharkar for teaching me various concepts and helping me improve my skills. I also thank Soumi, Shreya, Ruhee, Joanna, and Riddhish for being collaborators.

Next, I want to acknowledge my other incredible collaborators: Yuri Alexeev, Matthew Otten, Francesca Fasulo, Ana B. Muñoz-García, Michele Pavone, Yu Jin, Christian Vorwerk, Minsik Cho, Valay Agarwal, Sandra M. Ciborowski, Rachel M. Harris, Gaoxiang Liu, Navneet Khetrapal, Moritz Blankenhorn, and Kit H. Bowen. Without their support, this thesis would not have been possible.

Next, I would like to thank my undergraduate supervisor, Professor Upakarasamy Lourderaj, for introducing me to computational chemistry and for encouraging, supporting, and mentoring me throughout my career.

I want to thank my wonderful friends, Arghya Sarkar, Manas Bharadwaj, Sharba Bhattacharya, Nishant Sharma, Dipanshu Roy, Shahzad Alam, Bidisha Sarkar, Adrian Gordon, Jacob Schaffner, Zhihao Wu, Eduardo Medina, Antara Ray, Ayana Bhattacharya, Riddhi Datta, Rijul Guha Neogi, Shramana Brahma, and Sahana Deb, for being there in my life.

I want to thank my amazing partner, Irma Avdić, for her support, guidance, and for always being there through thick and thin during the last two years of my PhD. Without

her, this thesis would not have been possible. Lastly, I want to thank my parents, Amitava and Aparna, for their love, support, and encouragement throughout all these years and for helping me come to where I am today.

ABSTRACT

The development of electronic structure methods is essential for understanding the properties of molecules and materials, thereby advancing materials and drug discovery. Over the past century, numerous electronic structure methods have been developed, though the most accurate ones often suffer from poor scalability with system size, limiting their application to moderate-sized molecules and extended materials.

Quantum embedding offers a promising solution by fragmenting the system into smaller, chemically relevant pieces and applying the accurate, computationally expensive methods only on the chemically important fragments. In this thesis, we discuss the development and application of quantum embedding methods that significantly reduce computational costs, in terms of computational time and memory, using both classical and quantum computing resources. Using illustrative examples, we show that these approaches make certain calculations possible that were previously impractical with conventional electronic structure methods.

Chapter 1 of this thesis presents a review of the fundamentals of electronic structure theory relevant to this work and provides a general outline for the rest of the thesis. In chapters 2 and 4, we will discuss methods developed using density matrix embedding techniques and strongly correlated electronic structure theories to study excited states of defects in extended solids, which are essential for the discovery of solid-state qubits and in heterogeneous catalysis applications. In chapter 3, we extend our quantum embedding framework with weakly correlated electronic structure theories to study surface adsorption through which we develop memory-efficient techniques that lead to savings in computational memory of handling larger fragment sizes. In chapter 5, we develop a quantum computing algorithm based on the localized active space self-consistent field (LASSCF) method that significantly reduces resource requirements for quantum computers as needed for application on noisy intermediate-scale quantum devices. Finally, in chapter 6, we present an application of multireference methods

in studying metal-metal bonding in uranium dimers.

These methods enable more extensive calculations on moderate to large molecules and materials, providing a framework for the future development of accurate electronic structure methods at a manageable cost.

CHAPTER 1

INTRODUCTION

Electronic structure calculations on classical and quantum computers are essential for understanding and determining the properties of molecules and materials. These properties are often difficult to measure experimentally but are important for advancing research in heterogeneous catalysis, drug discovery, and materials discovery. This thesis is concerned with the development and applications of fragment-based electronic structure methods that enhance the applicability of conventional accurate methods to larger system sizes as is important in the aforementioned fields using both quantum and classical hardware.

In this chapter, we will briefly describe the many-electron problem, which is the central reason that necessitates the development of electronic structure methods. We will introduce the general tools required to understand the formalism of electronic structure methods. Next, we will briefly describe some of the most popular electronic structure theories and discuss their limitations in terms of computational cost.

Finally, we will discuss the concept of quantum embedding, which introduces the idea of a fragmentation-based scheme to enhance the affordability of modern electronic structure methods. This will be followed by a brief discussion on our developments concerning the development of quantum embedding and active space fragmentation methods for treating strongly correlated ground and excited states for materials discovery using classical and futuristic quantum hardware.

1.1 The Many-Electron Problem

The fundamental idea of electronic structure calculations involves employing quantum mechanics to analyze interactions among electrons. This is done by representing the quantum mechanical system of interest in terms of a wavefunction and obtaining solutions to the non-

relativistic, time-independent many-body Schrödinger equation[2]. The Schrödinger equation for any system is given in Equation 1.1:

$$\hat{H}\mathbf{\Psi}(\mathbf{r}) = E\mathbf{\Psi}(\mathbf{r}) \tag{1.1}$$

Here, $\mathbf{\Psi}(\mathbf{r})$ is the wavefunction for the system, $\hat{H}(r)$ is the Hamiltonian operator, and E is the energy eigenvalue. For a molecule with N electrons and n nuclei, the non-relativistic, time-independent Hamiltonian operator can be represented as shown in Equation 1.2.

$$H = -\sum_{i=1}^{N}\frac{1}{2}\nabla_i^2 - \sum_{a=1}^{n}\frac{1}{2M_a}\nabla_a^2 - \sum_{i=1}^{N}\sum_{a=1}^{n}\frac{Z_a}{r_{ia}} + \sum_{i=1}^{N}\sum_{j>i}^{N}\frac{1}{r_{ij}} + \sum_{a=1}^{n}\sum_{b>a}^{n}\frac{Z_a Z_b}{R_{ab}} \tag{1.2}$$

Here, M_a is the mass of a nucleus, Z_b and Z_a are the atomic numbers of nuclei a and b respectively, r_{ij} gives the distance between electrons i and j, r_{ia} gives the distance between electron i and nucleus a, and R_{ab} gives the distance between nuclei a and b. The first and second terms represent the kinetic energy operators for the electrons and nuclei respectively. The third term gives the electron-nuclei potential term. The fourth and fifth terms represent the electron-electron and nuclei-nuclei Coulombic repulsion terms, respectively. Even after assuming the nuclei to be point particles and ignoring relativistic effects, the molecular Hamiltonian remains extremely difficult to solve[3]. The Born-Oppenheimer (BO) approximation[4,5] further allows us to decouple the nuclear degrees of freedom from the electronic ones. This approximation is valid for many applications where the motion of the electrons is much faster than that of the nuclei.

$$H_{elec} = -\sum_{i=1}^{N}\frac{1}{2}\nabla_i^2 - \sum_{i=1}^{N}\sum_{a=1}^{n}\frac{Z_a}{r_{ia}} + \sum_{i=1}^{N}\sum_{j>i}^{N}\frac{1}{r_{ij}} + h_{nuc} \tag{1.3}$$

Solving these differential equations can give us the exact many-electron wavefunction. The Schrödinger equation, however, can be solved exactly only for a one-electron system[6]. For

a many-electron system, the explicit evaluation of the electron-electron interaction term poses a problem and hence the Schrödinger equation can only be solved approximately. This electron-electron interaction, however, is crucial for predicting properties with high accuracy. Over the years, significant progress has been made in this area and has resulted in the development of sophisticated electronic structure methods to account for these electron-electron interaction effects. Most of the advanced wavefunction-based theories are built upon the Hartree-Fock (HF) approximation, where only a mean-field model of the electron interaction is used. In this thesis, we will present methods and techniques that augment and enable the extension of some of these accurate electronic structure theories to extended systems using classical and quantum computing resources at an affordable computational cost.

Before doing so, we will briefly discuss the concepts of wavefunction, operators, and second quantization, which is important to start introducing modern electronic structure theories.

1.2 Wavefunctions, Operators, and Second Quantization

A many-electron wavefunction is generally represented by a single Slater Determinant (SD) or by a linear combination of SDs[7,8]. The construction of SDs ensures that these wavefunctions are anti-symmetric with respect to the exchange of two electrons[9]. A SD composed of N electrons in N spin-orbitals (χ) can be written as:

$$\Psi_{SD} = \frac{1}{\sqrt{N!}} \begin{pmatrix} \chi_1(1) & \chi_2(1) & \dots & \chi_{N-1}(1) & \chi_N(1) \\ \chi_1(2) & \chi_2(2) & \dots & \chi_{N-1}(2) & \chi_N(2) \\ \vdots & \vdots & \dots & \vdots & \vdots \\ \chi_1(N) & \chi_2(N) & \dots & \chi_{N-1}(N) & \chi_N(N) \end{pmatrix} \tag{1.4}$$

In second quantization[10,11], the wavefunctions are represented by the action of the creation ($a_P^\dagger$) and the annihilation operator (a_Q) on a vacuum state ($|vac\rangle$), where P and Q are

labels of the spin-orbitals. $a_P^\dagger$ creates an electron in the spin orbital ϕ_P and a_Q annihilates an electron from the spin orbital ϕ_Q. The general quantum mechanical operators are represented conveniently using the creation and annihilation operators. These operators obey anti-commutation relations as shown by the equations below:

$$a_P a_Q + a_Q a_P = 0 \tag{1.5}$$

$$a_P^\dagger a_Q^\dagger + a_Q^\dagger a_P^\dagger = 0 \tag{1.6}$$

$$a_P^\dagger a_Q + a_Q a_P^\dagger = \delta_{PQ} \tag{1.7}$$

Also, the annihilation operator acting on a vacuum state gives 0.

$$a_Q \left|vac\right\rangle = 0 \tag{1.8}$$

The antisymmetry of the wavefunction is incorporated by construction. A SD is represented as an occupation number vector (ONV) as shown in equation 1.9.

$$\left|k\right\rangle = \left|k_1, k_2, k_3 ... k_M\right\rangle \tag{1.9}$$

Here, where k_p is 1 for the occupied orbitals and 0 for the unoccupied orbitals. In second quantization, sequentially applying the creation operators on a vacuum state will generate a SD or a configuration.

$$\left|k\right\rangle = \left[\prod_{P=1}^{M} (a_P^+)^{k_p}\right] \left|vac\right\rangle \tag{1.10}$$

The spin-free, non-relativistic Hamiltonian operator[11] in second-quantization is thus represented as follows:

$$\hat{H} = \sum_{PQ} h_{PQ} a_P^+ a_Q + \frac{1}{2} \sum_{PQRS} g_{PQRS} a_P^+ a_R^+ a_S a_Q + h_{nuc} \tag{1.11}$$

where h_{nuc} is the nuclear repulsion term, a constant at a given nuclear geometry, and the one and two-electron integrals are defined as follows:

$$h_{PQ} = \int \phi_P^*(x) \left(-\frac{1}{2}\nabla^2 - \sum_l \frac{Z_l}{r_l} \right) \phi_Q(x) dx \tag{1.12}$$

$$g_{PQRS} = \int \int \frac{\phi_P^*(x_1)\phi_R^*(x_2)\phi_Q(x_1)\phi_S(x_2)}{r_{12}} dx_1 dx_2 \tag{1.13}$$

The wavefunction $|\psi\rangle$ is now expressed as a normalized linear combination of various ONVs (1.14).

$$|\psi\rangle = \sum_k c_k |k\rangle \tag{1.14}$$

where c_k is the coefficient of the ONV $|k\rangle$. The energy of this wavefunction, which is the expectation value of the Hamiltonian operator, can be calculated as

$$E_0 = \langle\psi| \hat{H} |\psi\rangle \tag{1.15}$$

Plugging equation 1.11 into the equation 1.15, the expectation value can be written in terms of the one and two body density matrices as:

$$\langle\psi| \hat{H} |\psi\rangle = \sum_{PQ} h_{PQ} \langle\psi| a_P^\dagger a_Q |\psi\rangle + \frac{1}{2} \sum_{PQRS} g_{PQRS} \langle\psi| a_P^\dagger a_R^\dagger a_S a_Q |\psi\rangle + h_{nuc} \tag{1.16}$$

with the one-body and two-body density matrices defined as:

$$D_{PQ} = \langle\psi|\, a_P^\dagger a_Q \,|\psi\rangle \tag{1.17}$$

$$d_{PQRS} = \langle\psi|\, a_P^\dagger a_R^\dagger a_S a_Q \,|\psi\rangle \tag{1.18}$$

One and two body density matrices can be used to calculate the expectation values of most operators[12]. The variational principle guarantees that the ground-state energy of a molecule can be obtained by minimizing the energy expression in equation 1.15 with respect to the coefficients of the wavefunction c_k[11].

Now we shall briefly discuss the Hartree-Fock (HF) method, one of the first and fundamental electronic structure methods, which approximates electron interaction through Coulomb and exchange energy terms.

1.3 The Hartree-Fock (HF) Approximation

The Hartree Fock (HF) wavefunction is represented by a single SD and the coefficients of the spin orbitals forming the SD are obtained variationally.

$$|\psi_{HF}\rangle = e^{-\hat{k}} \,|k_0\rangle \tag{1.19}$$

where $e^{-\hat{k}}$ is a unitary operator, $\hat{k}$ is an anti-Hermitian operator defined in terms of the anti-Hermitian matrix k_{PQ}, and $|\hat{k_0}\rangle$ is a reference configuration.

$$\hat{k} = \sum_{PQ} k_{PQ} a_P^\dagger a_Q \tag{1.20}$$

The ground state energy E_0^{HF} is the expectation value of the Hamiltonian operator using the ground state wave-function, $|\psi_{HF}\rangle$, and can be written as equation 1.16, by replacing the

one- and two-body density matrices with those derived for the Hartree-Fock approximations. The occupied orbitals are indicated by the indices i, j, k, and l, whereas the unoccupied orbitals are indicated by the indices a, b, c, and d.

$$D_{ij} = 2\delta_{ij} \tag{1.21}$$

$$d_{PQRS} = D_{ij}D_{kl} - \frac{1}{2}D_{il}D_{kj} = 4\delta_{ij}\delta_{kl} - 2\delta_{il}\delta_{kj} \tag{1.22}$$

Plugging equations 1.21 and 1.22 into 1.15, we get equation 1.23 which represents the total ground-state energy.

$$E_0^{HF} = \langle \psi_{HF} | \hat{H} | \psi_{HF} \rangle = h_{nuc} + 2\sum_i h_{ij} + \sum_{ij}(2g_{iijj} - g_{ijji}) \tag{1.23}$$

1.4 Electron Correlation

Although HF accounts for a large chunk of the total system energies, it overlooks some important electron correlation effects, which results in large errors in relative energy predictions such as binding energies or excitation energies. Nevertheless, it lays the groundwork for most modern electronic structure methods in the wavefunction domain. Extensive research efforts have been dedicated to accurately capturing this electron interaction beyond HF. This type of interaction, termed the electron correlation energy[13–20], is defined as the difference between the exact energy and the Hartree-Fock energy in a given basis or at the complete basis set limit (CBS). Although there is no precise method for defining the various types of electron correlation, researchers have conceptually separated various correlation effects like dynamical and static correlation, or long-range and short-range correlation[21–24]. We focus on the conceptual separation of electron correlation into static and dynamic terms. These categorizations arise from the challenges associated with accurately calculating electron correlation beyond the HF mean-field approximation. The first category, static, also referred to

as strong or non-dynamic correlation, stems from the inherent multi-configurational nature of the wavefunction, which HF does not account for. In this thesis, we will largely be focussing on chemical effects arising from static correlation. It occurs when multiple electron states that are close in energy influence each other, leading to energy splitting. These effects can be addressed by incorporating multiple configurations into the wavefunction, typically involving degenerate or near-degenerate states. Such strong correlation is important for describing transition-metal and heavy-metal chemistry, magnetic molecules, bond breaking, biradicals, excited states, and the functionality of various materials, and can give rise to exotic phenomena, such as superconductivity, where Cooper pairs form due to strongly correlated electrons[25], resulting in a significant drop in resistance when the material is cooled below a certain temperature. The second challenge is the instantaneous Coulombic repulsion between electrons, which the mean-field approximation fails to capture, known as dynamic correlation.

1.5 Electronic Structure Theories

Wavefunction-based methods such as coupled cluster (CC) and perturbation theories like second-order Møller-Plesset perturbation theory (MP2) have proven highly effective in approximating electron correlations, which are primarily dynamic and based on a single reference, such as HF. To address the challenges of static correlation, it is essential to include multiple configurations. Including all possible configurations results in the Full Configuration Interaction (FCI) method. However, the applicability of FCI is severely restricted by factorial scaling with system size, typically limited to 20 electrons in 20 orbitals[12]. Consequently, researchers have developed methods to include only relevant configurations, leading to multiconfiguration self-consistent field (MC-SCF) methods such as complete active space SCF (CASSCF)[26–28] and multireference configuration interaction (MRCI)[29,30]. These methods identify important configurations based on the number of electrons and orbitals in the "active

space" subjected to exact diagonalization. However, their applicability is further limited by factorial scaling with the size of the active space and by high polynomial scaling for the space subjected to variational optimization[12].

Furthermore, when dynamic correlation effects become significant for multireference states, multireference perturbation theories are invoked, which scale even more poorly. Thus, a major challenge in developing accurate wavefunction-based electronic structure theories is the computational scaling, which increases dramatically with system size, such as in modeling realistic molecules or extended materials, essential for applications like catalysis[31–33] or quantum information[34,35]. Efforts to circumvent these challenges are discussed in Sections 1.6 and 1.7.

On the other hand, one of the most popular electronic structure methods for modeling large systems, especially solid-state materials, either using large finite models or periodic boundary conditions, has been Kohn–Sham Density Functional Theory (KS-DFT)[36–38]. One limiting factor of KS-DFT is its dependence on the choice of exchange-correlation functionals, making the performance of a functional highly case-specific and not always systematically improvable[39–41]. Another limitation arises from the single-determinantal description of the system, which hinders KS-DFT's applicability in modeling inherently multi-configurational systems like transition metal oxides (TMOs), multiconfigurational excited states, or superconducting phases in cuprates without resorting to spin-symmetry breaking[42,43].

Recently, for studying periodic systems with weak correlation, MP2[44,45] and CC singles and doubles (CCSD)[46–48] have been employed. While these methods do not require heavy symmetry breaking and are systematically improvable, as discussed above, their steep scaling with system size (N^4 and N^6 for MP2 and CCSD, respectively) renders them prohibitively costly for the large number of atoms required to model solids. Multireference methods like MC-SCF or multireference perturbation theories, on the other hand, have rarely been used for solids since these methods scale as a high power or exponentially with the active space

size determined by the number of electrons and basis functions. However, as we discuss below and as is a large part of this thesis, we develop quantum embedding methods to make this possible.

1.6 Quantum Embedding Theories for Solids

An important concept that can be utilized in most problems are localized electron interactions. Often, important chemical or physical phenomena, such as those occurring at a catalytic active site or around a defect in a solid-state qubit candidate, are confined within a spatial region. Quantum embedding methods can significantly reduce computational costs accompanying conventional wavefunction-based methods by treating a smaller fragment, such as those around the defective region or the catalytic site, with a high-level method while employing a cheaper (usually mean-field) method for the larger rest of the system[49]. Quantum embedding can be distinguished based on the quantum variables of interest, which may include the physical system's density[50–57], Green's function[58–64], or a density matrix[65–68]. While a comprehensive description of each category is beyond the scope of this thesis, we direct the reader to the review by Sun *et al.*[49] for further details. In this thesis, we will primarily be concerned with developing density matrix embedding techniques, which stem from the density matrix embedding theory (DMET)[65].

In chapters 2-4 of this thesis, we present quantum embedding methods developed using the concept of density matrix embedding and strongly correlated electronic structure methods and their applications in computing ground state energies, excited state energies and adsorption energies in representative solid-state materials where conventional wavefunction methods are impractical. In chapter 2, we introduce the state-averaged CAS-DMET and NEVPT2-DMET methods for periodic systems and apply them to study electronic excitations in an oxygen vacancy (OV) on a MgO(100) surface and a neutral silicon vacancy in diamond[1]. In CAS-DMET, we employ the density matrix embedding formalism to reduce the infinite vari-

ational space to a finite, tractable space for variational orbital optimization using CASSCF. While CAS-DMET has been developed for studying the ground state of molecular systems this is the first time it has been developed for solids and the first time the state-averaged framework has been used for computing excited states. Despite the introduction of several active space selection techniques, variational optimization with well-chosen initial orbitals remains the most effective method for determining the optimal active space[69]. The primary challenges are the sizes of the active and variational spaces, the latter of which is addressed in this study. By significantly reducing the variational space, CAS-DMET provides a convenient and affordable way to address the active space selection problem in materials, which would otherwise be impossible. In NEVPT2-DMET, we perform NEVPT2 only within the finite embedding space to account for the important dynamical electron correlation effects, leading to significant cost reductions without compromising accuracy as we show using representative examples. In this work, we studied the oxygen vacancy (OV) on a MgO(100) surface and a neutral silicon vacancy in diamond as the initial applications. Following this work, NEVPT2-DMET has been applied to study excitation energies of spin defect systems such as the nitrogen-vacancy center in diamond and an oxygen vacancy defect in MgO which are discussed briefly at the end of chapter 2. In both of these cases, we found good agreement relative to the experimentally observed excitation energies as detailed in chapter 3.

In the third chapter, we extend the periodic formulation of DMET to heterogeneous catalysis applications and investigate its performance in calculating the adsorption energy of CO to the MgO(001) surface. Since this particular problem is single reference, we use coupled-cluster theory with single and double excitations and second-order Møller-Plesset perturbation theory as the high-level electronic structure solvers. In doing so we realize that such investigations require a relatively large embedding space and are therefore memory intensive. So, we present a memory-efficient procedure of storing and manipulating electron repulsion integrals in the embedding space within the framework of periodic DMET which reduces

memory requirements by 5-6 folds for the given case studies. This enhances the applicability of our density matrix embedding framework for larger embedding spaces as will be required in heterogeneous catalysis applications.

Although NEVPT2-DMET is considerably cheaper and more affordable than conventional NEVPT2, it still scales poorly with the active space size and the embedding space size. Hence we developed density matrix embedding using multiconfiguration pair-density functional theory (DME-PDFT), described in chapter four, which is a cost-effective method compared to NEVPT2-DMET to include electron correlation in calculating strongly correlated ground and excited states. DME-PDFT accounts for both static and dynamic correlation effects. In DMET-PDFT, the one- and two-reduced density matrices (1- and 2-RDMs) generated from a CAS-DMET calculation are used to compute the densities ρ and on-top pair densities Π, which are then used in a subsequent multiconfiguration pair-density functional theory (MC-PDFT) energy expression[70–72]. DME-PDFT, by construction, models electron correlation of all electrons regardless of the underlying embedding methodology, and is therefore formally less sensitive to the size of the embedded fragment than methods such as NEVPT2-DMET, which can only model electron correlation within the embedded subspace.

1.7 Quantum Computing with Localized Active Space Methods

While DME-PDFT addresses scaling issues related to dynamical correlation, CAS-DMET remains constrained by the size of the active space, as discussed in Section 1.5. One way to circumvent this issue is through the use of fragmentation techniques applied to active spaces. Such techniques include active space decomposition (ASD)[73–76], cluster mean-field[77], rank-one basis states[78,79], the TPSCI algorithm[80], restricted active space (RAS)[81,82], generalized active space (GAS)[83], and the localized active space self-consistent field (LASSCF) method[84,85], among others. This thesis specifically focuses on the LASSCF method, which divides the active space into localized subspaces. Inter-active space interactions are cap-

tured only through the underlying mean-field method, necessitating the use of post-LASSCF methods to restore interfragment correlation. To achieve this, we utilize quantum computing resources. Although quantum computers theoretically offer the potential to eliminate exponential scaling, they are currently limited by the capabilities of existing hardware, known as noisy intermediate-scale quantum (NISQ) devices[86]. In addition to the challenge of producing noise-free qubits, a key limitation of NISQ devices is their restricted circuit depth, quantified by the number of quantum gates.

In Chapter 5, we introduce a hybrid quantum-classical algorithm, the localized active space unitary selective coupled cluster singles and doubles (LAS-USCCSD) method. This algorithm, inspired by active space decomposition and selected configuration interaction techniques, is developed to reduce the quantum computational resource requirements, enabling scaling up application sizes on current and near-term quantum computers. LAS-USCCSD significantly reduces circuit depth by at least an order of magnitude for the benchmark systems explored, ranging from hydrogen chains to bimetallic compounds. This reduction is essential for the practical implementation of multireference hybrid quantum-classical algorithms on near-term quantum computers.

1.8 Applications with Multireference Methods

Finally, in Chapter 6, we present a collaborative theoretical and experimental work that examines metal-metal bonding in actinides. This topic is particularly relevant for multireference wavefunction theories due to the inherent multireference character of actinides, which arises from their partially filled f orbitals. For these systems, single-reference schemes are insufficient. The electronic structure of the uranium dimer, U_2, is notably complex and has been the subject of several theoretical studies[87–94]. For the first time, this research reports the anion photoelectron spectrum of U_2^- which was carried out by our experimental collaborators. On the theoretical front, our electronic structure calculations on U_2 and U_2^-,

conducted using multireference methods, reveal that while U_2 features a formal quintuple bond, U_2^- exhibits a quadruple bond. However, the effective bond orders differ by only 0.5 units, not one. This synergy between experimental and computational approaches sheds light on the nature of metal-metal bonding in U_2 and U_2^- and highlights the importance of proper active space selection and leads us to important developments that are yet to be tested in the quantum embedding and active space decomposition techniques developed in chapters 2-5.

1.9 List of Publications and Preprints

Although I have highlighted specific works relevant to this thesis, I have also contributed to other projects that fall outside its scope. Below is a list of all my published works, including those discussed and those not included in this thesis:

Publications included as chapters in this thesis:

- **Mitra A.**, Pham H. Q., Pandharkar R., Hermes M. R., and Gagliardi L. Excited States of Crystalline Point Defects with Multireference Density Matrix Embedding Theory, *J. Phys. Chem. Lett.* 2021, 12, 11688-11694 [Link][1]

- Ciborowski S. M., **Mitra A.**, Harris R. M., Liu G., Sharma P., Khetrapal N., Blankenhorn M., Gagliardi L., and Bowen K. H. Metal–Metal Bonding in Actinide Dimers: U_2 and U_2^-, *J. Am. Chem. Soc.* 2021, 143, 17023-17028 [Link][95]

- **Mitra A.**, Hermes M. R., Cho M., Agarawal V., and Gagliardi L. Periodic Density Matrix Embedding for CO Adsorption on the MgO(001) Surface, *J. Phys. Chem. Lett.* 2022, 13, 7483–7489 [Link][96]

- **Mitra A.**, Hermes M. R., and Gagliardi L. Density Matrix Embedding Using Multiconfiguration Pair-Density Functional Theory, *J. Chem. Theory Comput.* 2023, 19, 3498-3508 [Link][97]

- **Mitra A.**, D'Cunha R., Otten M., Wang, Q., Hermes, M. R., Alexeev, Y., Gray, S. and Gagliardi, L., Efficient Localized Active Space Method with a Unitary Selected Coupled Cluster Ansatz for Quantum Computing, *arXiv:2404.12927*, 2024 [Link][98]

Publications not included as chapters:

- Haldar S., **Mitra A.**, Hermes M. R., and Gagliardi L. Local Excitations of a Charged Nitrogen Vacancy in Diamond with Multireference Density Matrix Embedding Theory, *J. Phys. Chem. Lett.* 2023, 14 (18), 4273-4280 [Link][99]

- Verma S., **Mitra A.**, Jin Y., Haldar S., Vorwerk C., Hermes M. R., Galli G., and Gagliardi L. Optical Properties of Neutral F Centers in Bulk MgO with Density Matrix Embedding *J. Phys. Chem. Lett.* 2023, 14, 34, 7703–7710 [Link][100]

- Alexeev Y., Amsler M., Barroca M. A., Bassini S., Battelle T., Camps D., Casanova D., Choi Y. J., Chong F. T., Chung C., Codella C., Córcoles A. D., Dean M., Demarteau M., Di Felice R., Epting W. K., Finkel H., Ghaznavi F., Ghosh A., Gomes N., Hallman R., Holland E., Hu S., Kanungo B., Klymko K., Li M., Liao W.-K., Liddle S., Liles E., Liu M., Lopez-Bezanilla A., Luo T., Ma J., Maclean J. R., Mandal A., Marshall J., Maurer R., McIntosh T., Meng X., Motta M., Muller R., O'Brien K. P., Otten M., Palenik M., Peng B., Peschel J., Porter W., Prokofiev A., Prouza M., Roy A. D., Russina M., Sabo A., Sangiovanni G., Sharma S., Shankland N., Shi H., Shukla A., Si M., Spence S., Sriluckshmy P. V., Starr M., Sundararaman R., Susca J., Tenney I., Thiagarajan J., Trushin E., Wang Y., Wasiakowski E., West P., Windus T. L., Wismer M., Wisnieff R., Yu J., **Mitra A.**, Gagliardi L., and others. Quantum-centric Supercomputing for Materials Science: A Perspective on Challenges and Future Directions, *arXiv:2312.09733*, 2023 [Link][86]

- Fasulo F., **Mitra A.**, Muñoz-García A. B., Pavone M., and Gagliardi L. Role of Surface Ir-Oxo Specie in Tuning Molecular Oxygen Evolution Electrocatalysis by Iridium

Oxide: New Insights from Multireference Calculations, Articles ASAP, *J. Phys. Chem. C.* 2024 [Link][57]

CHAPTER 2

EXCITED STATES OF CRYSTALLINE POINT DEFECTS WITH MULTIREFERENCE DENSITY MATRIX EMBEDDING THEORY

This chapter is reprinted with permissions from *J. Phys. Chem. Lett.* **2021**, *12*, 48, 11688-11694

Abstract

Accurate and affordable methods to characterize the electronic structure of solids are important for targeted materials design. Embedding-based methods provide an appealing balance in the trade-off between cost and accuracy - particularly when studying localized phenomena. Here, we use the density matrix embedding theory (DMET) algorithm to study the electronic excitations in solid-state defects with a restricted open-shell Hartree–Fock (ROHF) bath and multireference impurity solvers, specifically, complete active space self-consistent field (CASSCF) and n-electron valence state second-order perturbation theory (NEVPT2). We apply the method to investigate an oxygen vacancy (OV) on a MgO(100) surface and find absolute deviations within 0.05 eV between DMET using the CASSCF/NEVPT2 solver, denoted as CAS-DMET/NEVPT2-DMET, and the non-embedded CASSCF/NEVPT2 approach. Next, we establish the practicality of DMET by extending it to larger supercells for the OV defect and a neutral silicon vacancy in diamond where the use of non-embedded CASSCF/NEVPT2 is extremely expensive.

2.1 Introduction

Quantum embedding theory offers an appealing solution for understanding the electronic structures of extended systems where conventional quantum chemical methods are impracti-

cal.[101] Various formulations of quantum embedding theory aims at describing a small region of interest, *i.e.*, a "fragment" or "impurity," using an accurate yet expensive method while treating the rest of the system at a lower level of theory, usually a mean-field method such as Hartree–Fock (HF)[7] or Kohn-Sham density functional theory (KS-DFT).[102,103] Density matrix embedding theory[68,104–106] is a wave function-in-wave function embedding technique where the environment of the fragment is effectively modeled with a bath constructed by a Schmidt decomposition of a mean-field wave function.[107] Recently, the DMET algorithm formulated using a restricted closed-shell Hartree–Fock (RHF) bath for solid-state systems within the framework of periodic boundary condition has been introduced independently by some of the authors[108] as well as by Cui *et al.*.[109] Our preliminary investigations revealed that DMET provides ground-state energies and band structures of simple solids like the periodic hydrogen chain and polyyne.[108]

In this Letter, we investigate the performance of periodic DMET in describing excited states of point defects in solid-state systems. While the previous algorithm used a restricted Hartree-Fock (RHF) bath, we now employ a ROHF bath in order to treat the open-shell electronic states of the oxygen vacancy on a MgO(100) surface and of a silicon vacancy in diamond. We implemented the complete-active space self-consistent field (CASSCF)[26–28] and strongly-contracted n-electron valence state second-order perturbation theory (NEVPT2)[110–113] multireference methods as impurity solvers to capture electron correlation of excited states. While CASSCF has been used as a DMET solver within the molecular context,[114] this is the first time that NEVPT2 is used as a high-level method in DMET. Our tests on the oxygen vacancy on a MgO(100) surface show that using ROHF as the low-level wave function in conjunction with the CASSCF/NEVPT2 solver offers an accurate description of strongly correlated electrons. The approach proposed here does not require the high-level wave function to break spin symmetry, as in the case in which the spin-unrestricted Hartree–Fock (UHF) method is employed for the low-level wave function.[115,116].

The theory and implementation of DMET for lattice models[104,117,118] and molecular systems have been discussed extensively in previous publications. Readers are encouraged to refer to these publications for more details.[68,106]

A spin-restricted Hartree–Fock wave function is used to initialize a periodic DMET calculation. The impurity is then defined using a set of localized orbitals in real space. We use the maximally-localized Wannier functions (MLWFs)[119,120], implemented in the wannier90[121] code. The translational symmetry is broken for defective solids and the unit cell is chosen to be sufficiently large to avoid the interaction between periodic images of the defect. As a result, the Brillouin zone can be adequately sampled at the Γ-point and a subset of N_{imp} MLWFs at the chemical region of interest, for example those around the defective site, defines the impurity. The bath is a set of orbitals representing the environment and is constructed using the Schmidt decomposition,[106] which for any single determinant requires only the one-body reduced density matrix (1-RDM). The environment block (D_{env}) of the 1-RDM is diagonalized, $D_{\mathrm{env}} = \mathbf{U}\lambda\mathbf{U}^*$, where λ is a diagonal matrix of eigenvalues λ_i ($i = 1, 2, ..., N_{\mathrm{env}}$ where N_{env} is the number of the environment orbitals). The columns of the unitary matrix $\mathbf{U}$ corresponding to λ_i other than zero or two define the entangled bath orbitals; the remainder are treated as a frozen core in the subsequent embedding calculation. For a RHF wave function, the number of $0 < \lambda_i < 2$ eigenvalues is at most N_{imp}. For a high-spin ROHF wave function, it is straightforward to prove that the number of $0 < \lambda_i < 2$ eigenvalues is at most $N_{\mathrm{imp}} + 2S$, where S is the total spin quantum number of the computational supercell. Note that this implies that we assign all the unpaired electrons in the ROHF bath to the impurity by *fiat*. We thus denote DMET using the RHF and ROHF bath as DMET@RHF and DMET@ROHF, respectively.

Following the Schmidt decomposition, the high-level wave function, $|\Psi_{\mathrm{imp}}\rangle$, which formally diagonalizes the impurity Hamiltonian, $\hat{H}_{\mathrm{imp}}$, in the combined Fock space of the impurity and bath orbitals can be determined by any high-level solver of choice, for instance, CASSCF

or NEVPT2. All calculations are performed using our in-house pDMET code and the PySCF package for electron integral and quantum chemical solvers.[122–124] The calculations are all performed without enforcing any spatial symmetry. We will refer to the CASSCF or NEVPT2 calculations performed at the Γ-point without the use of DMET as non-embedding references or the full calculations.

2.2 Computational details

All DMET calculations are performed using our in-house pDMET code which utilizes the electron integrals and quantum chemical solvers from the PySCF package.[122,123] The code is available on the GitHub repository.[125] Wannier90[121] is used to construct MLWFs via the pyWannier90 interface.[126] In the Wannierisation procedure, all available bands are used for the calculations. Electron integrals and Γ-point (non-embedding) calculations are obtained by means of PySCF. We also employ the efficient algorithm for the orbital transformation to the embedding space which has been introduced recently by Cui *et al.*[109]. The spin-restricted formalism is used in all the calculations. The GTH pseudopotentials[127] is used for all the calculations.

The geometry optimizations are performed at the spin-unrestricted PBEsol level[128] using the Vienna *Ab initio* Simulation Package (VASP).[129–132] The convergence criteria of 10^{-6} eV and 10^{-3} eV/Å are used for the energy and force, respectively.

Oxygen vacancy model (OV): First, we consider a single layer model, denoted as $Mg_{18}O_{18}$, to represent the MgO(100) surface. The oxygen vacancy defects are created by removing the neutral oxygen atom at the center of the unit cell. We use a vacuum of 23.518 Å to separate the layer and its periodic images along the [100] direction. In the DMET calculations, we place a dummy oxygen atom at the vacancy to provide basis functions to span the electron density of the defect. The polarized triple-zeta basis set TZVP is used for the dummy oxygen and eight nearest atoms (4 O and 4 Mg) while the polarized double-zeta basis set

DZVP is used for all other atoms. The first singlet-singlet excitation is computed via the state-averaging formalism of CASSCF[133–135] with equal weights for the first two roots. The singlet-triplet excitation is computed using the difference between a state-specific CASSCF for the triplet state and the first root of the state-averaged singlet calculations. The double and triple layered model are constructed by placing non-defective one and two layers of $Mg_{18}O_{18}$ below the first layer respectively. For these models the polarized triple-zeta basis set TZVP is used for the dummy oxygen and nine nearest atoms (4 O and 5 Mg) while the polarized double-zeta basis set DZVP is used for all other atoms. The orbitals in the (2,8) active space and for the two and three layered systems do not transform as irreps therefore we use S_n to label the nth excited singlet states and T_n to label nth triplet states.

Neutral silicon vacancy in carbon diamond (SiV^0): The silicon vacancy defect is created by removing two carbons followed by inserting a silicon atom in the midpoint. A $2 \times 2 \times 2$ supercell of the primitive cell of the carbon diamond crystal is used for numerical testing, resulting in a SiC_{52} model with 53 atoms. For extension to realistic models a $4 \times 4 \times 4$ supercell of the primitive cell of the carbon diamond crystal and a $3 \times 3 \times 3$ supercell of the 8-atom unit cell of the carbon diamond crystal are used resulting in SiC_{126} model with 127 atoms and SiC_{214} model with 215 atoms respectively. We use S_n and T_n for labelling the nth excited singlet and triplet states respectively. We use the polarized triple-zeta basis set TZVP for Si, the polarized double-zeta basis set DZVP for the six nearest carbons with respect to the Si site, and the double-zeta basis set DZV for the rest.[136]. We use the state-average CASSCF formalism by averaging over 4 singlet states with equal weights to obtain singlet state energies to and 6 triplet states with equal weights to obtain triplet state energies. An active space of 10 electrons in 12 orbitals was used and has been denoted as (10,12) For computing all excitation energies, the triplet ground state is considered as a reference.

Cluster calculations for the silicon vacancy in carbon diamond (SiV^0): A cluster of the Si vacancy -consisting of the silicon and 54 carbons (3 coordination spheres around

the Si) - was cut from the optimized periodic structure. The dangling bonds of the carbons on the edges were capped with an appropriate number of hydrogen atoms to maintain the neutrality of the cluster. The positions of the hydrogens were optimized with all other atom positions frozen using M06-L/def2-svp level of theory in Gaussian16. The CASSCF and NEVPT2 calculation on the cluster were performed in Orca (version 4.2.0) with cc-pvdz basis on the carbons and the cc-pvtz basis on the silicon atom. Density fitting with resolution of identity and numerical chain-of-sphere integration (RIJCOSX) was used to reduce the cost of computation. The strongly contracted (SC) NEVPT2 was used in all cases. Separate state average calculations for the singlet and triplet multiplicities with 4 and 6 states respectively were performed with an active space of 10 electrons in 12 orbitals (10,12).

Identification of the defect states: First, the molecular orbitals **C** (equivalently, the Bloch orbitals in a Γ-point sampling calculation) are orthogonalized using the overlap matrix **S**:

$$\tilde{\mathbf{C}} = \mathbf{S}^{1/2}\mathbf{C} \tag{2.1}$$

For each orbital, the weight (w_i) of the defect site **X** is calculated by:

$$w_i = 100 \times \frac{\sum_{\mu \subset \mathbf{X}} \tilde{C}_{\mu i}^2}{\sum_{\mu} \tilde{C}_{\mu i}^2} \tag{2.2}$$

Defect states are the orbitals that are in close proximity to Fermi energy and exhibit a significant contribution from **X**. For OV, **X** is the dummy atom, and the two defect states a_{1g} and a_{2u} exhibit a weight of 17.4 and 18.6 %, respectively. Similarly, **X** is the silicon atom for the SiV^0 system, and the four defect states e_{ux}, e_{uy}, e_{gx} and e_{gy} exhibit a weight of 13.4, 13.4, 20.6, and 20.6 %, respectively .

2.3 Results and Discussions

2.3.1 Oxygen vacancy (OV) in magnesium oxide

First, we consider the oxygen vacancy (OV) in magnesium oxide. This point defect plays a crucial role in energy storage and photoelectrochemical applications of metal oxides.[137–139] The oxygen vacancy exists both in the bulk as well as on the surface of the oxide. We investigate the performance of our method in calculating the first singlet-singlet and singlet-triplet excitations of a neutral oxygen vacancy, denoted here as OV, on the (100) monolayer of MgO. In particular, the removal of an oxygen atom (O) from the ionic crystal composed of the O^{2-} and Mg^{2+} ions results in two electrons trapped in the cavity left by the missing oxygen, denoted as a F-center (or a color center). The $Mg_{18}O_{18}$ model of OV is shown in Fig. 2.1a. All the geometries used in this study for the OV defect have been optimized using the PBEsol functional. Further details are discussed in section S01 of the SI of reference 1. The full space group of this monolayer model system contains the D_{4h} point group as a subgroup, and the two localized defect orbitals transform as the a_{1g} and a_{2u} irreducible representations, as shown in Fig. 2.1b (see Section S01 of the SI of reference 1 for more details on how the defect states are identified). Although the gaps between the valence band (VB) and conduction band (CB) obtained by RHF(S=0) and ROHF(S=1) are similar, the positions of the a_{1g} and a_{2u} orbitals with respect to the valence band maximum depend on the spin imposed in the mean-field calculation, as shown in Fig. 2.1c. Later, we extend our calculations to larger unit cells as shown in Fig. 2.1d. In the DMET calculations, we consider three impurity clusters of expanding size to investigate how the choice of the impurity cluster affects the excitation energies (see Fig. 2.1e). The CASSCF and NEVPT2 methods are used as high-level solvers and the impurity is embedded in either the RHF or ROHF mean-field wave function. All the DMET calculations are performed on geometries optimized by the PBEsol functional. Readers are referred to Section S01 of the SI of reference

1 for a detailed description of the computational methodologies. An active space of two electrons in two orbitals is employed in all calculations because there are two electrons and two defect orbitals localized at the F-center. The same active space was previously used.[140] We compare our embedding results with non-embedding Γ-point calculations on $Mg_{18}O_{18}$ at the same level of theory. The ground-state wave function for the F-center mainly consists of the $a_{1g}^{\uparrow\downarrow}$ determinant, leading to a $^1A_{1g}$ state. The first singlet excited-state, $^1A_{2u}$, results from the linear combination of the $a_{1g}^{\uparrow}a_{2u}^{\downarrow}$ and $a_{1g}^{\downarrow}a_{2u}^{\uparrow}$ determinants with an equal weight of *ca.* 48 %. Similarly, the first triplet excited-state, $^3A_{2u}$, is the $a_{1g}^{\uparrow}a_{2u}^{\uparrow}$ determinant.

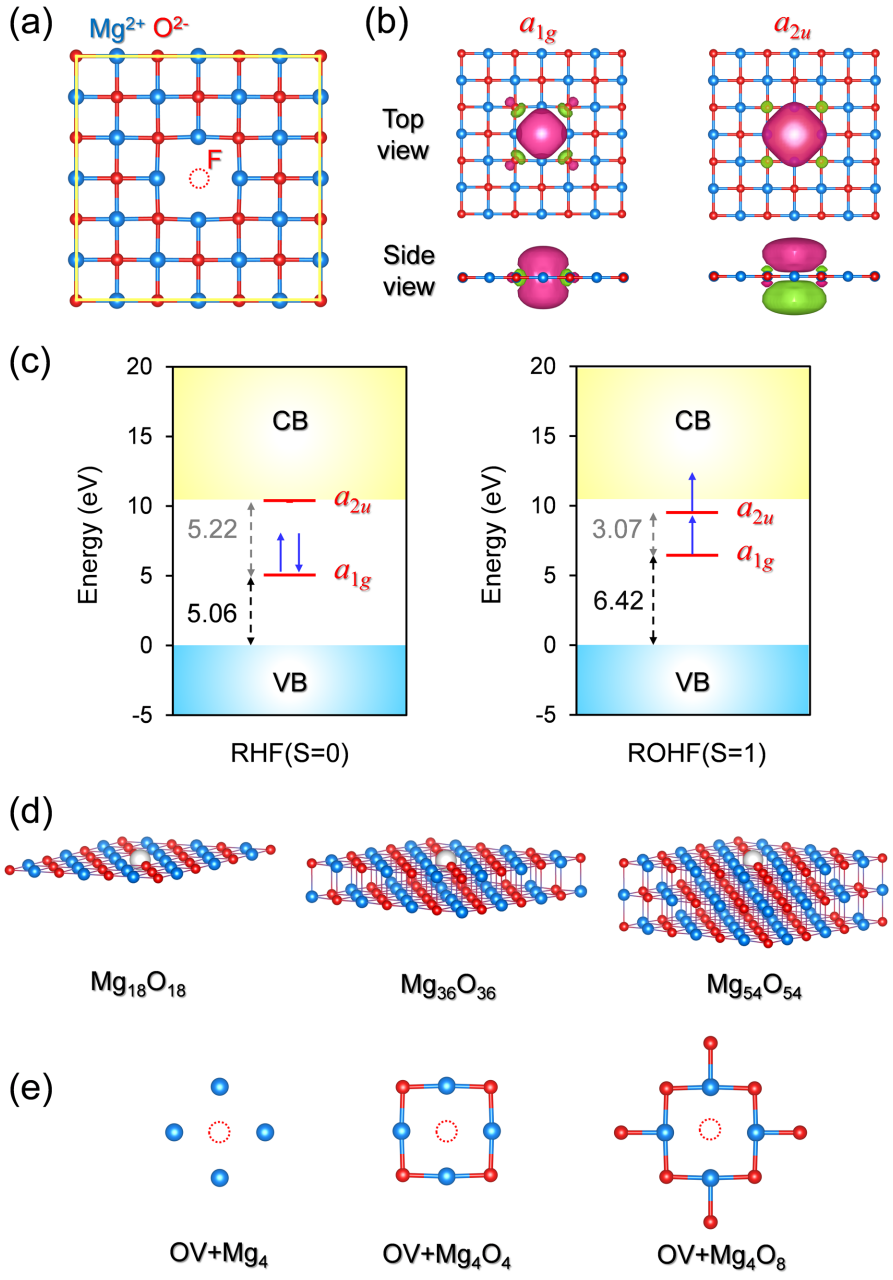

Figure 2.1: Oxygen vacancy on a $Mg_{18}O_{18}$ layer: (a) Top view of the F-center on the (100) surface. (b) Top and side view of two defect orbitals a_{1g} and a_{2u} from the ROHF(S=1) calculation. The isosurface of orbitals is 0.03. (c) Relative energy of defect orbitals with respect to the valence band maximum. The Fermi energy (or valence band maximum) is set to 0; (d) Oxygen vacancy models with different numbers of layers: $Mg_{18}O_{18}$, $Mg_{36}O_{36}$, and $Mg_{54}O_{54}$. The top layer corresponds to (a) in each of these cases; The gray atom highlights the oxygen vacancy. (e) Three different impurity clusters considered in the DMET calculations. For $Mg_{36}O_{36}$ and $Mg_{54}O_{54}$, the Mg atom right below the vacancy is also included, resulting in OV+Mg_5O_4 instead of OV+Mg_4O_8.

Table 2.1: Vertical excitation energies (in eV) of the oxygen vacancy on the MgO(100) surface obtained using DMET with CASSCF and NEVPT2 as the solvers compared to CASSCF and NEVPT2 results at Γ-point. "Reference" here indicates the non-embedded Γ-point CASSCF and NEVPT2 calculations. The extrapolated CAS-DMET and NEVPT2-DMET energies from the linear regression are labeled as "Extrap". All results are obtained using a (2,2) active space.

Excitation	Method	Impurity cluster	CASSCF	NEVPT2
$^1A_{1g} \rightarrow {}^3A_{2u}$	DMET@RHF	OV+Mg_4	2.70	3.22
		OV+Mg_4O_4	1.78	2.53
		OV+Mg_4O_8	1.37	2.18
		Extrap	1.10	1.98
	DMET@ROHF	OV+Mg_4	1.30	1.91
		OV+Mg_4O_4	1.32	2.09
		OV+Mg_4O_8	1.32	2.12
		Extrap	1.33	2.18
	Reference		1.33	2.19
$^1A_{1g} \rightarrow {}^1A_{2u}$	DMET@RHF	OV+Mg_4	5.38	5.11
		OV+Mg_4O_4	3.96	3.68
		OV+Mg_4O_8	3.30	3.05
		Extrap	2.88	2.62
	DMET@ROHF	OV+Mg_4	3.27	3.17
		OV+Mg_4O_4	3.26	3.05
		OV+Mg_4O_8	3.25	3.00
		Extrap	3.25	2.97
	Reference		3.25	2.95

Table 2.1 shows the vertical excitation energies for the OV system. The excitation energies are overestimated by DMET using the RHF(S=0) bath. The deviation with respect to CASSCF for the largest impurity cluster OV+Mg_4O_8 is *ca.* 0.04 and 0.05 eV for the singlet-singlet and singlet-triplet excitation, respectively. For the ROHF(S=1) bath, the smallest impurity cluster OV+Mg_4 already agrees well with CASSCF, with a deviation of 0.02-0.03 eV for both transitions. The excitation energies obtained using OV+Mg_4O_8 are almost identical to the CASSCF references. These results suggest that the bath constructed from a ROHF(S=1) wave function is superior to that from the RHF(S=0) wave function. Interestingly, we find a linear dependence between the NEVPT2 excitation energies and the inverse of the number of embedding orbitals as shown in Figure 2.2, which suggests that it is realistic to extrapolate the NEVPT2-DMET energy to the one corresponding to the full system. It should be noted that similar convergence patterns have been observed and linear extrapolation techniques have been used in recent studies.[47,141] Our extrapolations for the ROHF(S=1) bath result in a deviation of only 0.02 and 0.01 eV for the singlet-singlet and singlet-triplet excitation, respectively between the embedding and non-embedding calculations. The same extrapolation for the RHF(S=0) bath does not provide good agreement with the reference, highlighting the importance of a good DMET bath for both accuracy and efficiency for our embedding scheme.

The bath constructed from a ROHF(S=1) wave function is superior to that from the RHF(S=0) wave function likely due to the fact that the RHF bath is built from a determinant in which the a_{2u} orbital, which plays a prominent role in both excitations here considered, is unoccupied. Unoccupied orbitals do not generate bath orbitals, and the embedding space is therefore deficient in orbitals of symmetry a_{2u}, compared to the subspace generated *via* the ROHF bath, which has the a_{2u} orbital singly occupied. Indeed, we could see an a_{2u}-like orbital in the embedding space generated by the ROHF bath, which cannot be found in the

case of the RHF bath (see Figure 2 of the SI of reference 1). The presence of this orbital increases the size of the basis in which the CASSCF solver may optimize the a_{2u} active orbital. Of course, with either bath wave function, additional orbitals of a_{2u} symmetry can be made available to the CASSCF solver by increasing the size of the impurity. However, a small impurity cluster is sufficient if one employs a good bath, as can be seen in the case of the ROHF(S=1) wave function. At the NEVPT2 level of theory, the same conclusion could be drawn, particularly, the DMET results converge to the reference values as the size of the impurity cluster increases.

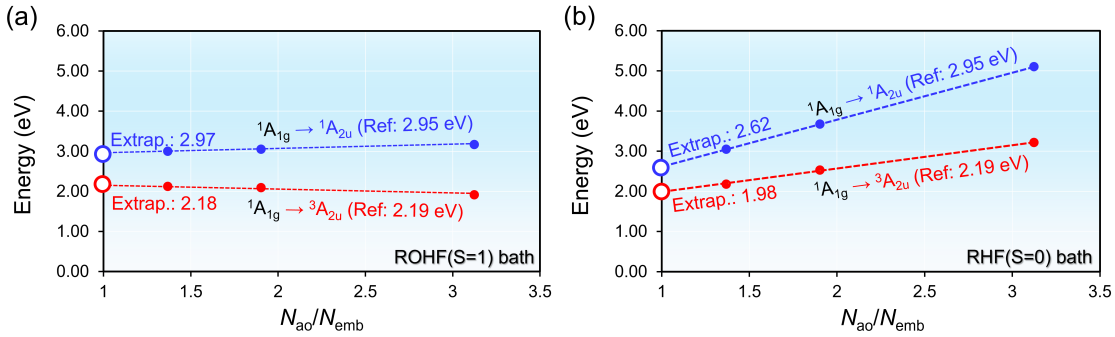

Figure 2.2: NEVPT2-DMET excitation energies of OV using (a) ROHF(S=1) and (b) RHF(S=0) bath bath as a function of $N_{\text{ao}}/N_{\text{emb}}$ where N_{ao} is the number of basis functions of the entire system and N_{emb} is the number of embedding orbitals. The $^1A_{1g} \rightarrow {}^1A_{2u}$ and $^1A_{1g} \rightarrow {}^3A_{2u}$ transition are highlighted in blue and red, respectively. The extrapolated energy is indicated with the "Full" label. The reference NEVPT2 energy for each excitation is also given.

We extend our study to the oxygen vacancy on the MgO surfaces containing two or three layers, resulting in $Mg_{36}O_{36}$ and a $Mg_{54}O_{54}$ respectively (see Figure 2.1d). For these systems, we use a larger active space of two electrons in eight orbitals with s and p character localized at the defect (shown in the SI of reference 1). The non-embedding CASSCF or NEVPT2 calculations for these models are not possible with our current computational capabilities. However, within the embedding framework, such calculations are possible. We investigate the performances of CAS-DMET and NEVPT2-DMET in calculating the singlet-singlet and

singlet-triplet excitation energies (shown in Table 2.2). The surface models with increasing number of layers allow us to study the convergence of the excitation energy with respect to the thickness of the slab. It is observed that although the $S_0 \rightarrow S_1$ excitation energies differ by 0.5-0.6 eV when moving from a single- to a double-layer model, the difference between the two- and three-layer models is about 0.1 eV for both $S_0 \rightarrow S_1$ and $S_0 \rightarrow T_1$ excitations. Moreover, the in-plane expansion of the layer model only slightly changes the excitation energies (see Section S05 of the SI of reference 1). Unfortunately, there has yet been no consensus on the $S_0 \rightarrow S_1$ excitation energy of the surface F-center. The $S_0 \rightarrow S_1$ excitation is estimated to be about 1-5 eV by different experimental techniques.[142–144] Computationally, the quantum mechanics/molecular mechanics (QM/MM) approach using the multireference configuration interaction (MRCI) method as the QM solver on a cluster model of OV predicts an excitation energy of 3.24 eV and 1.93 eV for the $S_0 \rightarrow S_1$ and $S_0 \rightarrow T_1$ excitations;[145] our CAS-DMET and NEVPT2-DMET calculations predict excitation energies 0.3-0.4 eV higher than this particular reference.

Table 2.2: Vertical excitation energies (in eV) of the oxygen vacancy on the MgO(100) surface obtained using CAS-DMET and NEVPT2-DMET using an (2,8) active space. The extrapolated CAS-DMET and NEVPT2-DMET energies from the linear regression are labeled as "Extrap". The values preceded by a star correspond to the experimental measurement.

Excitation	Layers	Impurity cluster	CASSCF	NEVPT2	Literature
$S_0 \rightarrow T_1$	$Mg_{18}O_{18}$	OV+Mg_4	1.93	1.98	
		OV+Mg_4O_4	1.97	2.07	
		OV+Mg_4O_8	1.98	2.13	
		Extrap	1.99	2.11	
	$Mg_{36}O_{36}$	OV+Mg_4	2.19	2.19	
		OV+Mg_4O_4	2.25	2.25	
		OV+Mg_4O_5	2.26	2.28	1.93[145]
		Extrap	2.32	2.35	
	$Mg_{54}O_{54}$	OV+Mg_4	2.20	2.13	
		OV+Mg_4O_4	2.26	2.19	
		OV+Mg_4O_5	2.28	2.21	
		Extrap	2.35	2.28	
$S_0 \rightarrow S_1$	$Mg_{18}O_{18}$	OV+Mg_4	3.48	3.37	
		OV+Mg_4O_4	3.46	3.34	
		OV+Mg_4O_8	3.45	3.30	
		Extrap	3.45	3.29	
	$Mg_{36}O_{36}$	OV+Mg_4	4.01	3.90	3.24[145]
		OV+Mg_4O_4	3.97	3.86	*2.30[142]
		OV+Mg_4O_5	3.91	3.75	*1.0, *1.3, *2.4, *3.4[143]
		Extrap	3.87	3.70	*1.2, *3.6, *5.3[144]
	$Mg_{54}O_{54}$	OV+Mg_4	3.90	3.79	
		OV+Mg_4O_4	3.87	3.75	
		OV+Mg_4O_5	3.81	3.67	
		Extrap	3.77	3.62	

2.3.2 Neutral silicon vacancy (SiV^0) in diamond

Next, we discuss electronic excitations in the neutral silicon vacancy (SiV^0) in diamond, a typical qubit candidate and a bulk defective system.[146] In particular, we compute the first three singlet and first five triplet excitation energies, which have been studied previously using KS-DFT[147–149] as well as density functional-based embedding techniques.[63,150,151] The ground state of SiV^0 is a triplet, therefore, the use of a ROHF low-level wave function is necessary. Three models of increasing unit cell size representing the SiV^0 vacancy in diamond have been explored as shown in Figure 2.3a. We considered two choices for the impurity cluster: SiC_6 and SiC_{12} as shown in Figure 2.3b. We report the excitation energies computed using the SiC_{12} impurity cluster in Table 2.3. The excitation energies computed using the smaller SiC_6 impurity cluster are reported in the SI of reference 1. As one can expect, finite-size errors have a significant effect on the evaluation of excitation energies for both CAS-DMET and NEVPT2-DMET. The excitation energies differ by *ca.* 0.2-0.5 eV when moving from the SiC_{52} to the SiC_{126} unit cell, but only about 0.1 eV when moving from SiC_{126} to SiC_{214}. Since our results appear to be converged to a smaller error bar than the difference between our predictions and others reported in the literature, we tentatively conclude that finite-size effects are unlikely to be principally responsible for this disagreement. Similar to the OV defect, all the structures here used for the Γ-point are optimized using the PBEsol functional. Additionally, we have used a finite cluster ($SiC_{54}H_{78}$) to compute excitation energies and have compared them with the periodic calculations.This has been obtained from the optimized SiC_{214} crystal structure. The terminal hydrogens are further optimized using the MO6-L functional. Further details have been provided in the SI of reference 1. In Table 2.3, the excitation energies are compared with other computational and experimental values. Strictly speaking, the experimental number (1.31 eV)[152] is a zero-phonon line (ZPL) and should not be directly compared to the vertical excitation energies. We are not aware of experimental data for the vertical excitation energy. The vertical excitation energies are

expected to be larger depending on the excited state minimum. All our excitation energies are higher than those reported by Ma *et al.*[150,151]. We also note that Ma *et al.* used an active space of (16,9) and evaluated its convergence by adding only more doubly occupied orbitals. Here, we use a different active space of (10,12), which includes more unoccupied orbitals from the conduction band. The active orbitals (shown in the SI of reference 1) are localized around the defect and have *s*-like, *p*-like and *d*-like characters from the silicon atom and the 6 surrounding carbon atoms which form the dangling SiC bonds. The singlet-triplet gaps for the SiC_{214} model are within 0.1 eV of the cluster calculations. The CASSCF and CAS-DMET triple-triplet excitations for SiC_{214} differ by 0.15-0.25 eV whereas the cluster NEVPT2 and NEVPT2-DMET differ by 0.3-0.5 eV. We think that the results do not significantly depend on the localization procedure since, after the localization, we optimize the orbitals using CASSCF.

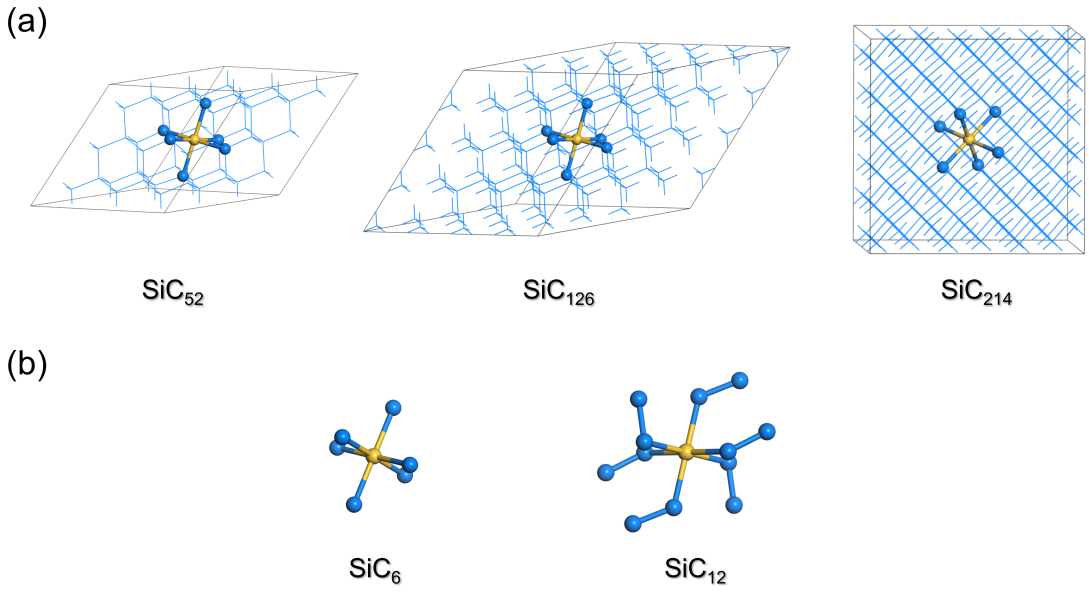

Figure 2.3: Neutral silicon vacancy in carbon diamond: (a) Three supercell models: SiC_{52}, SiC_{126}, and SiC_{214}. (b) The impurity clusters used in our DMET calculations: SiC_6 and SiC_{12}

.

Table 2.3: Singlet and triplet excitation energies (in eV) of SiV^0 computed using CAS-DMET and NEVPT2-DMET using the SiC_{12} impurity cluster shown in Figure 2.3b. The Table shows excitation energies for the SiC_{52}, SiC_{126} and SiC_{214} unit cells. The excitation energies reported under the "$SiC_{54}H_{78}$ cluster" column have been calculated using CASSCF and NEVPT2 calculations on a finite cluster $SiC_{54}H_{78}$. All calculations use an active space of (10,12). Computational values from literature are also included. The experimental value is the zero-phonon line and not a vertical excitation energy

State	CAS-DMET			NEVPT2-DMET			$SiC_{54}H_{78}$ cluster		Literature	
	SiC_{52}	SiC_{126}	SiC_{214}	SiC_{52}	SiC_{126}	SiC_{214}	CASSCF	NEVPT2	Comput.	Expt.
T_0	0.00	0.00	0.00	0.00	0.00	0.00	0.00	0.00		
T_1	2.84	2.37	2.26	2.71	2.51	2.39	2.10	2.10	1.583[150]	
T_2	2.97	2.51	2.44	2.76	2.55	2.47	2.19	2.16	1.568[148],1.594[150]	1.31[152]
T_3	3.03	2.54	2.44	2.85	2.55	2.46	2.25	2.14	1.568[148],1.594[150]	1.31[152]
T_4	3.41	3.21	3.16	2.82	2.67	2.61	3.04	2.14	1.792[150]	
S_1	0.59	0.52	0.50	0.17	0.48	0.51	0.56	0.54	0.336[150]	
S_2	0.60	0.52	0.50	0.19	0.47	0.51	0.56	0.53	0.336[150]	
S_3	1.45	1.37	1.36	0.71	1.12	1.14	1.44	1.10	0.583[150]	

Finally, we comment on the scaling of NEVPT2-DMET as compared to the reference NEVPT2 calculations. The computational cost of DMET is mainly dominated by the cost of the multireference calculations within the embedding space. The evaluation of the four-body reduced density matrix (4-RDM) required in NEVPT2 suffers from a scaling of $\mathcal{O}[N_{\text{det}} \times N_{\text{act}}^8]$, where N_{det} is the number of determinants (or configuration state functions, *i.e.*, CSF) and N_{act} is the number of active orbitals. NEVPT2-DMET has this step in common with NEVPT2. However, for a small number of determinants, the cost scaling in practical applications is controlled by the size of the parameter space, rather than the evaluation of the 4-RDM. The strongly contracted formalism[113] employed throughout this work has an overall parameter space of $\mathcal{O}[N_{\text{det}} + N_{\text{inact}}^2 N_{\text{vir}}^2]$,[153] where N_{inact} and N_{vir} are the number of inactive (doubly occupied) and virtual (empty) orbitals, respectively. For, again, a small number of deter-

minants, the computational cost of NEVPT2 will therefore exhibit an approximate scaling of $\mathcal{O}[N_{\text{inact}}^2 N_{\text{vir}}^2]$. NEVPT2-DMET removes unentangled orbitals from the parameter space, and therefore has a lower effective N_{inact} and/or N_{vir} than the corresponding NEVPT2 calculation. If all N_{core} unentangled orbitals are doubly occupied, the scaling of NEVPT2-DMET becomes $\mathcal{O}[(N_{\text{inact}} - N_{\text{core}})^2 N_{\text{vir}}^2]$; if they are all empty, the scaling of NEVPT2-DMET becomes $\mathcal{O}[N_{\text{inact}}^2 (N_{\text{vir}} - N_{\text{core}})^2]$. The advantage of the embedding treatment will become more significant for realistic applications using large basis set where the defect concentration is in fact very low. Therefore, the defect is often embedded in a large environment whose many unentangled orbitals can be excluded within the DMET framework.

2.4 Conclusion

In summary, we have generalized our periodic DMET to open-shell solids with the Brillouin zone sampled at the Γ-point in order to study the excited states of point defects. We have implemented the ROHF bath for open-shell systems and have explored the performance of CASSCF and NEVPT2 as the high-level impurity solvers within the framework of density matrix embedding for solid-state systems. Our initial applications of the method demonstrate a good agreement between the embedding and the non-embedding calculations which are computationally expensive for the systems studied here. We have utilized DMET to compute CASSCF/NEVPT2 excitation energies in supercells where the non-embedding calculations become intractable. This paves the way for the applicability of multireference methods on a regular basis for periodic systems. We note that an algorithmic improvement over the expensive computation of the exact exchange for periodic systems could further enhance the applicability of our method for large-scale computations of solid-state defects. Furthermore, the simple extension of the bath to open-shell solids introduced in this work can be generalized to the **k**-point sampling of the Brillouin zone to study magnetic ordering in solids. We envision that the method proposed here will be used in the future to study

quantum materials and extended systems containing lanthanides and actinides.

2.5 Further Applications of NEVPT2-DMET

This section of the chapter is partially adapted with permissions from *J. Phys. Chem. Lett.* **2023**, *14*, 18, 4273–4280 and *J. Phys. Chem. Lett.* **2023**, *14*, 34, 7703–7710

In a following work, we have investigated the excited states of a negatively charged nitrogen-vacancy center in diamond using CAS-DMET and NEVPT2-DMET[154]. Since the NEVPT2-DMET energies show a linear dependence on the inverse of the size of the embedding subspace, we performed an extrapolation of the excitation energies to the nonembedding limit using a linear regression. The extrapolated NEVPT2-DMET first triplet–triplet excitation energy is 2.31 eV and that for the optically inactive singlet–singlet transition is 1.02 eV, both in agreement with the experimentally observed vertical excitation energies of ∼2.18 eV and ∼1.26 eV, respectively. This is the first application of pDMET to a charged periodic system and the first investigation of the NV– defect using NEVPT2 for periodic supercell models.

In another following work, we investigated the optical spectra of neutral oxygen vacancies (F0 centers) in the bulk MgO lattice using CAS-DMET and NEVPT2-DMET[100]. To estimate defect-localized vertical excitation energies at the nonembedding and thermodynamic limits, a double extrapolation scheme is employed. The extrapolated NEVPT2-DMET vertical excitation energy value of 5.24 eV agrees well with the experimental absorption maxima at 5.03 eV, whereas the excitation energy value of 2.89 eV at the relaxed triplet defect-localized state geometry overestimates the experimental emission at 2.4 eV by only nearly 0.5 eV, indicating the involvement of the triplet–singlet decay pathway.

Acknowledgement

We thank Hung Q. Pham, Giullia Galli, Joachim Sauer and Debmalya Ray for insightful discussion. We are grateful to Zhihao Cui, Tianyu Zhu, Garnet K.-L. Chan for sharing with us the Gaussian density fitting transformation code. This work was funded by the Division of Chemical Sciences, Geosciences, and Biosciences, Office of Basic Energy Sciences of the U.S. Department of Energy through Grant DE-SC002183. Computer resources were provided by the Minnesota Supercomputing Institute at the University of Minnesota and the University of Chicago Research Computing Center.

CHAPTER 3

PERIODIC DENSITY MATRIX EMBEDDING FOR CO ADSORPTION ON THE MGO(001)SURFACE

This chapter is reprinted with permissions from *J. Phys. Chem. Lett.* **2022**, *13*, 32, 7483-7489

Abstract

The adsorption of simple gas molecules to metal oxide surfaces is a primary step in many heterogeneous catalysis applications. Quantum chemical modeling of these reactions is a challenge both in terms of cost and accuracy, and quantum-embedding methods are promising, especially for localized chemical phenomena. In this work, we employ density matrix embedding theory (DMET) for periodic systems to calculate the adsorption energy of CO to the MgO(001) surface. Using coupled-cluster theory with single and double excitations and second-order Møller-Plesset perturbation theory as quantum chemical solvers, we perform calculations with embedding clusters up to 266 electrons in 306 orbitals; the largest embedding models agreeing to within 1.2 kcal/mol of the non-embedding references. Due to the need of large impurity clusters for surface chemistry, we present a memory-efficient procedure of storing and manipulating electron repulsion integrals in the embedding space within the framework of periodic DMET.

3.1 Introduction

Magnesium oxide (MgO) surface plays an important role in several heterogeneous catalytic reactions, such as the partial oxidation of methane,[155] the Guerbet reaction at low pressure,[156] the synthesis of 2-amino-2-chromenes using benign reactants[157], the conversion

of ethane to ethylene[158] and the formation of carbonates from carbon monoxide in the presence of oxygen.[159] Modeling the surface adsorption of simple molecules, for example carbon monoxide (CO), to metal-oxide surfaces like MgO is an important step for theorists towards the understanding of heterogeneous catalysis, but it is challenging.[160–163] The CO molecule binds to the MgO surface, preferentially with a C-Mg interaction.[164] The CO/MgO adsorption energy is relatively small and a range of values has been obtained by different experimental techniques and theoretical methods. An adsorption energy of 3.23 kcal/mol was obtained from thermodesorption experiments by Wichtendahl *et al.*[165] whereas temperature-programmed desorption (TPD) experiments performed by Dohnálek *et al.*[166] accounted for an adsorption energy of 4.84 kcal/mol. An experimental study by Xu *et al.* reported an interaction energy of 3.0 kcal/mol.[167] For a more extensive description of the rich experimental history of the MgO/CO adsorption, readers are referred to the review by Spoto *et al.*.[168]

Computationally, the challenge posed by this system is the weak interaction between CO and the surface, mainly arising from van der Waals (vDW) forces. Many local and semi-local Kohn-Sham density functionals[102,103] are unable to account for vDW interactions in such cases.[169–172] The accurate estimation of the adsorption energy, therefore, requires an extensive testing of DFT functionals and the incorporation of dispersion corrections.[173–177]. On the other hand, size-consistent correlated wave-function (CWF)-based *ab initio* methods can model vDW interactions,[169] and in the past few years their application to periodic systems has gained momentum.[44,45,178–183] An attractive feature of CWF methods is their systematic improvability; however, their steep computational-cost scaling with system size poses an obstacle.[7,169] This becomes apparent in applications where one cannot exploit translational symmetry due to the presence of irregularities in the crystal, like point defects or surface adsorbates.

Among the most recent wave-function theoretical studies, Staemmler computed an adsorp-

tion energy of 2.86 kcal/mol using the method of local increments,[169] whereas, using their combined MP2-CCSD(T) approach embedded in a potential of point charges, Boese *et al.*[162] calculated an adsorption energy of 5.0 kcal/mol, but also pointed out the wide range of numbers that can be obtained using different electronic structure theories. Valero *et al.*[160] showed that the Minnesota functionals M06-2X and M06-HF provide adsorption energies of around 6 kcal/mol.

These systems are usually modeled by either cutting a cluster from an extended system (cluster modeling) or by assuming periodic boundary conditions (PBCs). Defining a cluster involves choosing an appropriate cluster size and saturating the free valencies using hydrogen atoms, which can create spurious electronic states at the boundary. Previously used cluster models[162,163,184–188] were surrounded with point charges or periodic potentials to replicate the environment. On the other hand, modeling surface adsorption with PBCs using CWF becomes prohibitively costly due to the apparent need of large supercells (often hundreds of atoms). To overcome the cost and maintain the accuracy of the parent method, the models can be subjected to fragmentation/embedding approaches.[49,162,181,182,189] Quantum embedding methods use a high-level quantum chemistry solver to represent a small region of interest (here referred to as the fragment/impurity), whereas the rest of the system (generally referred to as “environment") is represented using a mean-field method such as KS-DFT[102,103] or Hartree–Fock (HF)[7,11]. Modeling the adsorption of CO to a MgO surface is therefore ideal to investigate the performance of wave function-in-wave function quantum embedding approaches.

In this work, we use the density matrix embedding theory (DMET) algorithm to calculate the adsorption energy of a CO molecule to the MgO(001) surface. DMET, a wave function-in-wave function embedding technique,[104] was originally proposed as a promising alternative to dynamical mean-field theory (DMFT)[190] to treat strongly correlated fermions in the one-dimensional Hubbard model. Several theoretical developments and targeted appli-

cations have followed since.[68,84,85,105,106,114,117,118,191,192] DMET uses the Schmidt decomposition[107] of a mean-field wave function to model the environment of a given impurity space using an effective bath. Pham *et al.*[124] and Cui *et al.*[109] extended the DMET algorithm to periodic systems. Here we use coupled-cluster theory with single and double excitations (CCSD) and second-order Møller-Plesset perturbation theory (MP2) as high-level solvers within the DMET formalism and compare them with non-embedding Γ-point CCSD and MP2 references.

3.2 Theory and Methods

The DMET calculations are performed using our periodic DMET, pDMET, code,[125,193] which utilizes the electron integrals and quantum chemical solvers from the PySCF package.[122,123] Similar to the workflow in Ref. 1, we first perform a HF calculation to obtain the mean-field wave function. Next, we define the impurity region using a set of localized orbitals in real space. Here, we use the maximally-localized Wannier functions (MLWFs)[119,120], implemented in the wannier90[121] code via the pyWannier90 interface.[126]. Since adsorbates (*i.e.*, perturbations to the pristine crystal) are introduced, the Brillouin zone is sampled at the Γ-point and a subset of the MLWFs (which we label as N_{imp}) at the chemical region of interest, for example those around the adsorbate, are chosen to define the impurity. The bath is defined using the Schmidt decomposition.[106] where the environment block (D_{env}) of the one-body reduced density matrix (1-RDM) is diagonalized as follows:

$$D_{\text{env}} = \mathbf{U}\lambda\mathbf{U}^{*} \tag{3.1}$$

where λ is a diagonal matrix of eigenvalues λ_i ($i = 0, 1, ..., N_{\text{env}}$ where N_{env} is the number of the environment orbitals). The columns of the unitary matrix $\mathbf{U}$ corresponding to λ_i other than zero or two define the entangled bath orbitals; the remainder orbitals are treated as a

frozen core in the embedding calculation. The mean-field wave function after the Schmidt decomposition thus has the following form

$$|\Phi\rangle = (\sum_i \lambda_i |f_i\rangle \otimes |b_i\rangle) \otimes |\text{core}\rangle \tag{3.2}$$

where $|f_i\rangle$, $|b_i\rangle$, and $|\text{core}\rangle$ are, respectively, single determinants in the Fock spaces of the N_{imp} impurity orbitals, $N_{\text{bath}} \leq N_{\text{imp}}$ bath orbitals, and N_{core} frozen core orbitals, respectively, and $i = 0, 1, ..., N_{\text{imp}}$. The high-level wave function, $|\Psi_{\text{emb}}\rangle$, diagonalizes the embedding Hamiltonian, $\hat{H}_{\text{emb}}$:

$$\hat{H}_{\text{emb}}|\Psi_{\text{emb}}\rangle = E_{\text{emb}}|\Psi_{\text{emb}}\rangle \tag{3.3}$$

where $\hat{H}_{\text{emb}}$ is the partial trace of the Hamiltonian over the $|\text{core}\rangle$ determinant; its operator terms involve only $N_{\text{emb}} = N_{\text{imp}} + N_{\text{bath}} \leq 2N_{\text{imp}}$ embedding orbitals. For calculations of energy differences it is important to choose the same number of N_{emb} embedding orbitals for the different geometries. As discussed later, the computational cost of the high-level method is thus reduced by not requiring to have N_{core} orbitals in the effective Hamiltonian. We utilize a density fitting (DF) approach based on the Cholesky decomposition,[194–197] where four-center electron repulsion integrals (ERIs) in the embedding space can be reconstructed in terms of the three-center ERIs as:

$$(ij|kl) = \sum_{P,Q}(ij|P)\mathbf{M}^{-1/2}_{PQ}(Q|kl) = \sum_P B^P_{ij}B^P_{kl}, \tag{3.4}$$

where P, Q represent auxiliary basis functions, $\mathbf{M}_{PQ} = (P|Q)$ is the Coulomb metric, and B^P_{ij} and B^P_{kl} are the Cholesky vectors,

$$B^P_{ij} = \sum_Q C^Q_{ij}(Q|P)^{1/2} \tag{3.5}$$

where the expansion coefficients C_{ij}^{R} are obtained by solving a linear equation

$$\sum_{R}(P|R)C_{ij}^{R} = (P|ij). \tag{3.6}$$

The auxiliary basis set contains even-tempered basis (ETB) functions generated with a progression factor $\beta = 2.0$ for the auxiliary expansion of the polarized double-zeta basis set (GTH-DZVP) and polarized triple-zeta basis set (GTH-TZVP) bases, and shall be represented using P and Q. The prefix GTH is used since these basis sets are consistent with the Goedecker-Teter-Hutter pseudopotentials[127,198] that have been used for all the calculations. Our approach is general and applies equally well to pseudopotentials and all-electron basis sets since surface adsorption should primarily depend on valence electrons and orbitals.

In the previous implementations of periodic DMET[109,124] the quantum impurity solvers utilized four-center two-electron integrals obtained by contracting the three-center electron repulsion integrals (ERIs) in the embedding space as in equation 3.4. This eliminated the full-basis 4-index ERI array, but still required the storage of the 4-index ERIs in the embedding basis, whose memory cost scales with the size of the impurity as $\mathcal{O}(N_{\text{imp}}^{4})$.[109,124] On the other hand, in the current implementation, we utilize the DF for the MP2 and CCSD high-level solvers, in which the programmable equations for the energy are implemented in terms of the Cholesky vectors themselves and the $(ij|kl)$ integrals in the embedding basis are not required. In other words, the right-hand side of equation 3.4 is not evaluated but is algebraically substituted into the energy expressions in the high-level solver implementations. The formal memory cost scaling of this approach (with respect to the size of the impurity) is $O(N_{\text{aux}}N_{\text{imp}}^{2})$, which in practice is much more favorable for our applications, as shown later.

We compute the adsorption energy, ΔE, as the difference between the energy at the equilibrium geometry, E_{eq} (C-Mg bond distance 2.479 Å),[162] and at a separated geometry, E_{sep}, (C-Mg bond distance 6 Å) as indicated in Figure 3.1a. The 4x4x2 slab model of MgO has

a vacuum of approximately 16 Å in the vertical direction (collinear to CO) above the MgO surface to avoid the interaction between neighboring images. We consider four choices of impurity clusters as shown in Figure 3.1b). For these four choices, the orbitals are localized on (a) only the CO molecule, (b) the CO molecule and the nearest Mg atom on the substrate (denoted as CO + Mg), (c) the CO molecule, the nearest Mg atom and the 4 nearest O atoms on the substrate (denoted as CO + MgO_4) and finally (d) which includes the 4 next to nearest Mg atoms in addition to (c) (denoted as CO + Mg_5O_4). The orbitals localized at the highlighted atoms in the embedding clusters (Figure 3.1b) have been considered as the fragment. We do not correct for basis set superposition error (BSSE) in our calculations, because this would require the use of ghost basis functions. The Schmidt decomposition is unable to produce bath orbitals entangled to the unoccupied ghost orbitals; therefore, these correction calculations would be systematically deficient in bath orbitals compared to the calculation being corrected. A proper way to account for the most entangled orbitals from the environment is desired especially for physical/chemical phenomena where BSSE is non-negligible and is currently an area we are working on.

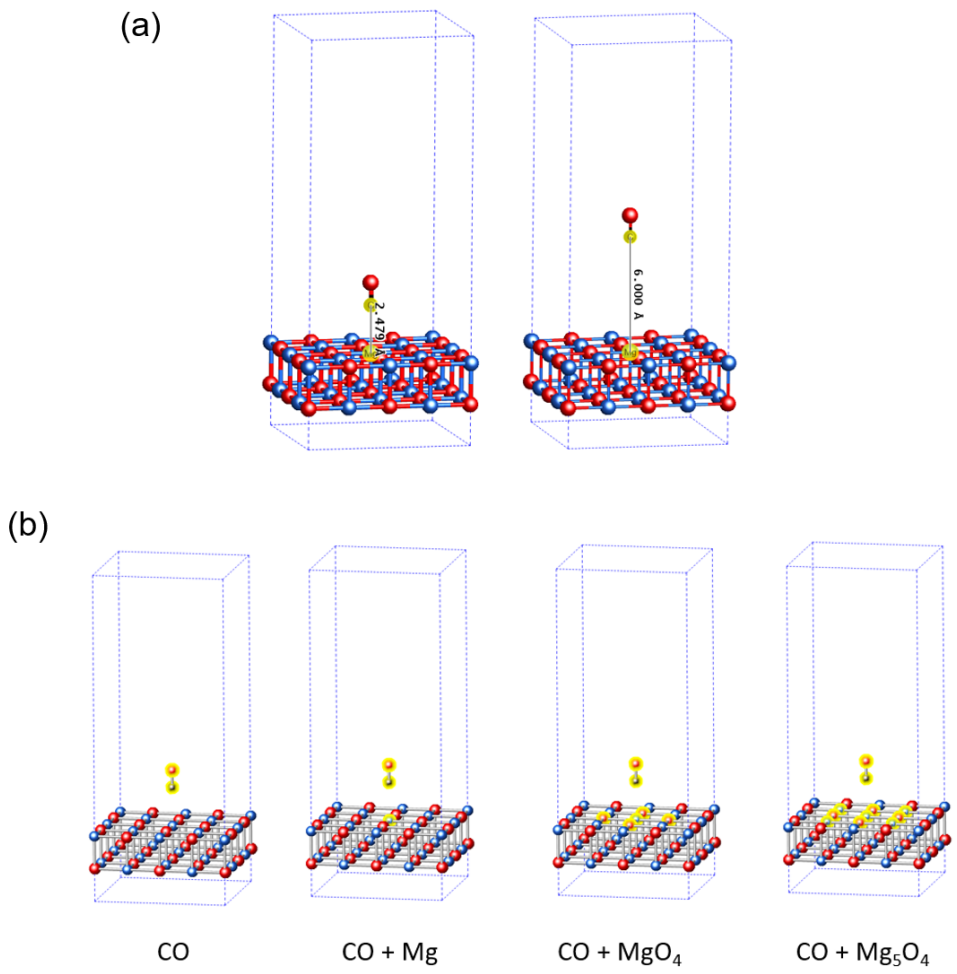

Figure 3.1: (a) CO at a distance of 2.479 Å (left) representing the geometry at equilibrium (referred as eq.) and 6 Å (referred as sep.) from the MgO surface (right) representing the geometry when there is no interaction between the substrate and adsorbate. Magnesium (Mg) atoms are shown in red, oxygen (O) in blue and carbon (C) in gray. (b)Atoms highlighted in yellow form the impurity clusters used for DMET calculations.

3.3 Results and Discussion

In Figure 3.2, we report the relative energy E_{rel} of the CO+MgO model as a function of the distance between C (in CO) and Mg (in MgO) from 2 Å to 6 Å. We take as reference value the total energy at the C-Mg distance of 2.479 Å and E_{rel} at all other geometries are

reported relative to this reference. The results are obtained using periodic MP2 calculations, restricted HF (RHF) and DMET-MP2. The DMET-MP2 calculations are performed using the smaller CO + Mg impurity subspace and the larger CO + MgO_4 impurity subspace.

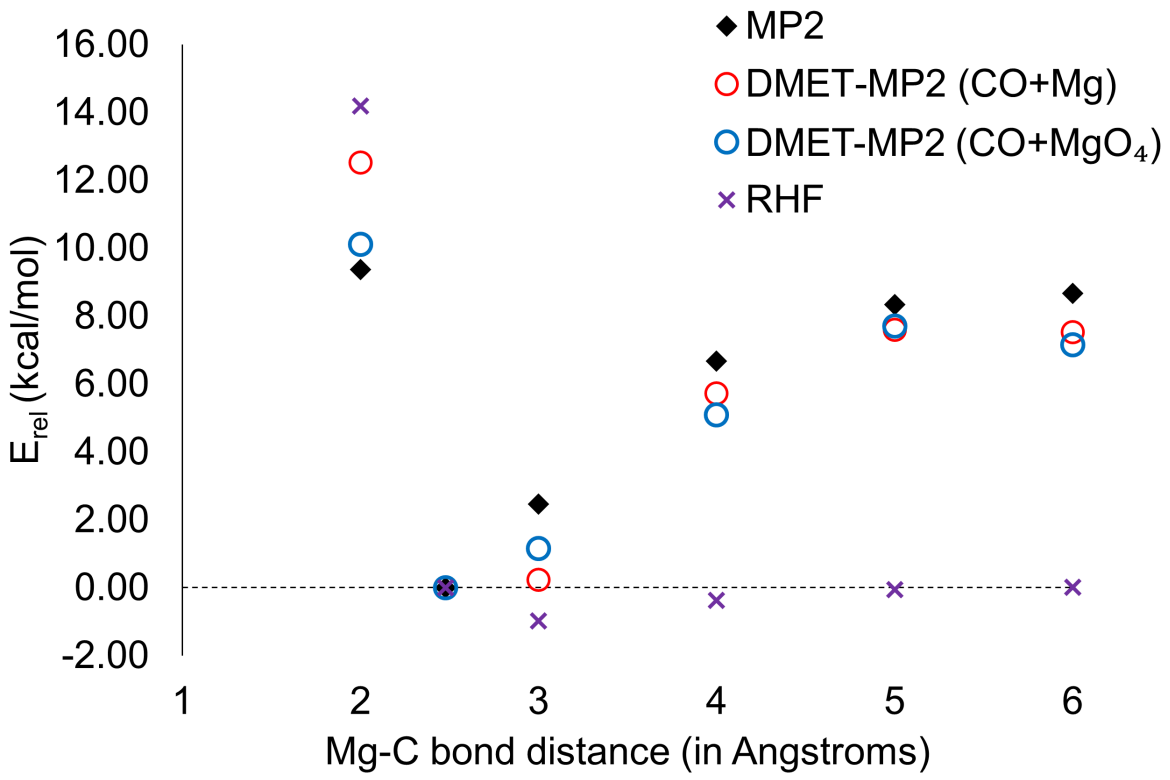

Figure 3.2: Relative energies E_{rel} (in kcal/mol) obtained using non-embedding MP2 (blue diamond), DMET-MP2 with the CO+Mg impurity cluster (red circles), DMET-MP2 with the CO+MgO_4 impurity cluster (dark blue circles) and RHF (purple crosses). The abscissa represents the Mg-C distances in Å. All E_{rel} values are reported as differences with respect to the value at the C-Mg distance of 2.479 Å. All calculations are performed using the DZVP basis set.

For the MP2 reference method, E_{rel} reaches an asymptotic value at a C-Mg distance of 6 Å and differs from E_{rel} at 5 Å by only 0.3 kcal/mol thereby suggesting that 6 Å is a reasonable choice for a separated geometry. Using the CO+MgO_4 fragment, the DMET E_{rel} values at each geometry are within 2 kcal/mol of the MP2 references. Using the CO+Mg fragment, the DMET value at the C-Mg bond distance of 2 Å has a large disagreement (ca. 5 kcal/mol) with the non-embedding reference, suggesting the importance of using a larger fragment space.

The RHF E_{rel} values deviate significantly from the MP2 references. Morover, the RHF E_{rel} values at 3, 4 and 5 Å are negative, thereby indicating the presence of a minimum C-Mg bond length significantly away from the literature value of 2.479 Å.[162] This is consistent with cluster HF calculations by Nygren *et al.*.[199] DMET on the other hand reproduces the binding energy (to within 1.5 kcal/mol) that is predicted by the reference.

Next, DMET calculations with the embedding clusters are compared to the periodic Γ-point CCSD and MP2 calculations (termed as the non-embedding references). The energy differences ΔE calculated using DMET-CCSD and DMET-MP2 with different basis sets are shown in Figure 3.3. The numbers are reported in Tables SI2 and SI3. Four different basis set compositions have been used. They are divided as either DZVP on all the atoms or TZVP on important atoms and DZVP on all the others. TZVP (X) refers to TZVP applied on the X set of atoms and DZVP on all others.

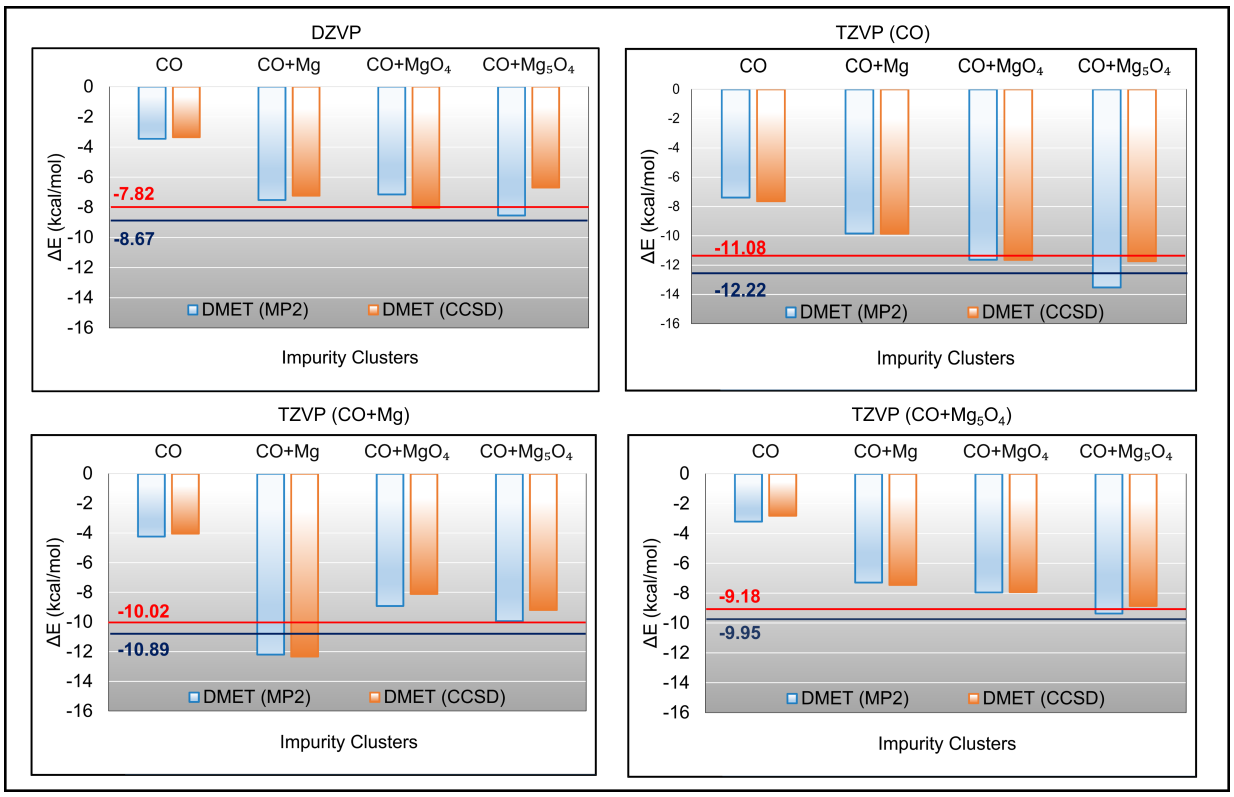

Figure 3.3: Adsorption energies (ΔE) between the equilibrium (2.479 Å) and separated (6 Å) geometries calculated using different basis sets and impurity cluster models. TZVP (X) refers to X being treated with the TZVP basis set and the rest of the system using DZVP basis set. The solid lines correspond to the periodic Γ-point CCSD/MP2 calculations with red/dark blue color coding.

With the two largest impurity clusters, there is a closer agreement with the non-embedding references. This suggests that a larger number of surface atoms in the DMET impurity space is necessary for better accuracy. In Figure SI1, we plot the mean absolute deviations (MADs) from the non-embedding references and report them in Table SI3 of the SI of reference 96. The requirement of bigger impurity clusters implies the storage and manipulation of a higher number of electron repulsion integrals (ERIs). With our DF implementation, we observe a severe reduction in memory requirements. For the test case of the $CO+Mg_5O_4$ fragment at the equilibrium geometry with more than 200 orbitals, the 4c-2e calculation requires 200 Gb of memory on a AMD EPYC 7502 32-Core Processor, while the DF integrals calculation requires 30 Gb of memory. This is because the previous implementation in Refs. 124 and 1

required storage of $O(N_{\text{imp}}^4)$ two-electron integrals, whereas the new implementation requires storage of $O(N_{\text{aux}}N_{\text{imp}}^2)$ decomposed intermediates, where N_{imp} is the number of impurity fragment orbitals and N_{aux} is the number of auxiliary density-fitting orbitals. For large impurity fragments, $N_{\text{imp}}^2 \gg N_{\text{aux}}$ and the storage saving becomes significant. All the calculations use multithreading (*i.e.*, shared memory) only; there is no multiprocessing. It should be noted that Cui *et al.*[109] also mentioned the possible memory efficiency that can be achieved by incorporating a similar algorithm. The current algorithm does not involve a formal speedup in terms of time required for a particular calculation. In this particular example, the 4c-2e calculation requires a wall-time of two hours and twenty one minutes wheras the DF integrals calculation requires a wall-time of one hour and fifty five minutes

Now, we examine the scaling of CCSD-DMET as compared to the reference CCSD calculations. The computational cost of DMET is mainly dominated by the cost of the CCSD calculations within the embedding space. The most expensive term required in CCSD has a scaling of $\mathcal{O}[\mathrm{N}_{\text{vir}}^4 \times \mathrm{N}_{\text{occ}}^2]$, where N_{vir} is the number of virtual orbitals and N_{occ} is the number of occupied orbitals.[200] The primary contribution to the large scaling arises from the virtual orbitals. In the current framework, most of the virtual orbitals are part of the environment (*i.e.* a part of N_{core} orbitals), thereby significantly reducing the cost. If all N_{core} unentangled orbitals are doubly occupied, the scaling of CCSD-DMET becomes $\mathcal{O}[(\mathrm{N}_{\text{vir}})^4(\mathrm{N}_{\text{occ}}-\mathrm{N}_{\text{core}})^2]$; if they are all empty, the scaling of CCSD-DMET becomes $\mathcal{O}[(\mathrm{N}_{\text{vir}} - \mathrm{N}_{\text{core}})^4(\mathrm{N}_{\text{occ}})^2]$.

3.4 Conclusions

In summary, we have used a periodic implementation of DMET to calculate the adsorption energy of the CO molecule with the MgO(001) surface. We have investigated two widely used quantum chemical solvers, CCSD and MP2, as high-level methods. We infer that DMET-CCSD and DMET-MP2 can be used to obtain adsorption energies with high accuracy and at a significantly lower cost compared to the non-embedding references. We additionally

observed that an impurity cluster including at least a MgO_4 moiety on the MgO surface is required for accurate adsorption energies. Therefore, we implemented an efficient way to store and manipulate the memory intensive ERIs within the periodic DMET algorithm. We envision that, with our recent implementation of the multireference solvers [1] such as complete active space self-consistent field (CASSCF) [26–28] and n-electron valence state second-order perturbation theory (NEVPT2), [110–113] this approach can allow us to study bond breaking phenomena of multireference systems on surfaces, at an affordable cost, which would be otherwise non-trivial for mean-field and single reference methods.

Acknowledgement

We thank Hung Q. Pham, Riddhish Pandharkar, Jason Goodpaster, Giullia Galli, Joachim Sauer and Debmalya Ray for insightful discussion. We thank Zhihao Cui, Tianyu Zhu and Garnet K.-L. Chan for sharing with us the Gaussian density fitting transformation code. This work was supported as part of the Inorganometallic Catalysis Design Center, an Energy Frontier Research Center funded by the U.S. Department of Energy, Office of Science, Basic Energy Sciences, under Award DE-SC0012702. M. C. thanks the SURF-CTC program at the University of Minnesota Chemical Theory Center for the summer research fellowship. Computer resources were provided by the Minnesota Supercomputing Institute at the University of Minnesota and the University of Chicago Research Computing Center.

CHAPTER 4

DENSITY MATRIX EMBEDDING USING MULTICONFIGURATION PAIR-DENSITY FUNCTIONAL THEORY

This chapter is reprinted with permissions from *J. Chem. Theory Comput.* **2023**, *19*, 12, 3498–3508

Abstract

We present a quantum embedding method for ground and excited states of extended systems that uses multiconfiguration pair-density functional theory (MC-PDFT) with densities provided by periodic density matrix embedding theory (pDMET). We compute local excitations in oxygen mono- and di-vacancies on a magnesium oxide (100) surface and find absolute deviations within 0.05 eV between pDMET using the MC-PDFT, denoted as pDME-PDFT, and the more expensive, non-embedded MC-PDFT approach. We further use pDME-PDFT to calculate local excitations in larger supercells for the mono-vacancy defect, for which the use of non-embedded MC-PDFT is prohibitively costly.

4.1 Introduction

Quantum embedding methods are promising for accurately describing electron correlation in molecules and materials, especially when correlated wave-function methods become prohibitively expensive due to their poor scaling with system size.[49,63,104,181,182,191,201–205] These methods involve dividing a system into important regions (called impurities or fragments) that are treated with a highly correlated theory, while the rest of the system is

described using a more approximate level of theory, such as Hartree-Fock (HF)[7] or Kohn-Sham density functional theory.[102,103] One particular type of quantum embedding method is density matrix embedding theory (DMET),[68,104–106] which uses a wave function-in-wave function approach and models the environment of the impurity or fragment using a bath constructed from the Schmidt decomposition[107] of a mean-field wave function.

For systems with significant static (strong) correlation, multiconfiguration methods are often used to describe the ground and excited states of molecular systems. The complete active space self-consistent field (CASSCF) method[26–28] expresses the wave function as a linear combination of all possible configuration state functions that can be generated within a defined "active space" of n active electrons occupying N active orbitals. To get accurate electronic excitation energies and reaction energies, post-SCF methods such as the complete active space second-order perturbation theory (CASPT2)[153] or n-electron valence state second-order perturbation theory (NEVPT2)[110–113] can be used, as well as multiconfiguration pair-density functional theory (MC-PDFT).[70,72,206,207]

Multiconfiguration methods are desired as high-level (impurity) solvers in DMET because they can handle extended systems with multiple electronic configurations.[1,114,154] Recently n-electron valence state second-order perturbation theory (NEVPT2) was implemented as a high-level quantum chemical solver within periodic DMET (pDMET) to capture dynamic correlation as a post-CAS-DMET procedure.[1] However, even though NEVPT2-DMET is cheaper than NEVPT2, it scales poorly with the active space size and the parameter space (*i.e.* the number of orbitals in the impurity).[1] A more affordable alternative for capturing electron correlation at the post-SCF level is multiconfiguration pair-density functional theory (MC-PDFT)[70,206,207] and its hybrid version (HMC-PDFT).[208] In a recent benchmark study of 373 vertical excitation energies from the QUESTDB dataset, HMC-PDFT was found to be as accurate or even more accurate than NEVPT2 for excitation energies.[209]

Here, we present a way to calculate the correlation energy starting from a CAS-DMET

wave function using PDFT and hybrid PDFT. Our implementation is designed for systems with periodic boundary conditions (extended systems), specifically inspired by the class of problems we are tackling, such as point defects in crystals. It can be easily adapted to molecular systems with open boundary conditions. Here onwards, we refer to this approach as pDME-PDFT and we employ it to calculate singlet-singlet and singlet-triplet excitation energies in the F and M centers on the (100) surface of magnesium oxide. F centers play an important role in catalysis,[210] energy storage,[211] photoelectrochemical applications[137–139] and are responsible for several physical and chemical properties of MgO.[212] M centers are an aggregate of two adjacent F centers, which also affect the physical and chemical properties of MgO, such as its electrical conductivity, magnetic behavior, and optical properties.[212]

4.2 Theory

4.2.1 Multiconfiguration pair-density functional theory (MC-PDFT)

The MC-PDFT energy for a multiconfiguration (MC) wave function is expressed as:

$$E_{\mathrm{MC-PDFT}} = V_{\mathrm{NN}} + \sum_{pq} h_{pq} D_{pq} + \frac{1}{2} \sum_{pqrs} g_{pqrs} D_{pq} D_{rs} + E_{\mathrm{ot}}[\rho, \Pi] \tag{4.1}$$

Here, V_{NN} is the nuclear–nuclear repulsion energy, p, q, r, and s denote molecular orbitals, h_{pq} and g_{pqrs} are one- and two-electron integrals, D_{pq} are the elements of the one-electron reduced density matrices (1-RDMs) and E_{ot} is a functional of the density (ρ) and the on-top pair-density (Π). The hybrid MC-PDFT energy[208] is expressed as:

$$E_{\mathrm{HMC-PDFT}} = \lambda E_{\mathrm{MCSCF}} + (1 - \lambda) E_{\mathrm{MC-PDFT}} \tag{4.2}$$

Here, E_{MCSCF} is the energy derived from the MC wave function in use and λ is the hybrid parameter which specifies the percentage of MCSCF energy included in the hybridization.

Our calculations were performed using a λ value of 0.25, referred to as tPBE0, in analogy with the PBE0 hybrid density functional theory (DFT) functional.[208,213]

4.2.2 Periodic Density Matrix Embedding Theory (pDMET) and the pDME-PDFT implementation

DMET and its periodic implementation have been discussed in detail previously.[1,68,96,104–106,108,109,117,118] DMET involves a low-level (usually Hartree–Fock) calculation on a whole system followed by a high-level (in our case, CASSCF or NEVPT2) calculation in an unentangled "embedding" subspace consisting of the union of user-specified fragment orbitals and corresponding bath (*i.e.* entangled environment) orbitals identified using the Schmidt decomposition.[106] The 1-RDM and two-body reduced density matrix (2-RDM) of the whole system consist of the 1- and 2-RDMs, respectively, from the high-level calculation in the embedding subspace combined with those from the low-level calculation in the orthogonal "core" subspace. If (as in this work) only one embedded fragment is considered in each calculation and the low-level wave function (here, restricted open-shell HF or ROHF) is spin-symmetry-adapted and closed-shell in the core subspace, then the expressions for the DMET whole-system 1- and

2-RDMs assume the simple forms:

$$D_{ij} = D_{ij}^{\mathrm{LL}} \tag{4.3a}$$

$$D_{uv} = D_{uv}^{\mathrm{HL}} \tag{4.3b}$$

$$D_{iu} = 0 \tag{4.3c}$$

$$d_{ijkl} = d_{ijkl}^{\mathrm{LL}} \tag{4.3d}$$

$$d_{uvwx} = d_{uvwx}^{\mathrm{HL}} \tag{4.3e}$$

$$d_{ijuv} = D_{ij}^{\mathrm{LL}} D_{uv}^{\mathrm{HL}} \tag{4.3f}$$

$$d_{ivuj} = -\frac{1}{2} D_{ij}^{\mathrm{LL}} D_{uv}^{\mathrm{HL}} \tag{4.3g}$$

$$d_{iuvw} = d_{uijk} = d_{iujv} = 0 \tag{4.3h}$$

where indices i, j, k, l and u, v, w, x indicate core and embedding orbitals respectively, and superscripts LL and HL indicate low-level and high-level calculations respectively. (N.B.: the 1- and 2-RDMs have the index-permutation symmetries $D_{pq} = D_{qp}$ and $d_{pqrs} = d_{qpsr} = d_{rspq}$, respectively.) Less generally but more simply, the superscripts LL and HL in Eqs. (4.3) can be ignored, and the indices i, j and u, v can instead be taken to identify doubly-occupied inactive orbitals (in either the embedding or core subspace) and active orbitals (which must be in the embedding subspace) respectively, since the 1- and 2-RDM elements for doubly-occupied orbitals are trivial ($D_{ij} = 2\delta_{ij}$ and $d_{ijkl} = 4\delta_{ij}\delta_{kl} - 2\delta_{il}\delta_{jk}$).

The density and the on-top pair-density are calculated from the 1-RDMs and 2-RDMs obtained from Eqs. (4.3) using the usual formulae:

$$\rho = \sum_{pq} D_{pq} \phi_p(r) \phi_q(r) \tag{4.4}$$

$$\Pi = \frac{1}{2} \sum_{pqrs} d_{pqrs} \phi_p(r) \phi_q(r) \phi_r(r) \phi_s(r) \tag{4.5}$$

and substituted into Eq. (4.1). In the case that we are using hybrid MC-PDFT, the first term of Eq. (4.2) (E_{MCSCF}) is taken as the CAS-DMET total energy. In comparing nonembedded MC-PDFT and pDME-PDFT calculations, the key difference lies in the origin of the 1- and 2-RDMs: for MC-PDFT, they are obtained from a non-embedded CASSCF calculation, while for pDME-PDFT, they are derived from a CAS-DMET calculation, the computational cost of which is directly proportional to the size of the embedding space. The computational savings achieved with CAS-DMET over non-embedded CASSCF stem from freezing core orbitals and optimizing only fragment and bath orbitals, in contrast to a conventional full-system CASSCF calculation, which optimizes the entire orbital space (here, HF orbitals). This results in fewer electronic degrees of freedom for CAS-DMET compared to CASSCF.[1,114]. Note that the implementation of pDME-PDFT differs from the one of NEVPT2-DMET in the following way: while pDME-PDFT evaluates the total energy using the density and on-top pair-density of the whole system (see eqs. 4.4 and 4.5), NEVPT2-DMET applies the NEVPT2 method only to the embedding space. Since pDME-PDFT is agnostic to the way in which the embedding calculation has been performed, it is designed to recover in part the effects of dynamic electron correlation even for inactive electrons, which are not correlated in the underlying trial wave function. In contrast, NEVPT2-DMET can not describe electron correlation beyond the embedding space. Moreover, pDME-PDFT has a lower cost scaling with respect to embedding space size compared to NEVPT2-DMET, making it potentially more advantageous both in terms of accuracy and cost reduction. It is worth noting that the 1- and 2-RDMs are influenced by the core/inactive environment, which means that the results of pDME-PDFT calculations may be affected by the choice of mean-field method used to define the core or inactive space in each embedding calculation.

4.3 Computational Methods

All the DMET calculations were performed using our in-house pDMET and mrh codes[193,215] which utilizes the electron integrals and quantum chemical solvers from PySCF.[122,123] Wannierization was done using the wannier90[121] code via the pyWannier90 interface.[126]The Wannierization step involves constructing maximally-localized Wannier functions (MLWFs)[119,120] from the ROHF molecular orbitals. These localized orbitals are used to select the impurity subspace, followed by a Schmidt decomposition of the impurity-environment block of the 1-RDM to generate entangled bath orbitals. The impurity and entangled bath space form the embedding space where high-level electronic structure solvers like CASSCF are used. The details about the CAS-DMET steps can be found in reference 1. The Goedecker-Teter-Hutter pseudopotentials[127,198] were used for all the calculations. The geometry optimizations were performed at the spin-unrestricted PBEsol level[128] using the Vienna *Ab initio* Simulation Package (VASP).[129–132] The convergence criteria of 10^{-6} eV and 10^{-3} eV/Å were used for the energy and force, respectively. We represent a MgO(100) surface using a single layer of Mg and O with the chemical formula $Mg_{18}O_{18}$. We performed benchmark calculations on two point defects, namely the oxygen mono-vacancy (OV) and a oxygen di-vacancy (OOV). For these systems, we computed singlet-singlet and singlet-triplet excitation energies using CAS-DMET, NEVPT2-DMET and pDME-PDFT. We used the translated PBE functional for both PDFT and hybrid PDFT which are referred to as pDME-tPBE and pDME-tPBE0 respectively. The oxygen mono-vacancy defect is created by removing one neutral oxygen atom at the center of the unit cell. The di-vacancy is created by removing an additional neutral oxygen atom nearest to the mono-vacant oxygen atom. To separate the layer and its periodic images, we used a vacuum of 23.518 Å along the [100] direction. In the DMET calculations, we place a dummy oxygen atom at the vacancy to provide basis functions to span the electron density of the defect. For the mono-vacancy, the dummy oxygen and four nearest atoms Mg atoms are treated using the polarized triple-zeta basis set (GTH-TZVP)

whereas the rest of the atoms are treated with the polarized double-zeta basis set (GTH-DZVP). For the di-vacancy, the dummy oxygens and six nearest Mg atoms are treated using the polarized triple-zeta basis set (GTH-TZVP) whereas the rest of the atoms are treated with the polarized double-zeta basis set (GTH-DZVP). The two and three layered models are constructed by placing non-defective one and two layers of $Mg_{18}O_{18}$ below the first layer respectively. For these models the GTH-TZVP is used for the dummy oxygen and nine nearest atoms (4 O and 5 Mg) while GTH-DZVP is used for all other atoms.

4.4 Results and Discussion

First, we investigate the performance of pDME-PDFT in calculating the $S_0 \rightarrow S_1$ and $S_0 \rightarrow T_1$ excitations of the F-center which is a neutral oxygen mono-vacancy (OV) on the (100) monolayer of MgO. Experimentally, detecting F centers on MgO surfaces presents a challenge due to its surface sensitivity, resulting in a range of $S_0 \rightarrow S_1$ transitions observed between 1-5 eV as reported in Table 4.1.[142–144,216] A quantum mechanics/molecular mechanics (QM/MM) approach, utilizing the multireference configuration interaction method, for a cluster model of the oxygen mono-vacancy predicted excitation energies of 3.24 eV for the $S_0 \rightarrow S_1$ transition and 1.93 eV for the $S_0 \rightarrow T_1$ transition.[145] The MgO lattice is composed of Mg^{2+} and O^{2-} ions, and when an oxygen atom is removed, it leaves behind two electrons in the defect site that occupy two defect-localized states between the valence band maximum (VBM) and the conduction band minimum (CBM). The computational model is illustrated in Figure 4.1a. To examine how the excitation energies vary with the embedding space, we consider three impurity clusters of increasing size, as depicted in Figure 4.1b. Figure 4.1c shows the two active natural orbitals used for the minimal (2,2) active space in all calculations presented in Figures 4.1a and 4.1b. This active space has been used previously for the F-center.[1,216] The two active orbitals have a_{1g} and a_{2u} symmetry in the D_{4h} point group. The natural orbitals shown in Figure 4.1c are obtained from the converged

non-embedded CASSCF calculations (used in the subsequent MC-PDFT calculations). The natural orbitals derived from the embedded CAS-DMET calculations, which are employed in the corresponding pDMET-PDFT calculations, qualitatively represent the same active space.

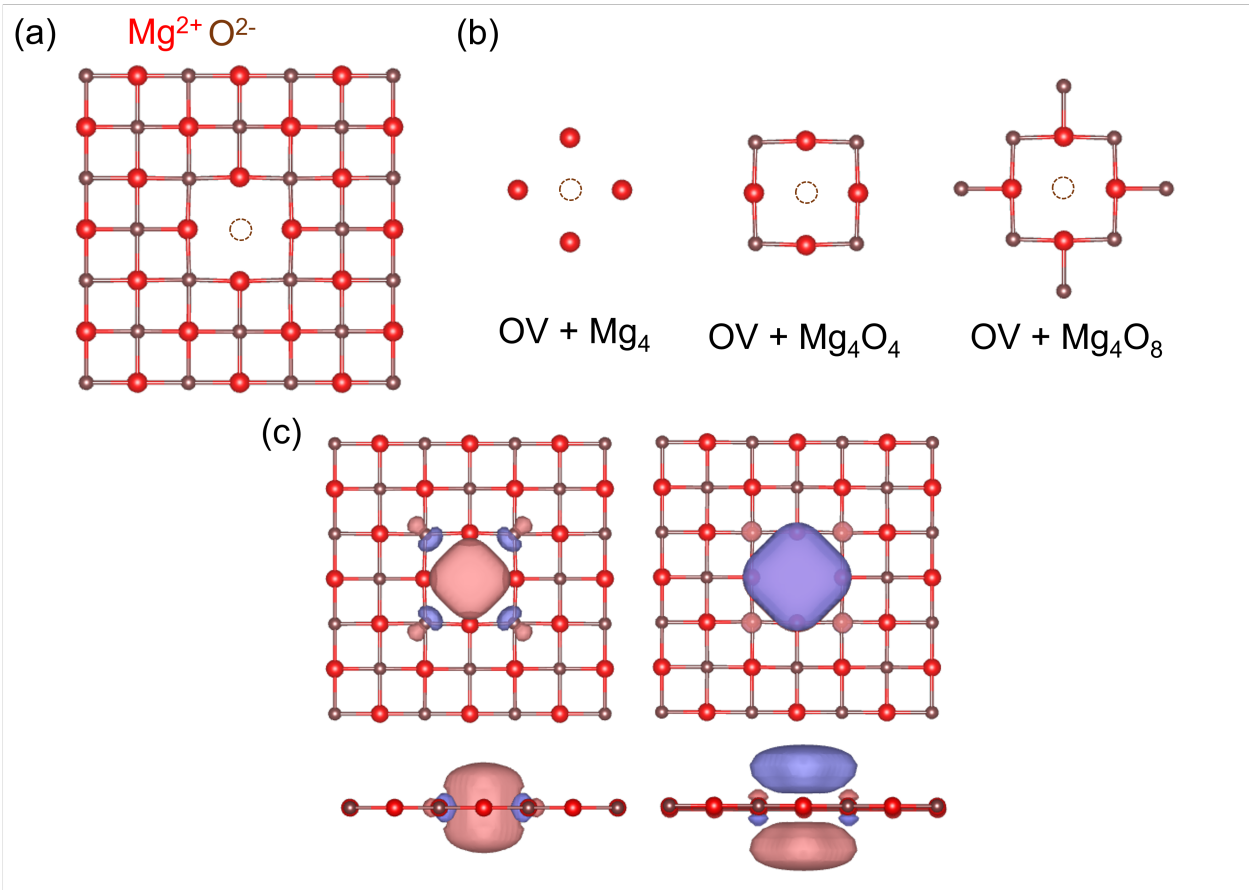

Figure 4.1: Oxygen mono-vacancy on a $Mg_{18}O_{18}$ layer: (a) Top view of the F-center on the (100) surface. (b) Three different impurity clusters considered in the DMET calculations. (c) Top and side view of two defect natural orbitals from the converged CASSCF calculation considered in the (2,2) active space. The isosurface of orbitals is 0.03. This figure has been adapted from reference 1.

In Figures 4.2a and 4.2b, we show the vertical excitation energies of the $S_0 \rightarrow T_1$ and $S_0 \rightarrow S_1$ transitions in the OV system, respectively, as a function of the inverse of the number of embedding orbitals, using the minimal (2,2) active space. Specifically, the plot of excitation energies is shown as a function of $N_{\mathrm{AO}}/N_{\mathrm{emb}}$ where N_{AO} represents the total number of basis

functions in the system considered (here $Mg_{18}O_{18}$) and N_{emb} is the number of embedding orbitals in the impurity clusters considered. We compare them to the corresponding non-embedded results represented by hollow markers. The values are reported in Table 4.1. The excitation energies computed using pDME-tPBE and pDME-tPBE0 agree to within 0.06 eV of the non-embedded reference values for all impurity clusters considered. NEVPT2-DMET, on the other hand, shows a higher sensitivity to the impurity cluster . This is expected since NEVPT2-DMET cannot describe electron correlation outside the embedding space. Considering the $S_0 \rightarrow T_1$ gap, for example, the NEVPT2-DMET difference with respect to the non-embedding reference ranges from 0.17 eV to 0.05 eV. As previously done for NEVPT2-DMET[1], the linear dependence of the excitation energies with respect to the inverse of the number of embedding orbitals was utilized to extrapolate the non-embedding limit. Here, the non-embedding limit corresponds to the point where N_{AO}/N_{emb} =1, *i.e.* $N_{emb} = N_{AO}$. All the extrapolated values lie within 0.05 eV of the non-embedding reference. This extrapolation is represented using dashed lines in Figure 4.2.

In Figure 4.2c and Figure 4.2d, we plot the vertical excitation energies using a (2,8) active space as was used in reference 1. The corresponding numbers are reported in Table 4.1. The active orbitals are reported in the SI of reference 97. The excitation energies obtained from various non-embedding correlated theories exhibit closer agreement with one another in the larger (2,8) active space, providing a means of evaluating the performance of DME-PDFT for both smaller (2,2) and larger (2,8) active spaces. For the (2,8) active space, all pDME-tPBE and tPBE0 excitation energies agree to within 0.05 eV of the non-embedding references, whereas NEVPT2-DMET shows a higher (although not very significant) sensitivity to the impurity cluster. To quantify the sensitivity of the excitation energies to the embedding space we report the slopes for all the linear extrapolations in Tables S2 and S3 of the SI of reference 97.

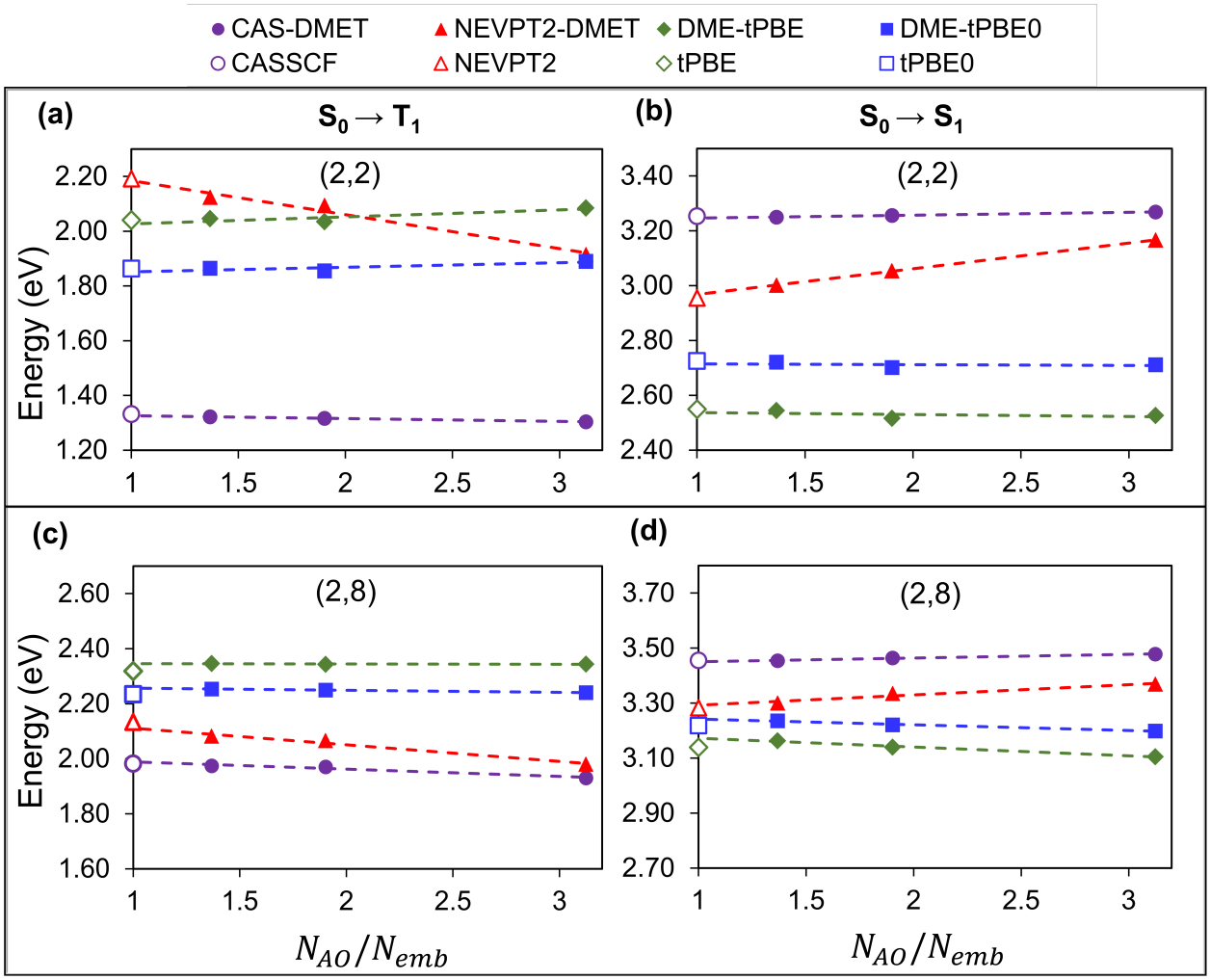

Figure 4.2: Excitation energies of OV defect in $Mg_{18}O_{18}$ layer using ROHF bath and active spaces of (2,2) and (2,8) calculated by CAS-DMET (purple circles), NEVPT2-DMET (red triangles), pDME-tPBE (dark green diamonds), and pDME-tPBE0 (blue squares) for $S_0 \rightarrow T_1$ (a,c) and $S_0 \rightarrow S_1$ (b,d) excitations as a function of $N_{\mathrm{AO}}/N_{\mathrm{emb}}$. Dashed lines are used for extrapolation, and reference energies from CASSCF (purple), NEVPT2 (red), tPBE (dark green), and tPBE0 (blue) are shown for comparison. N_{AO} is the total number of basis functions in $Mg_{18}O_{18}$ and N_{emb} is the number of embedding orbitals in the impurity clusters considered. Here N_{AO} is 506.

Table 4.1: Vertical excitation energies (in eV) of the oxygen mono-vacancy on the $Mg_{18}O_{18}$ layer obtained using DMET with CASSCF, NEVPT2, MC-PDFT (tPBE) and HMC-PDFT (tPBE0). The extrapolated CAS-DMET, NEVPT2-DMET, tPBE-DMET and tPBE0-DMET energies from the linear regression are labeled as "Extrap". "Reference" here indicates the non-embedded Γ-point CASSCF, NEVPT2, tPBE and tPBE0 calculations.

Excitation	Active Space	Impurity cluster	CASSCF	NEVPT2	tPBE	tPBE0	Literature
$S_0 \rightarrow T_1$	(2,2)	OV+Mg_4	1.30	1.91	2.09	1.89	
		OV+Mg_4O_4	1.32	2.09	2.03	1.86	
		OV+Mg_4O_8	1.32	2.12	2.05	1.87	
		Extrap	1.33	2.18	2.03	1.85	
	Reference		1.33	2.19	2.04	1.86	
	(2,8)	OV+Mg_4	1.93	1.98	2.34	2.24	1.93 (MRCI)[145]
		OV+Mg_4O_4	1.97	2.07	2.34	2.25	
		OV+Mg_4O_8	1.97	2.08	2.35	2.25	
		Extrap	1.99	2.18	2.35	2.26	
	Reference		1.98	2.13	2.32	2.23	
$S_0 \rightarrow S_1$	(2,2)	OV+Mg_4	3.27	3.17	2.53	2.71	
		OV+Mg_4O_4	3.26	3.05	2.52	2.70	
		OV+Mg_4O_8	3.25	3.00	2.54	2.72	
		Extrap	3.25	2.97	2.54	2.71	
	Reference		3.25	2.95	2.55	2.72	3.24 (MRCI)[145]
	(2,8)	OV+Mg_4	3.48	3.37	3.11	3.20	2.30 (Exp)[142]
		OV+Mg_4O_4	3.46	3.34	3.14	3.22	1.0, 1.3, 2.4, 3.4 (Exp)[143]
		OV+Mg_4O_8	3.45	3.30	3.16	3.24	1.2, 3.6, 5.3 (Exp)[144]
		Extrap	3.45	3.29	3.17	3.24	
	Reference		3.45	3.30	3.16	3.24	

Reference 1 investigated the impact of the choice of mean-field bath on the accuracy of CAS-DMET and NEVPT2-DMET excitation energies. It was found that the ROHF bath outperformed the RHF bath, and as a result, we have used the ROHF bath for all calculations

in this work. Although exploring the sensitivity of pDME-PDFT excitation energies to different low-level mean-field baths is an interesting area of research, it falls outside the scope of this study. It is worth noting that the 1- and 2-RDMs used to construct the densities, as discussed in Section 2.2, are dependent on the inactive/core subspace, which underscores the importance of selecting an appropriate mean-field method. Next, we investigate the $S_0 \rightarrow S_1$ and $S_0 \rightarrow T_1$ excitations of the M-center, which is a neutral oxygen di-vacancy (OOV) on the (100) monolayer of MgO. This defect is also known as the M centre. Here, the removal of two neutral oxygen atoms leaves four electrons in the cavity created by the two missing oxygens. In the singlet ground state these electrons occupy the two defect-localized states present between the VBM and the CBM.[216] Experimentally, Kramer *et al.* tentatively assigned the 1.0 eV and 1.3 eV adsorption peaks to the M center on thin films of MgO.[143] The computational model is shown in Figure 4.3a. We consider four impurity clusters as shown in Figure 4.3b. We show the five active natural orbitals forming the minimal (4,5) active space in Figure 4.3c. The natural orbitals shown in Figure 4.3c are obtained from the converged non-embedded CASSCF calculations (used in the subsequent MC-PDFT calculations). The natural orbitals derived from the embedded CAS-DMET calculations, which are employed in the corresponding pDMET-PDFT calculations, qualitatively represent the same active space.

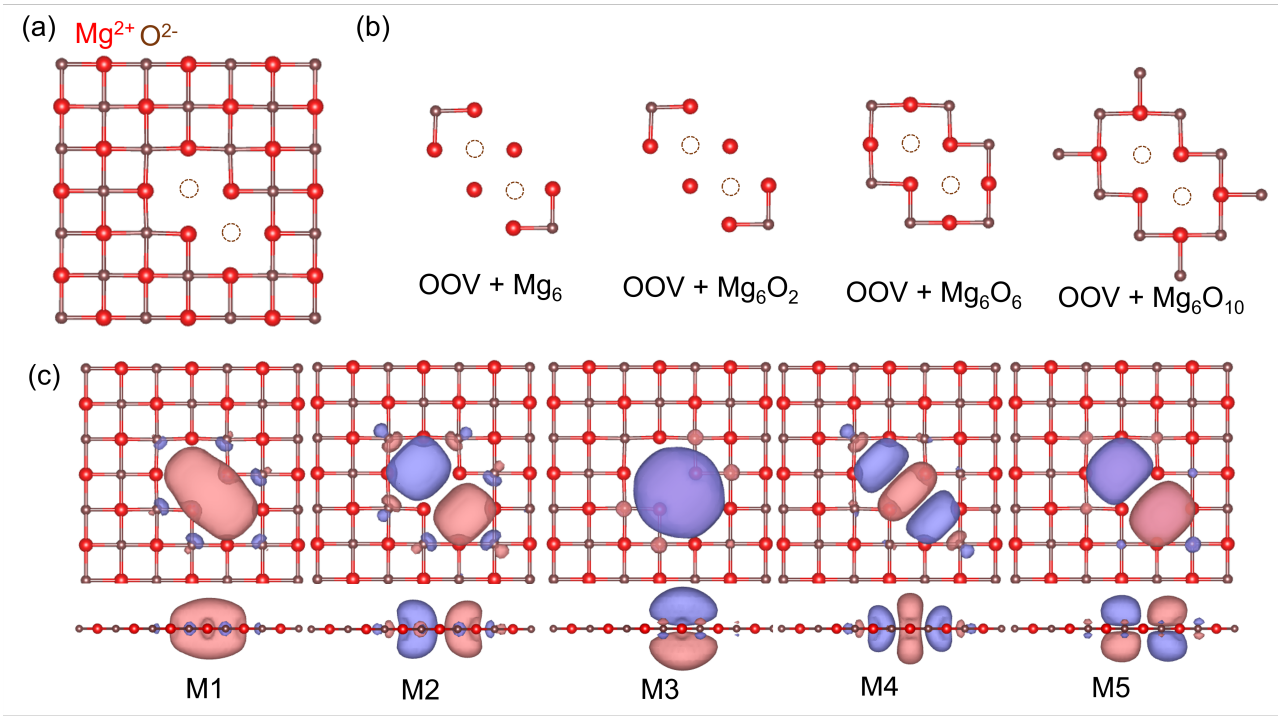

Figure 4.3: Oxygen di-vacancy on a $Mg_{18}O_{18}$ layer: (a) Top view of the M-center on the (100) surface. (b) Four different impurity clusters considered in the DMET calculations. (c) Top and side view of five defect natural orbitals from the converged CASSCF calculation considered in the (4,5) active space. The isosurface of orbitals is 0.02.

In Figure 4.4, we present the vertical excitation energies for the OOV system. The corresponding numbers are reported in Table 4.2. Although the excitation energies calculated using pDME-tPBE0 for the three larger fragments OOV+Mg_6O_2, OOV+Mg_6O_6 and OOV+Mg_6O_{10} are within 0.07 eV of the corresponding non-embedded calculations, the smallest fragment OOV+Mg_6 deviates by 0.14 eV for the $S_0 \rightarrow T_1$ gap. This highlights the inadequacy of the smallest impurity cluster (OOV+Mg_6) in providing an accurate approximation of the overall system densities. Therefore, when extrapolating to the non-embedding limit, only the three larger fragments are taken into account. The excitation energies for the OOV+Mg_6 impurity cluster clearly fall outside the range of the linear extrapolation, as indicated by the detailed analysis presented in Section S01 of the Supporting Information of reference 97, which includes R^2 values for the linear fits. The results for the OOV system

appear to be slightly more sensitive, as indicated by the slopes of the linear extrapolations in Table S3 of the SI of reference 97, compared to those of the F-center. The S_0, S_1, and T_1 configurations are primarily composed of the first three active orbitals, represented by M1, M2, and M3 in Figure 4.3c. These orbitals closely align with the a_1, b_1, and a_2 orbitals in the C_{2v} point group. While the S_0 state is primarily composed of the $M1^2M2^2$ configuration, both the S_1 and T_1 states are dominated by configurations resulting from a M2 $\rightarrow$ M3 transition.

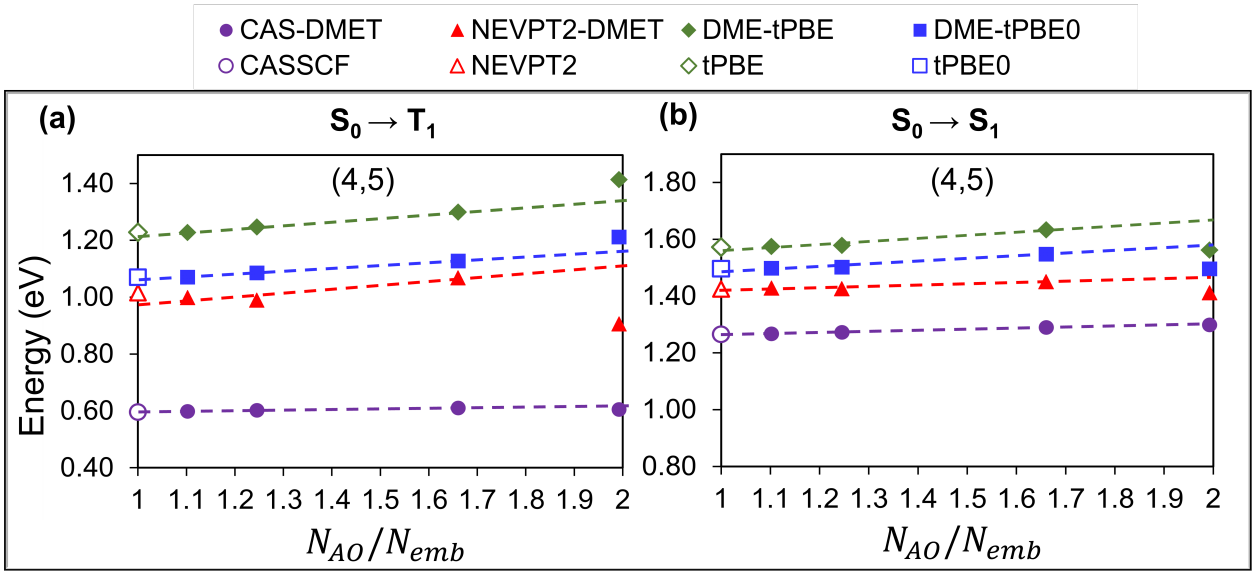

Figure 4.4: Excitation energies of OV in MgO layer using ROHF bath and (4,5) active space for $S_0 \rightarrow T_1$ (a) and $S_0 \rightarrow S_1$ (b) calculated by CAS-DMET (purple circles), NEVPT2-DMET (red triangles), pDME-tPBE (dark green diamonds), and pDME-tPBE0 (blue squares) as a function of $N_{\mathrm{AO}}/N_{\mathrm{emb}}$. Reference energies from CASSCF (purple), NEVPT2 (red), tPBE (dark green), and tPBE0 (blue) are shown for comparison. Here N_{AO} is 518.

Table 4.2: Vertical excitation energies (in eV) of the oxygen divacancy on the MgO(100) surface obtained using CAS-DMET, NEVPT2-DMET, pDME-tPBE and pDME-tPBE0, with an active space of 4 electrons in 5 orbitals. The extrapolated energies from linear regression of the last three points are labeled as "Extrap". "Reference" here indicates the non-embedded Γ-point CASSCF, NEVPT2, tPBE and tPBE0 calculations.

Excitation	Layers	Impurity cluster	CASSCF	NEVPT2	tPBE	tPBE0	Literature
$S_0 \rightarrow T_1$	$Mg_{18}O_{18}$	OOV+Mg_6	0.61	0.91	1.41	1.21	
		OOV+Mg_6O_2	0.61	1.07	1.30	1.13	
		OOV+Mg_6O_6	0.60	0.99	1.25	1.09	
		OOV+Mg_6O_{10}	0.60	1.00	1.23	1.07	
		Extrap	0.60	0.97	1.21	1.06	
	Reference		0.60	1.02	1.23	1.07	
$S_0 \rightarrow S_1$	$Mg_{18}O_{18}$	OOV+Mg_6	1.30	1.41	1.56	1.50	
		OOV+Mg_6O_2	1.29	1.45	1.63	1.55	2.00 (CASPT2)[216]
		OOV+Mg_6O_6	1.27	1.43	1.58	1.50	1.19 (TD-DFT)[216]
		OOV+Mg_6O_{10}	1.27	1.43	1.57	1.50	1.0, 1.3 (Exp)[143]
		Extrap	1.26	1.42	1.56	1.48	
	Reference		1.27	1.43	1.58	1.50	

Next, we explore electronic excitations in the oxygen mono-vacancy on MgO surfaces containing two and three layers, where the corresponding non-embedding calculations are prohibitively costly. The active spaces used are (2,2) and (2,8). The computational model used for the OV defect in 2 layers of MgO ($Mg_{36}O_{36}$), the impurity clusters used in the embedding calculations and the natural active orbitals in the minimal (2,2) active space are shown in figures 4.5a, 4.5b and 4.5c, respectively. Since the non-embedding calculations are prohibitive, the natural orbitals shown in Figure 4.5c are obtained from the largest converged CAS-DMET calculations.

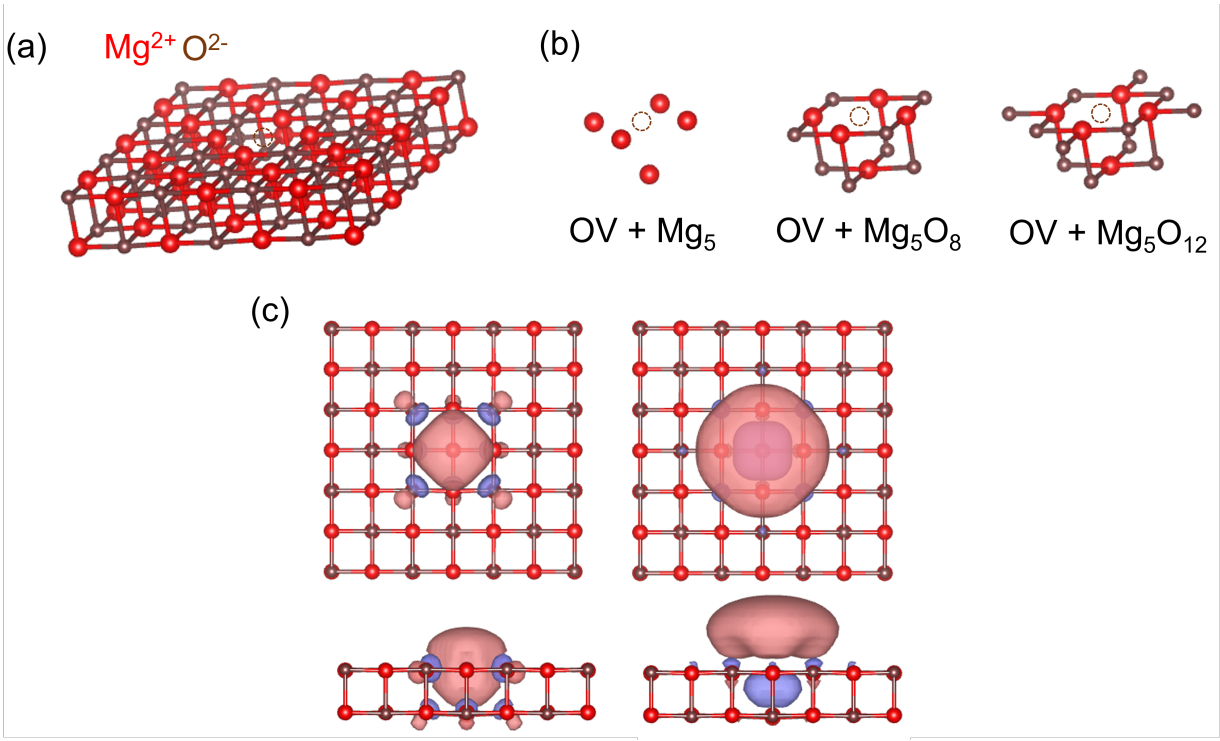

Figure 4.5: Oxygen mono-vacancy on a $Mg_{36}O_{36}$ surface: (a) F-center on the (100) surface. (b) Three different impurity clusters considered in the DMET calculations. (c) Top and side view of two defect natural orbitals from the converged CAS-DMET calculation considered in the (2,2) active space. The isosurface of orbitals is 0.02.

The vertical excitation energies for the OV defect in $Mg_{36}O_{36}$ obtained from the embedding calculations are plotted in Figure 4.6 and reported in Table 4.3. NEVPT2-DMET, pDME-tPBE and pDME-tPBE0 increase the $S_0 \rightarrow T_1$ excitation energy and decrease the $S_0 \rightarrow T_1$ excitation energy as compared to the corresponding CAS-DMET values. The correction is more prominent for the (2,2) active space since CAS-DMET is expected to capture a smaller percentage of the dynamic correlation effects than that of the (2,8) active space. Overall, the extrapolated NEVPT2-DMET and pDME-tPBE0 excitation energies agree within 0.5 eV of each other.

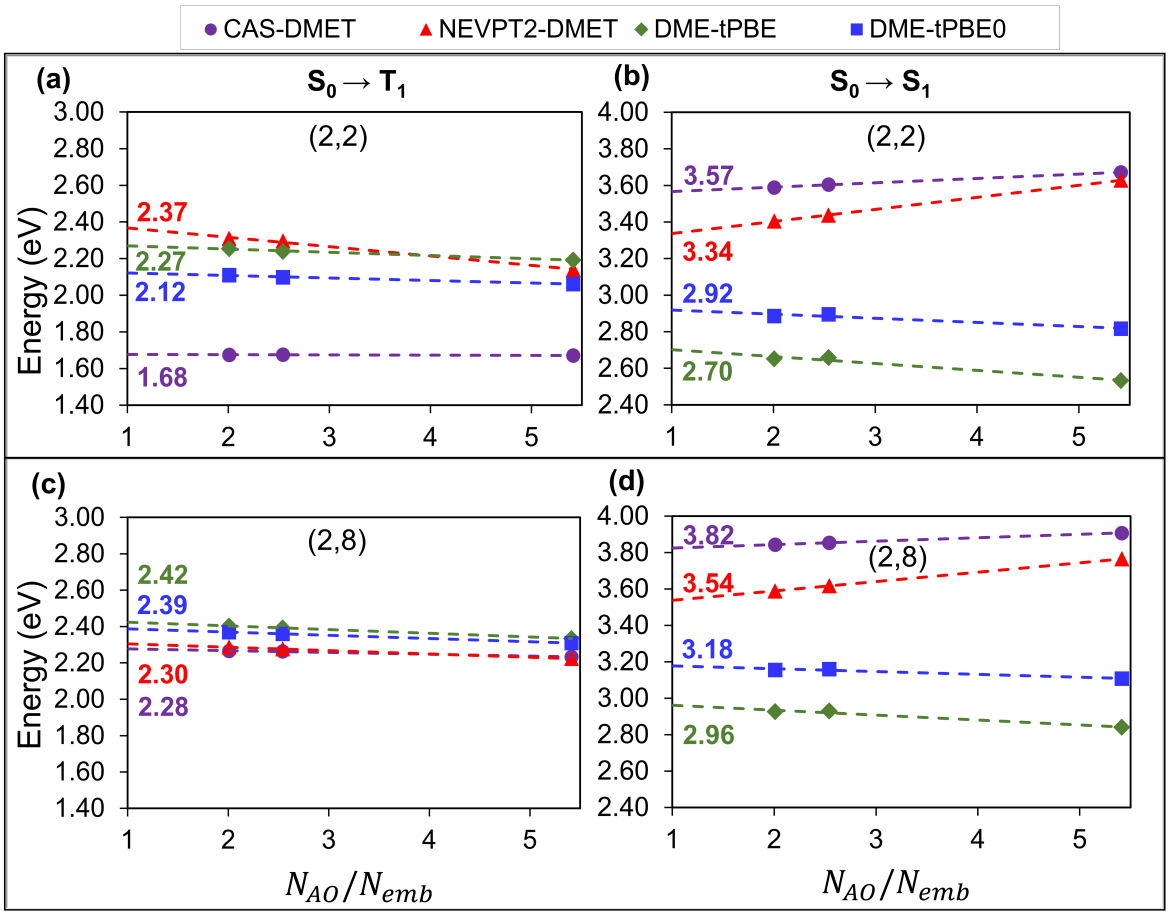

Figure 4.6: Excitation energies of OV defect in $Mg_{36}O_{36}$ surface using ROHF bath and active spaces of (2,2) and (2,8) calculated by CAS-DMET (purple circles), NEVPT2-DMET (red triangles), pDME-tPBE (dark green diamonds), and pDME-tPBE0 (blue squares) for $S_0 \rightarrow T_1$ (a,c) and $S_0 \rightarrow S_1$ (b,d) excitations as a function of $N_{\mathrm{AO}}/N_{\mathrm{emb}}$. All energies are extrapolated to the non-embedding limit, and N_{AO} represents the number of basis functions and N_{emb} is the number of embedding orbitals. Here N_{AO} is 996.

Table 4.3: Vertical excitation energies (in eV) of the oxygen mono-vacancy on the $Mg_{36}O_{36}$ surface obtained using DMET with CASSCF, NEVPT2, MC-PDFT (tPBE) and HMC-PDFT (tPBE0). The extrapolated CAS-DMET, NEVPT2-DMET, tPBE-DMET and tPBE0-DMET energies from the linear regression are labeled as "Extrap".

Excitation	Active Space	Impurity cluster	CASSCF	NEVPT2	tPBE	tPBE0	Literature
$S_0 \rightarrow T_1$	(2,2)	OV+Mg_5	1.67	2.14	2.19	2.06	
		OV+Mg_5O_8	1.68	2.30	2.24	2.10	
		OV+Mg_5O_{12}	1.67	2.31	2.25	2.11	
		Extrap	1.68	2.37	2.27	2.12	
	(2,8)	OV+Mg_5	2.23	2.22	2.33	2.31	
		OV+Mg_5O_8	2.26	2.28	2.39	2.36	1.93 (MRCI)[145]
		OV+Mg_5O_{12}	2.27	2.29	2.40	2.37	
		Extrap	2.28	2.30	2.42	2.39	
$S_0 \rightarrow S_1$	(2,2)	OV+Mg_5	3.91	3.76	2.84	3.11	
		OV+Mg_5O_8	3.85	3.62	2.93	3.16	
		OV+Mg_5O_12	3.84	3.59	2.93	3.16	
		Extrap	3.82	3.54	2.96	3.15	
	(2,8)	OV+Mg_5	3.91	3.76	2.84	3.11	3.24 (MRCI)[145]
		OV+Mg_5O_8	3.85	3.62	2.93	3.16	2.30 (Exp)[142]
		OV+Mg_5O_12	3.84	3.59	2.93	3.16	1.0, 1.3, 2.4, 3.4 (Exp)[143]
		Extrap	3.82	3.54	2.96	3.15	1.2, 3.6, 5.3 (Exp)[144]

In the three-layer case, like in the example above, the non-embedding calculations are prohibitively costly. The active spaces used are (2,2) and (2,8). The computational model used for the OV defect in 3 layers of MgO ($Mg_{54}O_{54}$), the impurity clusters used in the embedding calculations and the natural active orbitals in the minimal (2,2) active space are shown in figures 4.7a, 4.7b and 4.7c respectively. As in the two-layer case, the natural orbitals shown here in Figure 4.7c are obtained from the largest converged CAS-DMET calculations.

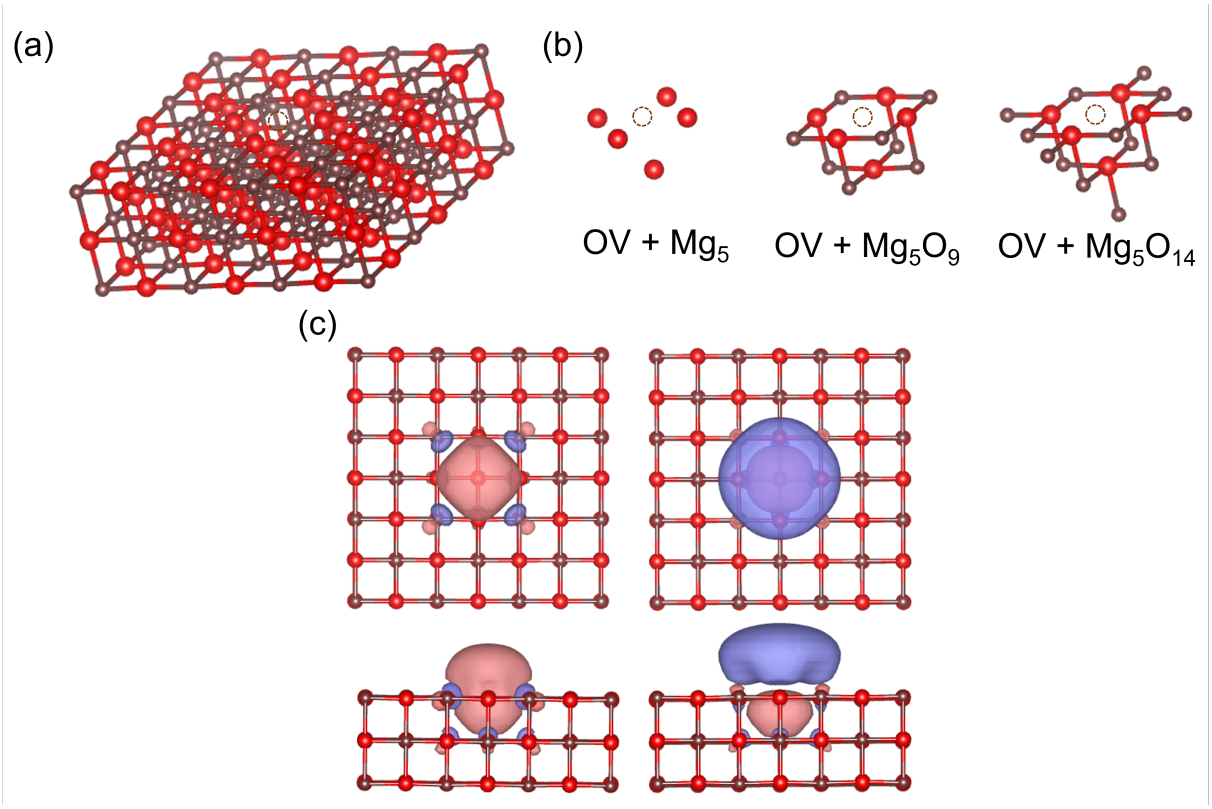

Figure 4.7: Oxygen mono-vacancy on a $Mg_{54}O_{54}$ layer: (a) F-center on the (100) surface. (b) Three different impurity clusters considered in the DMET calculations. (c) Top and side view of four defect natural orbitals from the converged CAS-DMET calculation considered in the (2,2) active space. The isosurface of orbitals is 0.02.

The vertical excitation energies for the OV defect in $Mg_{54}O_{54}$ obtained from the embedding calculations are plotted in Figure 4.8 and reported in Table 4.4. Like in the $Mg_{36}O_{36}$case, for the (2,2) active space, pDME-tPBE, pDME-tPBE0 and NEVPT2-DMET increase the $S_0 \rightarrow T_1$ excitation and decrease the $S_0 \rightarrow S_1$ excitation compared with CAS-DMET. Interestingly, NEVPT2-DMET and pDME-tPBE0 disagree with each other in the $S_0 \rightarrow S_1$ excitation energy, by 0.76 eV and 0.64 eV for the (2,2) and (2,8) active spaces, respectively.

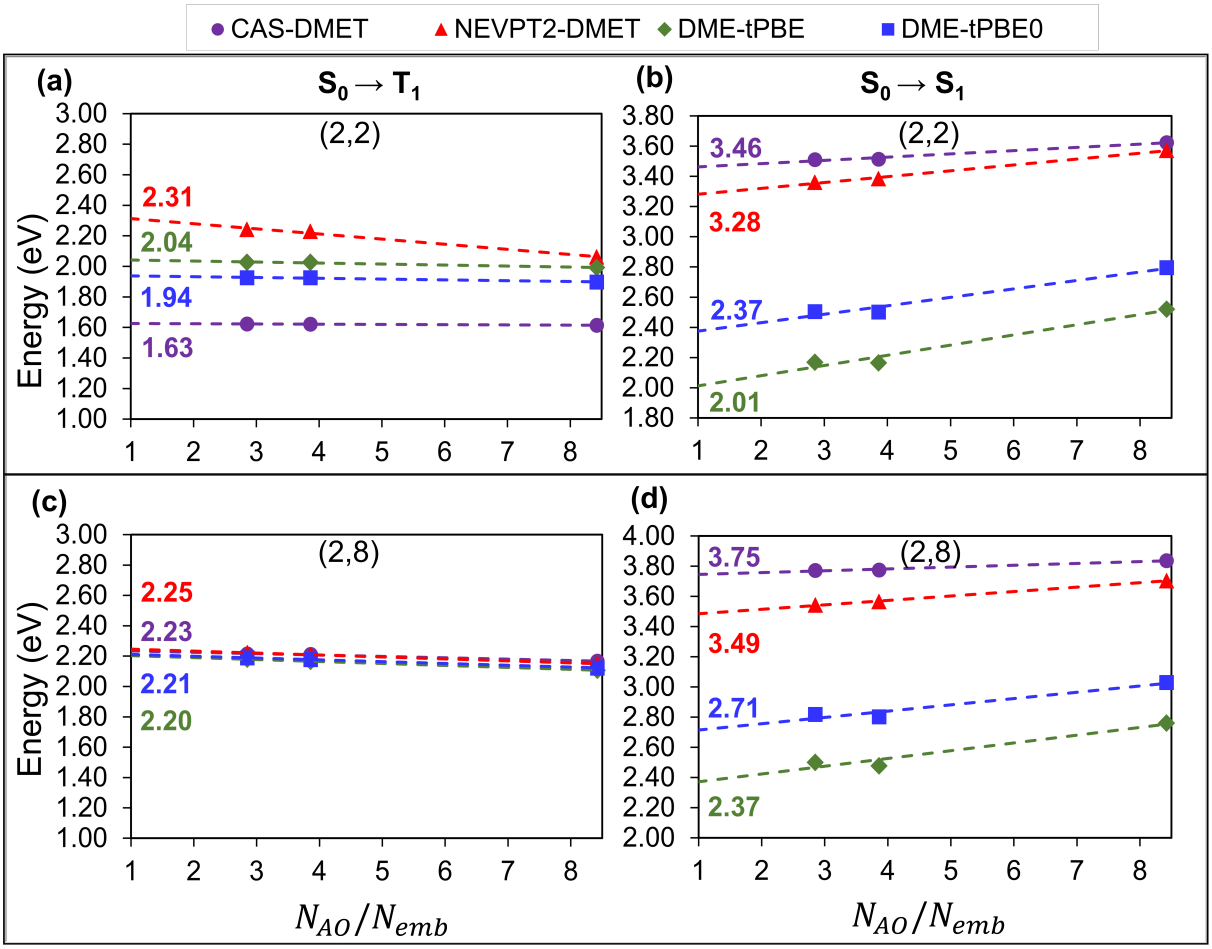

Figure 4.8: Excitation energies of OV defect in $Mg_{54}O_{54}$ surface using ROHF bath and active spaces of (2,2) and (2,8) calculated by CAS-DMET (purple circles), NEVPT2-DMET (red triangles), pDME-tPBE (dark green diamonds), and pDME-tPBE0 (blue squares) for $S_0 \rightarrow T_1$ (a,c) and $S_0 \rightarrow S_1$ (b,d) excitations as a function of $N_{\mathrm{AO}}/N_{\mathrm{emb}}$. All energies are extrapolated to the non-embedding limit, and N_{AO} represents the number of basis functions and N_{emb} is the number of embedding orbitals. Here N_{AO} is 1482.

Table 4.4: Vertical excitation energies (in eV) of the oxygen mono-vacancy on the $Mg_{54}O_{54}$ surface obtained using DMET with CASSCF, NEVPT2, MC-PDFT (tPBE) and HMC-PDFT (tPBE0). The extrapolated CAS-DMET, NEVPT2-DMET, tPBE-DMET and tPBE0-DMET energies from the linear regression are labeled as "Extrap".

Excitation	Active Space	Impurity cluster	CASSCF	NEVPT2	tPBE	tPBE0	Literature
$S_0 \rightarrow T_1$	(2,2)	OV+Mg_5	1.61	2.06	1.99	1.90	
		OV+Mg_5O_8	1.62	2.23	2.03	1.93	
		OV+Mg_5O_{12}	1.62	2.24	2.03	1.93	
		Extrap	1.63	2.31	2.04	1.94	
	(2,8)	OV+Mg_5	2.17	2.15	2.11	2.12	
		OV+Mg_5O_8	2.21	2.21	2.17	2.18	1.93 (MRCI)[145]
		OV+Mg_5O_{13}	2.21	2.22	2.18	2.19	
		Extrap	2.23	2.25	2.21	2.20	
$S_0 \rightarrow S_1$	(2,2)	OV+Mg_5	3.62	3.57	2.52	2.80	
		OV+Mg_5O_8	3.51	3.38	2.16	2.50	
		OV+Mg_5O_{13}	3.51	3.36	2.17	2.51	
		Extrap	3.46	3.28	2.01	2.37	
	(2,8)	OV+Mg_5	3.84	3.70	2.76	3.03	3.24 (MRCI)[145]
		OV+Mg_5O_8	3.78	3.57	2.48	2.80	2.30 (Exp)[142]
		OV+Mg_5O_{13}	3.77	3.54	2.50	2.82	1.0, 1.3, 2.4, 3.4 (Exp)[143]
		Extrap	3.65	3.30	2.38	2.70	1.2, 3.6, 5.3 (Exp)[144]

4.5 Conclusion

We developed a new electronic stucture method, called pDME-PDFT, based on density matrix embedding theory and multiconfiguration pair-density functional theory, able to treat extended systems with periodic boundary conditions. Initial applications on oxygen vacancies in magnesium oxide showed that produces results that are comparable to the more expensive non-embedded MC-PDFT method. We then used pDME-PDFT to study larger

models, namely the $Mg_{36}O_{36}$ and $Mg_{54}O_{54}$ surfaces, which are impractical to investigate with non-embedded MC-PDFT. Finally, pDME-PDFT gives results comparable with the more expensive and in many cases non-affordable NEVPT2-DMET method. We envision that pDME-PDFT will be used to investigate the electronic properties of defects in materials, as well as reactions on surfaces involving multireference systems.

Acknowledgement

We thank Gautam Stroscio and Soumi Haldar for insightful discussion. This material is based upon work supported by the U.S. Department of Energy Office of Science National Quantum Information Science Research Centers. This work was also partially funded by the Division of Chemical Sciences, Geosciences, and Biosciences, Office of Basic Energy Sciences of the U.S. Department of Energy through Grant DE-SC002183. Computer resources were provided by the the Research Computing Center at the University of Chicago and the Minnesota Supercomputing Institute at the University of Minnesota.

CHAPTER 5

THE LOCALIZED ACTIVE SPACE METHOD WITH UNITARY SELECTIVE COUPLED CLUSTER

This chapter is reprinted with permissions from *arXiv:2404.12927*, **2024**

Abstract

We introduce a hybrid quantum-classical algorithm, the localized active space unitary selective coupled cluster singles and doubles (LAS-USCCSD) method. Derived from the localized active space unitary coupled cluster (LAS-UCCSD) method, LAS-USCCSD first performs a classical LASSCF calculation, then selectively identifies the most important parameters (cluster amplitudes used to build the multireference UCC ansatz) for restoring inter-fragment interaction energy using this reduced set of parameters with the variational quantum eigensolver method. We benchmark LAS-USCCSD against LAS-UCCSD by calculating the total energies of $(H_2)_2$, $(H_2)_4$ and *trans*-butadiene, and the magnetic coupling constant for a bimetallic compound $[Cr_2(OH)_3(NH_3)_6]^{3+}$. For these systems, we find that LAS-USCCSD reduces the number of required parameters and thus the circuit depth by at least one order of magnitude, an aspect which is important for the practical implementation of multireference hybrid quantum-classical algorithms like LAS-UCCSD on near-term quantum computers.

5.1 Introduction

Accurately modeling strong electron correlation is crucial in quantum chemistry, especially for describing transition-metal and heavy-metal chemistry, magnetic molecules, bond breaking, biradicals, excited states, and the functionality of various materials. Despite its significance, addressing this challenge with computationally feasible electronic structure methods remains daunting. Strong electron correlation, also known as “static" or “non-dynamic"

correlation, emerges from degenerate or near-degenerate electronic states within systems referred to as multiconfigurational.[11] To investigate these systems effectively, multireference methods are indispensable, such as the complete active space self-consistent field (CASSCF) method[26–28] and multireference configuration interaction (MRCI)[29,30]. While these methods offer accuracy, their applicability is constrained by exponential and factorial scaling with the size of the "active space," determined by the number of electrons and orbitals subjected to exact diagonalization[12].

To enhance the practicality of multireference methods, approximate classical CI solvers like the density matrix renormalization group (DMRG)[217,218], selected configuration interaction methods[219–221], and quantum Monte Carlo methods [222–224] have been developed. These methods aim to reduce the exponential computational cost by eliminating less significant configurations. Another approach involves active space fragmentation techniques, such as active space decomposition (ASD)[73–76], cluster mean-field[77], rank-one basis states[78,79], TP-SCI algorithm[80], density matrix embedding theory (DMET)[96,97,99,100,104,106,108,109,225], restricted active space (RAS)[81,82], generalized active space (GAS)[83], and the localized active space self-consistent field method (LASSCF)[84,85], among others. LASSCF, in particular, models strong, localized correlation within specific fragments while modeling inter-fragment correlation using a mean-field approach. However, when inter-fragment electron correlation beyond the mean-field level becomes important, LASSCF becomes inaccurate, as demonstrated in the tris-(μ-hydroxo)-bridged chromium compound ($[Cr_2(OH)_3(NH_3)_6]^{3+}$), where LASSCF incorrectly suggests a high-spin sextet ground state instead of the actual low-spin singlet[226].

To restore the electron correlation between fragments, the localized active space state interaction (LASSI) method was developed[227], though it reintroduces the factorial scaling of CASSCF. Another standard approach that can be used to restore electron correlation between fragments is the unitary coupled cluster method (UCC)[228,229] for inter-fragment

excitations. However, when this method is applied to a LAS reference wave function, and in general any multireference wave function, it necessitates arbitrary truncation of the otherwise non-terminating equations of the cluster expansion for practical implementation on a classical computer. This has inspired the development of the LAS-UCC method where the UCC step can in principle be efficiently implemented on a quantum circuit simulator or quantum computer.[230].

There have been significant advancements in quantum computing hardware and algorithms, particularly in the field of quantum chemistry simulation[86,231–236]. This progress includes the development of various ansatzes such as the UCC ansatz[237–239], hardware efficient ansatzes,[240] adaptive structure anzatzes,[241] and qubit coupled-cluster ansatzes[242–244] for variational quantum eigensolver (VQE) simulations[245], which is currently the most practical hybrid quantum-classical method in quantum chemistry.

The LAS-UCCSD algorithm, while not yet run on actual quantum hardware, has been validated using quantum circuit simulators on a classical computer. It has been demonstrated that LAS-UCCSD achieves chemical accuracy (1 kcal/mol) in calculating total energies and an accuracy of 1 cm^{-1} in calculating magnetic coupling constants, relative to the corresponding CASCI values, for the limited systems explored[226,246]. However, a LAS-UCCSD calculation of moderately large systems such as the tris-(μ-hydroxo)-bridged chromium compound $[Cr_2(OH)_3(NH_3)_6]^{3+}$ with a mixed def2-TZVP/def2-SVP basis set requires 774 cluster amplitudes, and, therefore, several thousands of quantum gates. The unitary selective coupled cluster (USCC) method of Fedorov *et al.*[247] employs a selection scheme that includes only the most relevant excitations, using Hamiltonian matrix elements to identify the most connected excited state determinants to the single determinant ground state wave function. In this study, we generalize this approach to LAS-UCCSD. We utilize the Baker-Campbell-Hausdorff (BCH) expansion to re-express the USCC selection criterion in terms of LAS-UCCSD energy gradients. These analytical gradients are then used to select the most im-

portant cluster amplitudes in a new method that we call LAS-USCCSD. We demonstrate the advantage of LAS-USCCSD over LAS-UCCSD in terms of computational cost on several molecular systems.

It is important to also note some recent advancements in system-specific iterative ansatz design in quantum computing[241–243,248–253]. One of the leading algorithms in this domain is ADAPT-VQE[241], which iteratively builds an ansatz by adding fermionic operators, based on the expensive evaluation of energy gradients with respect to the variational parameters of these operators. ADAPT-VQE's method of selecting operators at each iteration is based on their impact on energy reduction, which leads to a more efficient ansatz generation compared to standard VQE. For a detailed comparison of the USCC ansatz and ADAPT-VQE ansatz, Fedorov et al.'s work[247] provides insightful analysis. Similar to the USCC method[247], the excitation selection criteria in LAS-USCCSD for reflect the 'importance' of an excitation but starting from a multireference wave function. While this may not yield the most compact ansatz like ADAPT-VQE, it has the benefit of not requiring additional measurements on the quantum computer for determining important coefficients/parameters, hence potentially being more cost-effective in terms of measurements on the quantum hardware. Unlike ADAPT-VQE, LAS-USCCSD is a single shot fixed-ansatz scheme *i.e.* it determines the optimal amplitudes as a form of classical pre-screening and does not require any VQE/QPE calculations on the quantum computer for determining important coefficients/parameter.

The paper is organized as follows. We first describe the LAS-UCCSD and USCC methods followed by our implementation of the LAS-USCCSD method. Next, we discuss numerical results obtained using LAS-USCCSD on four strongly correlated systems with important inter-fragment correlations. Finally, we provide an outlook of the method and discuss future possibilities.

5.2 Theory and Methods

5.2.1 Localized Active Space Unitary Coupled Cluster Method

In the LAS-UCCSD algorithm[226] the energy is obtained by first performing a LASSCF calculation followed by a VQE on the combined fragment space to restore inter-fragment electron correlation[226,246]. LAS-UCCSD has been validated using Qiskit's Aer state vector simulator[246,254] and is yet to be tested on quantum hardware. The LASSCF wave function[84,85] is an anti-symmetrized product of the K-fragment CAS wave functions and is represented as:

$$|\Psi_{\text{LAS}}\rangle = \bigwedge_K (\Psi_{A_K}) \wedge \Phi_D \tag{5.1}$$

where Ψ_{A_k} denotes the many-body wave function of the Kth localized subspace, and Φ_D denotes the single determinantal wave function delocalized over the system under consideration. Considering $\left|\Psi_{\text{QLAS}}\right\rangle = \bigwedge_K (\Psi_{A_K})$ as the active-space LASSCF wave function loaded onto a quantum device, the LAS-UCCSD wave function can be expressed as:

$$|\Psi_{\text{LAS-UCCSD}}(\boldsymbol{t})\rangle = \hat{U}_{\text{UCCSD}}(\boldsymbol{t})|\Psi_{\text{QLAS}}\rangle. \tag{5.2}$$

Here, the corresponding VQE on the loaded LASSCF wave function is done using a generalized form of the UCC singles and doubles (UCCSD) ansatz[237–239]:

$$\hat{U}_{\text{UCCSD}} = \exp\left\{t_l^k(\hat{a}_k^\dagger \hat{a}_l - \text{h.c.}) + \frac{1}{4} t_{ln}^{km}(\hat{a}_k^\dagger \hat{a}_m^\dagger \hat{a}_n \hat{a}_l - \text{h.c.})\right\}, \tag{5.3}$$

where t_l^k and t_{ln}^{km} are the cluster amplitudes for single and double excitations, respectively. $\hat{a}_k^\dagger$ and $\hat{a}_l$ are the creation and annihilation operators, acting on the molecular orbitals k and l respectively. "h.c." stands for the Hermitian conjugate of the preceding terms. In practice, the process requires decomposing the single exponential of a sum of generators into

a product of exponentials of individual generators. This can be done in a variety of ways, one of the most common of which is the Suzuki-Trotter decomposition[255,256] used here, to the first order. The fragment Hamiltonians are transformed to the qubit representation using a fermion-to-spin transformation, such as the Jordan-Wigner transformation[257]. The minimization of the total energy via VQE is performed by variation of the $\boldsymbol{t}$ with a classical computer and algorithm, with the energies being evaluated on a quantum simulator.

One of the challenges for the practical implementation of this method is the large number of UCCSD parameters ($\boldsymbol{t}$ amplitudes) required for the VQE energy optimization. For example, an energy LAS-UCCSD calculation for $[Cr_2(OH)_3(NH_3)_6]^{3+}$ requires 774 parameters - as can be calculated using equations 8 and 9 - and 2126 iterations. Each iteration refers to a numerical optimization step of $|\Psi_{\text{LAS-UCCSD}}(\boldsymbol{t})\rangle$ using the Broyden–Fletcher–Goldfarb–Shanno (BFGS) algorithm[258–261] or some other classical optimization algorithm. In a later section "Resource Estimates" we show that this translates to 36,360 CNOT gates and 54,612 single qubit gates, which is impractical with the current or near-term quantum computing capabilities even using a state-vector simulator. To address this, we have developed a physically motivated scheme that focuses on only the most relevant parameters.

5.2.2 Unitary Selective Coupled Cluster Method

The unitary selective coupled cluster (USCC) method of Fedorov *et al.*[247] starts from a Hartree-Fock reference wave function. In the initial step the most important amplitudes are selected based on the following criterion:

$$|H_{\beta\mathbf{0}}| = |\langle \Phi_\beta | \hat{H} | \Phi_\mathbf{0} \rangle| \geq \epsilon. \tag{5.4}$$

Here, $H_{\beta\mathbf{0}}$ represents the one- and two-body electronic Hamiltonian matrix element, connecting the determinant Φ_β to $\Phi_\mathbf{0}$, and ϵ is a user-defined cut-off. The amplitudes t_β

corresponding to these excitations are included in the UCCSD ansatz generation as required in equation 5.3.

5.2.3 Localized Active Space Unitary Selected Coupled Cluster Method

A direct translation of USCC to the LASSCF Hamiltonian has the following form

$$|H_{\mathrm{LAS}_{\beta\mathbf{0}}}| = |\left\langle \Psi_{\mathrm{LAS}_{\beta}} \right| \hat{H} \left| \Psi_{\mathrm{LAS}_{\mathbf{0}}} \right\rangle| \geq \epsilon. \tag{5.5}$$

Here, Ψ_{LAS_β} and $\Psi_{LAS_{\mathbf{0}}}$ are both multiconfigurational LASSCF wave functions, the former generated by the action of a particular coupled-cluster generator β on the latter. Unlike the single-reference case, these two states are not necessarily orthogonal[262] and their Hamiltonian matrix element (equation 5.5) is not reducible to a simple closed-form expression of a handful of 1- and 2-body Hamiltonian matrix elements.

To address this, we recontextualize the USCC selection criterion in terms of the energy gradients using the Baker-Campbell-Hausdorff (BCH) expansion with respect to the cluster amplitudes:

$$|H_{\beta\mathbf{0}}| = \left| \frac{\partial E_{\mathrm{UCC}}}{2\partial t_\beta} \right|_{\boldsymbol{t}=0} \geq \epsilon. \tag{5.6}$$

We have rewritten the Hamiltonian matrix elements in terms of the gradients of the UCC energy expression. Equation (5.6) can now be used to select the Hamiltonian matrix elements $H_{\beta\mathbf{0}}$ and therefore the corresponding t_β amplitudes (Derivation for equation (5.6) in section 1 of the Supplementary Information (SI) of reference 98). Now, we express the LAS Hamiltonian matrix elements of equation (5.5) in terms of energy gradients as in equation (5.6) and replace equation (5.5) with

$$\left| \frac{\partial E_{\text{LAS-UCCSD}}}{\partial t_\beta} \right|_{\boldsymbol{t}=0} \geq \epsilon. \tag{5.7}$$

The cluster amplitudes t_β for a given ϵ are now included in the UCC ansatz for the VQE step and we refer to this method as LAS-USCCSD.

The LAS-UCCSD gradients are evaluated before running any optimization steps, using only the information from the LASSCF wave function. The gradients are evaluated on a classical computer and selecting the most important parameters for VQE optimization is a form of classical preprocessing. We exclusively focus on direct initialization (DI), which has been shown to be more advantageous than using QPE to load the fragment wave functions for fragments requiring less than 20 qubits in terms of gate count and Trotter steps[246]. However, the insights derived here are applicable to all forms of state preparation. In both LAS-UCCSD and LAS-USCCSD, using DI, the CI vectors of the individual fragments are loaded onto the quantum circuit for each fragment using one and two-qubit gates, which has dimensions $N_{\text{frag,K}}$. Here $N_{\text{frag,K}}$ is the number of spin orbitals in the K^{th} fragment's active space. This approach entangles the fragment qubits during state preparation. The steps to perform a LAS-USCCSD calculation are summarized in Algorithm 1.

Algorithm 1 Localized Active Space Unitary Selective Coupled Cluster

1: Run a classical LASSCF calculation
2: Use $\left|\frac{\partial E_{\text{LAS-UCCSD}}}{\partial t_\beta}\right|_{\boldsymbol{t}=0} \geq \epsilon$ and a user-defined ϵ to generate the custom LAS-USCCSD ansatz with the most important parameters ($\boldsymbol{t}$ amplitudes)
3: Initialize the multiconfigurational LASSCF state either using localized QPE circuits or direct initialization (DI) and the LAS-USCCSD ansatz as in 2
4: Run VQE with the custom ansatz to compute energy
5: Lower the value of ϵ and repeat steps 1-3 to update amplitudes and check for energy convergence

Here we discuss how to calculate the total number of parameters (t_β amplitudes) for a given active space. This task is combinatorial and involves initially calculating the total possible number of singles and doubles amplitudes, followed by subtracting the number of possible

singles and doubles amplitudes within the fragment subspaces. This calculation depends on the number of spatial orbitals and the underlying fragmentation. Calculating the number of singles amplitudes is relatively straightforward, with an example provided later for H_2. The number of doubles amplitudes in a given active space can be found by using:

$$f(n) = 6\binom{\binom{n}{2}}{2} + 2(n+1)\binom{n}{2} \tag{5.8}$$

where n is the number of spatial orbitals (half the number of spin orbitals), $\binom{n}{2}$ is a combinatorial term representing the number of ways to choose 2 items from a set of n distinct items and $\binom{\binom{n}{2}}{2}$ refers to the number of unique pairs of unique pairs of a set of n distinct items. For a LAS-UCCSD calculation in which all excitations must involve at least two fragments, one can subtract the number for each fragment's "internal" excitations from the number for the whole system using:

$$f_{\text{LAS-UCCSD}}(n, n_K, n_L, \ldots, n_{N_{\text{frag}}}) = f(n) - \sum_{K}^{N_{\text{frag}}} f(n_K). \tag{5.9}$$

This is done because we focus only on inter-fragment excitations. Equations 5.8 and 5.9 can be used to find the total number of doubles amplitudes.

The USCC method also included disconnected triple and quadruple terms generated using the previously computed singles and doubles cluster amplitudes. In future work, where electron correlation beyond singles and doubles is necessary, we may consider including disconnected and connected triple and quadruple terms.

5.2.4 Computational Methods

All the LAS-UCCSD and LAS-USCCSD calculations in this work were performed using the LAS-USCC repository[263] which includes modified versions of the mrh code[215] and utilizes the electron integrals and quantum chemical solvers from PySCF (version 2.3).[122,123] The

current implementation for computing LAS-UCCSD gradients in Step 2 of algorithm 1 has exponential time and memory cost since it is designed to evaluate the gradient at any arbitrary vector of amplitudes $\boldsymbol{t}$. However, because LAS-USCC only requires the gradient evaluated at the origin, $\boldsymbol{t} = 0$, it is possible to implement a memory-efficient, polynomial-time algorithm for these gradients using the generalized Wick's theorem,[264] and this will be pursued in future work and is discussed further in Section S04 of the SI of reference 98. All noise-free simulations of state preparation using DI and measurement circuits were carried out using the Qiskit framework and the Aer state vector simulator[254]. The basis sets and active spaces, and localization used for the representative examples are described as the examples are introduced below.

5.3 Results and Discussion

Four distinct systems were considered, as illustrated in figure 5.1.

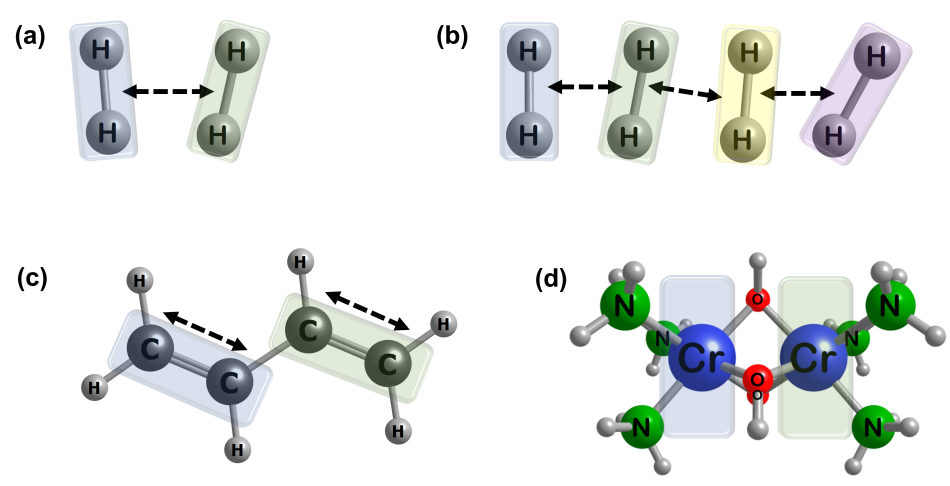

Figure 5.1: Systems studied in this work: (a) two interacting hydrogen molecules, (b) four interacting hydrogen molecules (c) the *trans*-butadiene molecule, and (c) tris-(μ-hydroxo)-bridged chromium molecule ($[Cr_2(OH)_3(NH_3)_6]^{3+}$) molecule. Arrows represent intermolecular and interatomic distances used to increase or decrease inter- and intra-fragment correlation for the hydrogen and *trans*-butadiene systems respectively.

These systems present a different degree of strength of inter-fragment correlation, for which

LASSCF shows significant deviations from the CASCI results and have been used as benchmark systems in references 226 and 246.

5.3.1 Hydrogen Molecules (H_4 and H_8)

The first system contains two H_2 molecules with the distance between the midpoints of the two H_2 fragments defining their interaction strength. We employed the STO-3G basis set and an active space of (2,2) for each fragment, corresponding to (4,4) in the CASCI calculations. The minimal STO-3G basis set was only used for the hydrogen systems for initial testing. Later, for the more realistic systems illustrated in Figure 5.1b-5.1d, more complete basis sets were employed. The interaction is weak when the two H_2 molecules are separated by more than 1.8 Å, and it becomes stronger as the two H_2 molecules get closer[226]. We first focus on the two H_2 molecules separated by 1.46 Å, where the total energy from LASSCF deviates from CASCI by 3.83 kcal/mol. We calculated the gradient values according to equation (5.7) and plotted the distribution of number of parameters against the gradient values as a histogram in figure 5.2a. Using equations 5.8 and 5.9 to obtain the number of doubles amplitudes, we obtain $f(4) = 150$ (the total number of spatial orbitals are 4), and $f(2) = 6$ (the fragments consist of 2 spatial orbitals each), from which $f_{\text{LAS-UCCSD}} = 138$. The number of singles amplitudes is 8 (since each electron has 2 choices), thereby leading to a total of 146 parameters ($\boldsymbol{t}$ amplitudes). The data in figure 5.2a shows that around 70% of the parameters have negligible gradient values, suggesting that they can be removed from the UCCSD ansatz. The dependence of the number of parameters on ϵ along with the total energies for this system is reported in table 5.1 as obtained using equation 5.7.

$\epsilon(E_h)$	Parameters	LAS-USCCSD Energy(E_h)
0.100000	0	-2.102636
0.062506	4	-2.103902
0.009541	14	-2.106346
0.007543	23	-2.107519
0.005964	26	-2.108738
0.004715	28	-2.108741
0.002947	32	-2.108741
0.001456	36	-2.108741
0.000910	38	-2.108741
0.000087	40	-2.108741
0.000000	146	-2.108741

Table 5.1: Dependence of the number of parameters on ϵ and the corresponding total energies for the H_4 system as is obtained using equation 5.7. The corresponding CASCI total energy is -2.108741 E_h.

In figure 5.2a, we plot the distribution of absolute gradient values which indicates that a large percentage of gradients are near-zero. In figure 5.2b, we plot the energy discrepancy, denoted as ΔE in kcal/mol, between the LAS-UCCSD and LAS-USCCSD methods. Both here and in table 5.1, we note that LAS-USCCSD achieves convergence to within 1 kcal/mol of the reference LAS-UCCSD energy with only 23 out of 146 parameters or 16% of the parameter space.

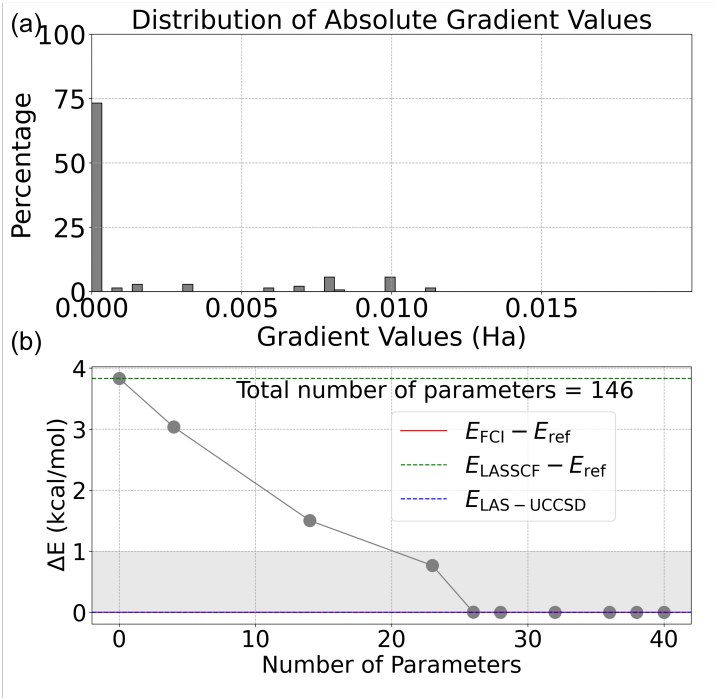

Figure 5.2: (a) Histogram displaying the percentage distribution of absolute gradient values (in E_h) for the H_4 molecule at an inter-fragment distance of 1.46 Å. (b) The energy convergence plot ($\Delta E = E_{\text{LAS-USCCSD}} - E_{\text{LAS-UCCSD}}$) for the LAS-USCCSD method as a function of the number of parameters, benchmarked against the LAS-UCCSD reference energy, showing the changes in calculated energy relative to the number of parameters included in LAS-USCCSD. The total number of parameters for the corresponding LAS-UCCSD calculation is 146. The shaded area highlights the region within 1 kcal/mol of the reference values.

For further insight, we also considered other distances between the two H_2 molecules and plot the energy convergence with respect to the CASCI limit in figure 5.3. We observe that when the two H_2 molecules are separated by 0.96 Å, LASSCF diverges from LAS-UCCSD by more than 75 kcal/mol. This is because the distance between the two hydrogen atoms of a single H_2 unit is 1 Å and this geometry is close to the equidistant square geometry. The discrepancy between LASSCF and LAS-UCCSD diminishes when the hydrogen moieties are brought even closer together (for example, when the intermolecular distance is 0.75 Å) as the covalent bonds within each nominal H_2 molecule are broken and replaced with covalent bonds between the two nominal molecules, as described by the optimized LASSCF molecular

orbitals, shown in figure S2 of the SI of reference 98. However, LAS-USCCSD with 28 parameters (an estimated 928 CNOT gates) out of 146 (6656 CNOT gates) restores back most of the electron correlation energy and is within 1 kcal/mol accuracy. The same behavior occurs for all the bond lengths studied. As was discussed in Otten *et al.*[226], LASSCF itself is enough to approximate the CASCI limit for inter-fragment distances greater than 2.00 Å.

Next, we study a system formed of four H_2 molecules using a minimal STO-3G basis set for further testing in line with the previous example, with the distance between the midpoints of the two nearest neighbor fragments defining their interaction strength. We examine a geometry where the inter-fragment distance is 1.46 Å, a distance at which the H_2 molecules are relatively close to one another, resulting in strong inter-fragment correlation. Under these conditions, LASSCF alone is insufficient to achieve chemical accuracy in calculating the total energies with respect to the corresponding CASCI. Similar to H_4, in configurations where the four H_2 molecules are farther apart, the LASSCF description suffices to reach chemical accuracy. We employed an active space of (2,2) for each fragment, corresponding to (8,8) in the CASCI calculations. Here, LAS-UCCSD corresponds to 2796 parameters (equation (5.9) can be used to get this number) to be optimized. We observe in figure 5.4a that for inter-fragment distances of 1.46 Å, around 80% of the gradients are near zero, thereby suggesting that less than 20% parameters are required for convergence. LASSCF diverges from LAS-UCCSD by almost 15 kcal/mol, whereas LAS-UCCSD using 398/2796 parameters (∼15% parameter space) *i.e.* an estimated 27416/198336 CNOT gates, reaches chemical accuracy compared with LAS-UCCSD.

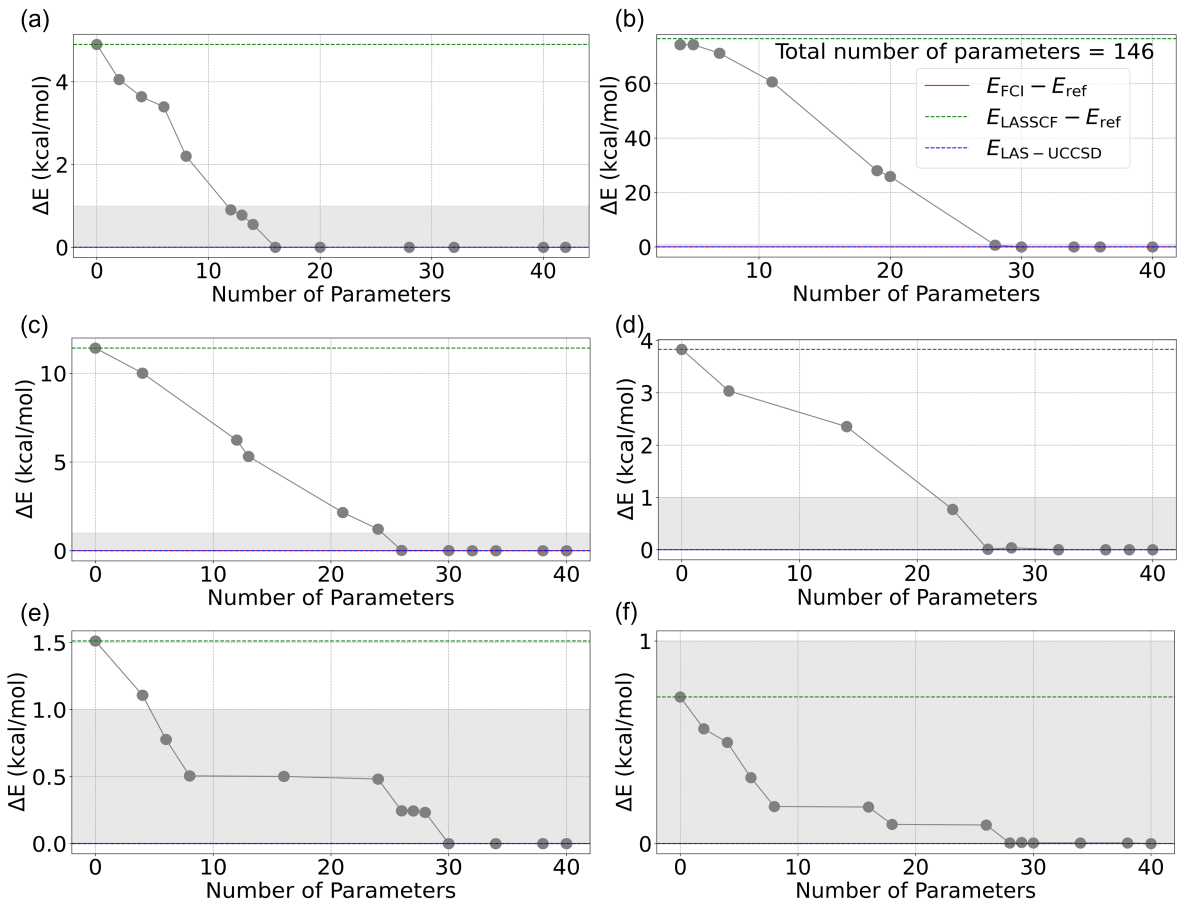

Figure 5.3: Energy convergence ($\Delta E = E_{\text{LAS-USCCSD}} - E_{\text{LAS-UCCSD}}$) for the H_4 molecule as a function of the number of parameters at varying inter-fragment distances. From top left to bottom right, the plots correspond to inter-fragment distances of (a) 0.75 Å, (b) 0.96 Å, (c) 1.20 Å, (d) 1.46 Å, (e) 1.75 Å, and (f) 2.00 Å. Each plot benchmarks the LAS-USCCSD energy against the LAS-UCCSD reference, illustrating how the energy difference decreases with an increasing number of parameters. The total number of parameters for all the corresponding LAS-UCCSD calculations is 146. The shaded area highlights the region within 1 kcal/mol of the reference values.

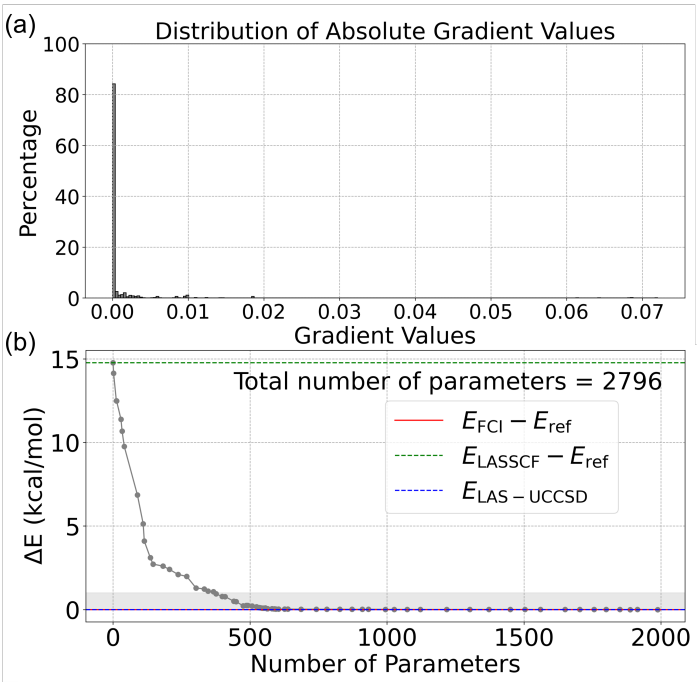

Figure 5.4: (a) Histogram showing the percentage distribution of absolute gradient values (in E_h) for the H_8 molecule at an inter-fragment distance of 1.46 Å. (b) Energy convergence plot ($\Delta E = E_{\text{LAS-USCCSD}} - E_{\text{LAS-UCCSD}}$) for H_8, detailing the reduction in the calculated energy relative to the increasing number of parameters. The total number of parameters for the corresponding LAS-UCCSD calculation is 2796. The shaded area highlights the region of chemical accuracy defined as being within 1 kcal/mol of the reference values.

5.3.2 Trans-butadiene

We investigated *trans*-butadiene using the 6-31G basis. It consists of two strongly interacting C-C double-bond fragments. At the equilibrium geometry (henceforth referred to as geometry 1) there is no significant inter-fragment electron correlation and the LASSCF energy is only 2.36 kcal/mol higher than the corresponding reference CASCI total energy. Figure 5.5 shows that 90% of the parameters can be removed for geometry 1 and in figure 5.5a we find that using only 84/2504 parameters (3856/118784 CNOT gates) we get to within chemical accuracy of the reference. The total number of parameters can be calculated using equations 5.8 and 5.9 and the number of parameters required to achieve chemical accuracy can be achieved using equation 5.7 and $\epsilon = 4.14 * 10^{-3}$. The dependence of the number of

parameters on ϵ are further reported in Table S5 of the SI of reference 98. The CNOT gate estimates are discussed in the section “Resource Estimates".

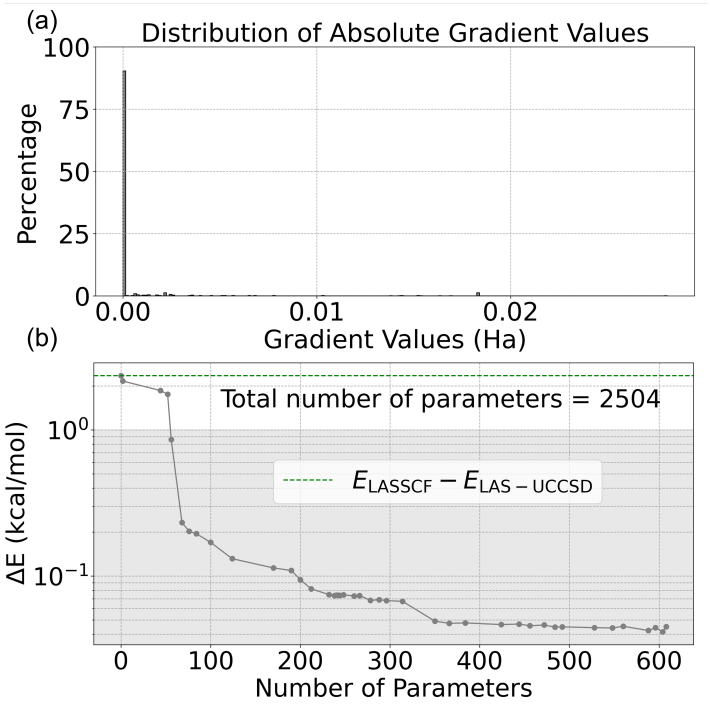

Figure 5.5: (a) Distribution of absolute gradient values (in E_h) for geometry 1 of *trans*-butadiene, showing the percentage of gradients within specified value ranges. (b) LAS-USCCSD energy convergence logarithmic plot ($\Delta E = E_{\text{LAS-USCCSD}} - E_{\text{LAS-UCCSD}}$) for stretched *trans*-butadiene as a function of the number of parameters. The convergence is benchmarked against the LAS-UCCSD reference energy which has a total of 2504 parameters. The shaded area highlights the region within 1 kcal/mol of the reference values.

Let us now consider “geometry 2" where the C-C double bonds are elongated by 3 Å from the equilibrium bond length of 1.33 Å while keeping the C-C single bond length fixed, thereby leading to a C-C double bond length of 4.33 Å (figure 5.1c). Figure 5.6a shows that 90% of the parameters have zero gradient value, implying that 288/2504 parameters are enough to achieve chemical accuracy, (figure 5.6b). Of note is that the gradients for geometry 2 (figure 5.6a) span up to an absolute value of 0.1 E_h whereas the gradients for the equilibrium geometry span only up to 0.02 E_h (figure 5.5a). For the particular case of geometry 2, the LAS-USCCSD with zero parameter energy is different from the LASSCF energy since

LAS-USCCSD (0 parameters) gets initialized at a different local minimum and is therefore different from the LASSCF ground state.

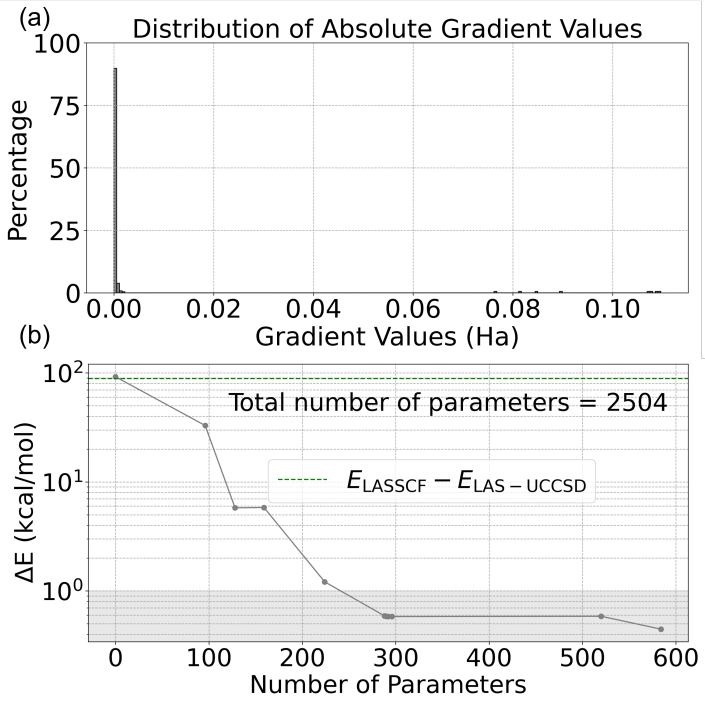

Figure 5.6: (a) Distribution of absolute gradient values (in E_h) for geometry 2 of *trans*-butadiene, showing the percentage of gradients within specified value ranges. (b) LAS-USCCSD energy convergence plot ($\Delta E = E_{\text{LAS-USCCSD}} - E_{\text{LAS-UCCSD}}$) for *trans*-butadiene geometry 2 as a function of the number of parameters. The convergence is benchmarked against the LAS-UCCSD reference energy which has a total of 2504 parameters. The shaded area highlights the region of chemical accuracy defined as being within 1 kcal/mol of the reference values.

5.3.3 Tris-(μ-hydroxo)-bridged Chromium Compound

Finally, we compute the magnetic coupling constant (J-coupling parameter) for the bimetallic compound $[Cr_2(OH)_3(NH_3)_6]^{3+}$, (figure 5.1d) with LAS-USCCSD. The J value can be calculated using the Yamaguchi formula[265] as the difference between the high-spin (HS) and low-spin (LS) energies divided by the difference between the $\left\langle \hat{S}^2 \right\rangle$ (expectation value of the

$\hat{S}^2$ spin operator) values of the HS and LS states.

$$J_{ab} = \frac{E_{\mathrm{HS}} - E_{\mathrm{LS}}}{\left\langle \hat{S}^2 \right\rangle_{\mathrm{LS}} - \left\langle \hat{S}^2 \right\rangle_{\mathrm{HS}}} \tag{5.10}$$

A negative J-coupling indicates antiferromagnetic coupling, whereas a positive J-coupling indicates ferromagnetic coupling. Otten et al.[226] showed that LAS-UCCSD using a minimal active space of 6 electrons in 6 singly-occupied 3d orbitals, 3 for each Cr ion, predicts a J value of -11.6 cm^{-1} in agreement with the corresponding CASCI value of -11.6 cm^{-1}. The def2-SVP basis was used for the C, N, O, and H atoms, while the def2-TZVP basis[266] was used for the Cr atoms. A LAS-UCCSD calculation requires 774 parameters (($\boldsymbol{t}$ amplitudes) and 2126 UCC iterations for convergence as also reported in figure 5.7 and Table 5.2. However, 90% of the amplitudes have near-zero gradients as shown in figure 5.7a. LAS-USCCSD with only 12/774 parameters and 18 iterations predicts the correct sign for the J-coupling constant and the correct low-spin ground state. LAS-USCCSD with only 10% of the parameters is within 1 cm^{-1} of the desired CASCI J-coupling value. On a state vector simulator[254] with 12 qubits and first-order Trotterization, this calculation using direct initialization did not converge with our current computing resources. The LAS-UCCSD was run for 240 hours on a 256 Gb of memory on an AMD EPYC-7702 128-core processor with the VQE step reaching only the forty-sixth iteration with the first iteration taking up more than 28 hours. Using 12 parameters (488 CNOT gates), LAS-USCCSD converged within 73 seconds and using 77 parameters (3256 CNOT gates) it required less than 5 hours of computing time. For LAS-USCCSD using 12 parameters, the first VQE iterations take around 15 seconds and for 77 parameters, the first VQE iteration takes 7 minutes. Using the quantum circuit simulator with DI, LAS-USCCSD with 12 UCC parameters predicts the right ground state and LAS-USCCSD with 77 UCC parameters is within 1 cm^{-1} of the desired CASCI J-coupling value.

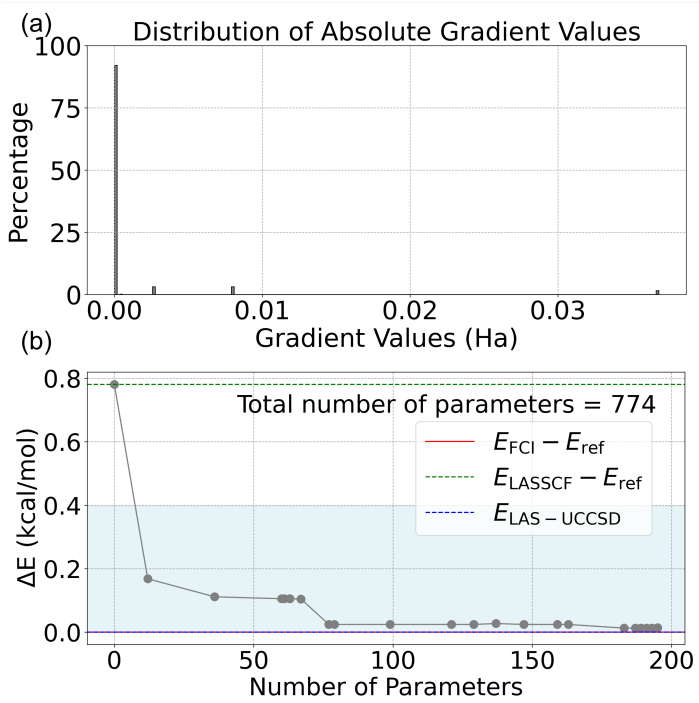

Figure 5.7: (a) The distribution of absolute gradient values (in E_h) for the chromium dimer system, indicating the percentage of total gradients within specific value ranges. (b) The convergence of energy ($\Delta E = E_{\text{LAS-USCCSD}} - E_{\text{LAS-UCCSD}}$) as a function of the number of parameters employed in the calculations, with the total number of parameters for LAS-UCCSD being 774. The reference energy is taken from the LAS-UCCSD method, and the graph shows how the energy difference decreases with an increasing number of parameters used. The shaded area in blue highlights the region of where the correct ground state is predicted and the low-spin state is lower than the high-spin state

Table 5.2: Comparison of (J) values for the $[Cr_2(OH)_3(NH_3)_6]^{3+}$ across various computational methods used on a classical emulator, focusing on parameter counts and iteration numbers for convergence. The high spin is single configurational and therefore is the same as -2649.1455510 E_h for all methods.

Method	**Parameters**	**Iterations**	**Low Spin Energy**	**J (cm^{-1})**
CASSCF	-	-	-2649.1463079	-13.8
LASSCF	-	-	-2649.1449395	11.2
CASCI@LAS orbitals	-	-	-2649.1461837	-11.6
LAS-UCCSD	774	2126	-2649.1461837	-11.6
LAS-USCCSD	12	18	-2649.1459158	-6.7
LAS-USCCSD	36	28	-2649.1460061	-8.3
LAS-USCCSD	77	169	-2649.1461448	-10.9
LAS-USCCSD	187	1980	-2649.1461634	-11.2

Table 5.3: Comparison of (J) values for the $[Cr_2(OH)_3(NH_3)_6]^{3+}$ across various computational methods used on the state vector simulator, focusing on VQE time required for convergence. The high spin is single configurational and therefore is the same as -2649.1455510 E_h for all methods.

Method	**Parameters**	**VQE Time**	**Low Spin Energy**	**J (cm^{-1})**
CASSCF	-	-	-2649.1463079	-13.8
LASSCF	-	-	-2649.1449395	11.2
CASCI@LAS orbitals	-	-	-2649.1461837	-11.6
LAS-UCCSD	774	240**	NA**	NA
LAS-USCCSD	12	0.02	-2649.1459158	-6.7
LAS-USCCSD	77	4.43	-2649.1461428	-10.8

** These calculations have not converged.

5.4 Resource Estimates

The number of single qubit gates (N_{SQGs}) and CNOT gates (N_{CNOTs}) calculated using the analytical formulas provided in reference 267 for standard qubit gate counts are provided in table 5.4. These can be written as:

$$N_{SQGs} = (4n + 1)2^{2n-1} \tag{5.11a}$$

$$N_{CNOTs} = (2n - 1)2^{2n} \tag{5.11b}$$

As evidenced by the reduction in the number of parameters ($\boldsymbol{t}$ amplitudes), we also observe a dramatic reduction in the corresponding single qubit and CNOT gate counts. Less than 15% of the total number of gates required in LAS-UCCSD are sufficient to obtain total energies within chemical accuracy of the corresponding CASCI value. For the $[Cr_2(OH)_3(NH_3)_6]^{3+}$ compound only 1.34% of CNOT gates are required to predict the correct ground state and about 9% of CNOT gates are important to predict the (J) values within 1 cm^{-1} accuracy of the corresponding CASCI value.

Table 5.4: Single qubit Gates (SQGs) and CNOT gates for LASUCCSD and LASUSCC for each system studied. The final column indicates the percentage of CNOT gates required by LASUSCCSD in comparison to their LASUCCSD counterparts.

System	Method	Parameters	N_{SQGs}	N_{CNOTs}	% N_{CNOTs}
H_4	LASUCCSD	146	10016	6656	-
H_4	LASUSCCSD	23	1408	928	13.94
H_8	LASUCCSD	2796	198336	132096	-
H_8	LASUSCCSD	398	27416	18224	13.80
C_4H_6 geometry 1	LASUCCSD	2504	178304	118784	-
C_4H_6 geometry 1	LASUSCCSD	84	5800	3856	3.46
C_4H_6 geometry 2	LASUCCSD	2504	178304	118784	-
C_4H_6 geometry 2	LASUSCCSD	288	19744	13120	11.05
$[Cr_2(OH)_2(NH_3)_6]^{3+}$	LASUCCSD	774	54612	36360	-
$[Cr_2(OH)_2(NH_3)_6]^{3+}$	LASUSCCSD	12	740	488	1.34
$[Cr_2(OH)_2(NH_3)_6]^{3+}$	LASUSCCSD	77	4924	3256	8.95

5.5 Summary and Future Directions

We have introduced an efficient implementation of a multireference quantum algorithm called localized active space unitary selective coupled cluster (LAS-USCCSD). It is derived from the parent classical LAS-UCCSD method. This algorithm considers only the most important parameters required to optimize a multireference wave function on a quantum circuit simulator, and although only validated on classical computers using the Qiskit statevector simulator, it is designed with early fault-tolerant quantum devices. We have tested the method on systems ranging from H_4, H_8 with minimal basis sets to a bimetallic chromium dimer compound using a mixture of more complete def2-TZVP/def2-SVP basis sets. Our findings show an improvement in algorithm efficiency and faster processing times for LAS-

USCCSD with respect to LAS-UCCSD, with a reduction of approximately 85% to 90% in the number of CNOT gates required to predict total energies in selected benchmark systems within chemical accuracy. Additionally, we observed a reduction of around 90% in the number of parameters and CNOT gates for predicting the magnetic coupling constant in a bimetallic compound, $[Cr_2(OH)_3(NH_3)_6]^{3+}$ within 1 cm^{-1} of the corresponding CASCI value. A future direction is to utilize generalized Wick's theorem for multireference wave functions to develop a polynomial-time algorithm for LAS-UCCSD gradient computation to increase memory efficiency for enhanced scalability. Furthermore, utilizing preselected LAS-USCCSD parameters in conjunction with adaptive and hardware-efficient quantum computing ansätze, such as ADAPT-VQE and nu-VQE, alongside efforts aimed at reducing CNOT gate counts[267,268] will lead to a further reduction in gate counts and circuit depth while maintaining accuracy. LAS-USCCSD will complement these methods for inherently multireference systems, potentially leading to more effective quantum simulations of realistic chemical systems and enabling the modeling of larger active spaces in the near future. Additionally, benchmarking the performance of ADAPT-VQE against both USCC and LAS-USCCSD approaches for inherently single and multi-configurational systems respectively is important and will be done in the future. Right now, classical calculations are still far superior, but with advancements in both quantum hardware and software, quantum computers may eventually overcome existing classical bottlenecks in quantum chemistry.

Acknowledgement

We thank Kanav Setia and Kenny Heitritter for their insightful discussion. This material is based upon work supported by the U.S. Department of Energy, Office of Science, National Quantum Information Science Research Centers. We gratefully acknowledge support from the NSF QuBBE Quantum Leap Challenge Institute (NSF OMA-2121044). Computer resources were provided by the Research Computing Center at the University of Chicago.

Y.A. and S.G. acknowledge support from the U.S. Department of Energy, Office of Science, under contract DE-AC02-06CH11357 at Argonne National Laboratory. Part of the work is supported by Wellcome Leap as part of the Quantum for Bio Program. Part of this work was also supported by Laboratory Directed Research and Development (LDRD) funding from Argonne National Laboratory, provided by the Director, Office of Science, of the U.S. DOE under Contract no. DE-AC02-06CH11357. Work performed at the Center for Nanoscale Materials, a U.S. Department of Energy Office of Science User Facility, was supported by the U.S. DOE, Office of Basic Energy Sciences, under Contract No. DE-AC02-06CH11357.

CHAPTER 6

METAL-METAL BONDING IN ACTINIDE DIMERS: U_2 AND U_2^-

This chapter is reprinted with permissions from *J. Am. Chem. Soc.* **2021**, *143*, 41, 17023–17028

ABSTRACT:

Understanding direct metal-metal bonding between actinide atoms has been an elusive goal in chemistry for years. We report for the first time the anion photoelectron spectrum of U_2^-. The threshold of the lowest electron binding energy (EBE) spectral band occurs at 1.0 eV, this corresponding to the electron affinity (EA) of U_2, whereas the vertical detachment energy (VDE) of U_2^- is found at EBE 1.2 eV. Electronic structure calculations on U_2 and U_2^- were carried out with state-of-the-art theoretical methods. The computed values of EA(U_2) and EA(U) and the difference between the computed dissociation energies of U_2 and U_2^- are found to be internally consistent and consistent with experiment. Analysis of the bonds in U_2 and U_2^- shows that while U_2 has a formal quintuple bond, U_2^- has a quadruple bond, even if the effective bond orders differ only by 0.5 unit instead of one unit. The resulting experimental-computational synergy elucidates the nature of metal-metal bonding in U_2 and U_2^-.

6.1 Introduction

Actinide-actinide bonds are of fundamental interest in chemistry, with their bare metal dimers providing the simplest examples. Given the importance of uranium, there is significant interest in the uranium dimer, U_2. As a metal-to-metal molecular prototype, the uranium dimer exhibits purely covalent bonding, this being unusual among uranium-containing

molecules. Moreover, as is often the case for actinides, the uranium dimer's electronic structure is exquisitely complex, prompting numerous theoretical studies[87–94].

Over the past 15 years, debate has focused on the bonding scheme within the uranium dimer, U_2. Initially, as determined by Gagliardi and Roos, the ground state U_2 was believed to have a quintuple bond, based on scalar complete active space self-consistent field (CASSCF) calculations, followed by perturbation theory (CASPT2), in which spin-orbit coupling was included a posteriori[87]. Their calculations revealed the following bonds between the two uranium atoms: three two-electron two-center bonds, i.e., one σ_g and two π_u from the 7s and 6d electrons, and four one-electron two-center bonds, i.e., one σ_g, one π_u, and two δg from 6d and 5f contributions, as well as two 5f electrons residing in non-bonding orbitals on each U atom1. This formally corresponds to a quintuple bond. Fourteen years later, Knecht, Jensen, and Saue[88] re-evaluated the bonding in U_2, finding its ground state to exhibit a quadrupole bond rather than the quintuple bond proposed by Gagliardi and Roos[87]. The Knecht et al work was based on multi-configurational CASSCF calculations using the same active space as in the calculation by Gagliardi and Roos[87], but including variational spin-orbit coupling[88,269]. Moreover, they also concluded that the previously calculated quintuple ground state is instead a low-lying electronically excited state[88]. The electronic ground state was shown to consist of three electron-pair bonds, i.e., one σ and two π, two one-electron bonds of σ and δ types, and four coupled 5f electrons localized on each U atom[88]. Without experimental validation, the debate remained ongoing.

In view of the above, we aim to resolve the long-debated bonding scheme in U_2 using the synergy between negative ion photoelectron spectroscopy and state-of-the-art quantum chemical calculations. We report joint experimental and theoretical investigations of the U_2^- anion. Together, these reveal the electronic structure and chemical bonding scheme of neutral U_2, this being facilitated by the photodetachment of the excess electron in the U_2^- anion to yield the ground and various electronic states of the neutral U_2 molecule. Thus, while the

experiments are conducted on U_2^-, i.e., on the anion, the results largely pertain to the electronic states of U_2, i.e., the anions' neutral counterpart. The resulting anion photoelectron spectrum of U_2^-, reported here for the first time, provides the experimental benchmark upon which high-level electronic structure calculations are validated. Together, this combined experimental and theoretical study elucidates the nature of chemical bonding in U_2 and U_2^-.

6.2 Methods

Experimental Methods. Anion photoelectron spectroscopy is conducted by crossing a beam of mass–selected negative ions with a fixed–frequency photon beam and energy–analyzing the resultant photodetached electrons. The photodetachment process is governed by the energy–conserving relationship: $h\nu$ = EBE + EKE, where $h\nu$ is the photon energy, EBE is the electron binding (photodetachment transition) energy, and EKE is the electron kinetic energy. Our apparatus consists of a laser vaporization cluster anion source, a time–of–flight mass spectrometer, a Nd:YAG photodetachment laser, and a magnetic bottle electron energy analyzer[270]. The magnetic bottle photoelectron spectrometer resolution is 35 meV at EKE = 1 eV. In this study, the third (355 nm, 3.49 eV) harmonic output of a Nd:YAG laser was used to photodetach electrons from mass–selected uranium cluster anions, U_n^- (n = 2–8). The well–known atomic transitions of Cu– were used to calibrate the magnetic bottle spectra[270].

The uranium dimer anions were generated in a laser vaporization ion source. Figure 6.1 presents a schematic of this source. Briefly, a housed, rotating and translating uranium rod was ablated using the second harmonic (532 nm, 2.66 eV) of a Nd:YAG laser, while 60 psig of argon gas was pulsed over the rod. A second pulsed valve, backed with 100 psig of helium gas, introduced the anions to the TOF-MS, from which the anions were mass-gated before their electrons were photodetached and energy-analyzed.

Additional uranium cluster anions, U_n^- (n = 3 – 8), were created in a more traditional laser

vaporization source. The second harmonic photon pulses ablated the rotating, translating uranium rod and directly introduced the ions into the TOF-MS, prior to the ions being mass-gated and their electrons energy-analyzed. The anion photoelectron spectra of U_n^- (n = 3 – 8) are presented in Fig. S1.

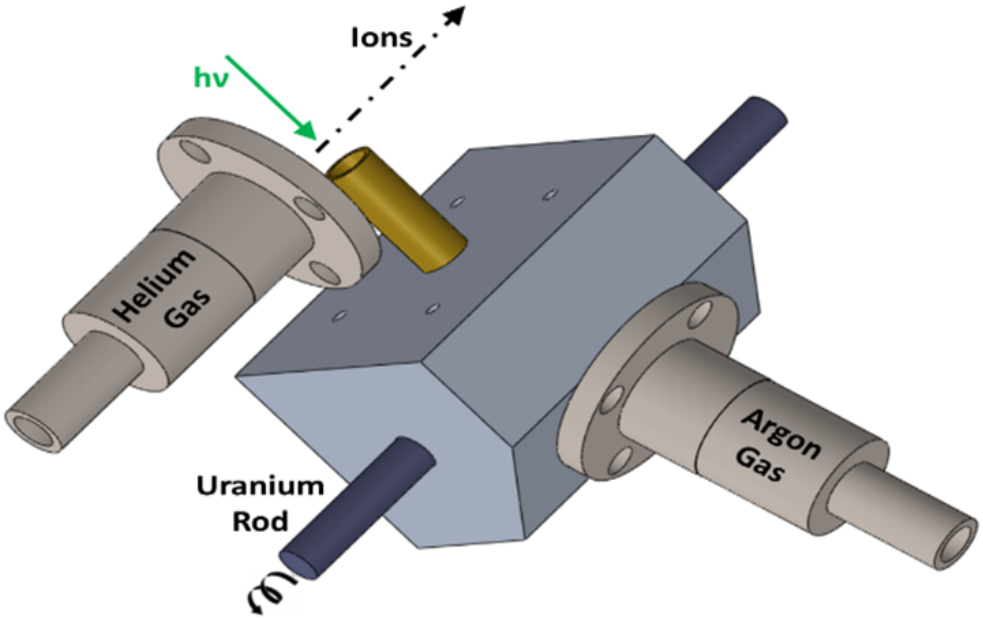

Figure 6.1: Schematic of the two-stage laser vaporization source used to generate the U_2^-

6.3 Theoretical Methods

Single point energy calculations were performed using the complete active space self-consistent field (CASSCF) method[271] for both U_2 and U_2^- at bond distances near their equilibrium geometry. The active space employed consists of 6 and 7 valence electrons for U_2 and U_2^-, respectively in 21 orbitals. Dynamical correlation effects were incorporated using the complete active space second order perturbation theory (CASPT2) on top of the CASSCF wave functions. The energies for excited electronic states were calculated at the multistate complete active space second order perturbation theory (MS-CASPT2) level of theory[272,273]. The OpenMolcas software package[274] was used to perform all the calculations. Scalar relativis-

tic effects were incorporated by using the Douglas Kroll-Hess (DKH) Hamiltonian[275–277]. The spin-orbit coupling effects were incorporated by using the SO-RASSI module[278] available in OpenMolcas. Atomic natural orbital type basis set[279] were used. A primitive set 26s23p17d13f5g3h was contracted to 9s8p6d4f2g. In order to maintain a linear geometry, a D_{2h} symmetry and the keyword "Linear" was used to impose super-symmetry. In total, 240 octet states lying up to 0.56 eV above the ground state, 80 sextet states lying up to 0.62 eV above the ground state, 30 quartet states lying up to 0.81 eV above the ground state and 10 doublet states lying up to 0.85 eV above the ground state were allowed to interact using the spin-orbit coupling Hamiltonian. In order to find the electronic ground state, the electronic energies for some points near the equilibrium geometry of U_2^- for the resulting 2540 spin-orbit coupled states were calculated and compared. In order to calculate the dissociation energies, the absolute energies for the U and U- atoms are calculated at the CASSCF level of theory by averaging over seventeen and thirty-eight states respectively. As was done for the dimers, dynamical correlation effects for the atoms are similarly incorporated using MS-CASPT2. For the atoms, a D_2 symmetry was considered and the keyword "Atom" was used to impose super-symmetry. Active spaces of 6 and 7 valence electrons in 16 orbitals were employed for U and U-, respectively. The sixteen orbitals considered here correspond to one 7s, three 7p, five 6d and seven 5f orbitals. In total, for the U- atomic specie, 152 octet states lying up to 2.02 eV above the ground state, 152 sextet states lying up to 0.85 eV above the ground state and 152 quartet states lying up to 1.16 eV above the ground state were allowed to interact using the spin-orbit coupling Hamiltonian. For the U atom, 68 septet states lying up to 1.44 eV above the ground state, 68 pentet states lying up to 0.82 eV above the ground state and 68 triplet states lying up to 1.05 eV above the ground state were allowed to interact using the spin-orbit coupling Hamiltonian. The energies of the atomic species were used to calculate the absolute energy of the U_2 and U_2^- at infinite bond distances. An imaginary shift of 0.2 and the default ionization potential electron affinity (IPEA)[280] of 0.25 was employed. The

IPEA is an empirical correction applied to the zero-order Hamiltonian.

6.4 Results and Discussion

6.4.1 Experimental Results

. Atomic uranium cations, U^+, have long been observed in mass spectra along with various uranium oxide and hydride cationic stoichiometries[281–283]. To prepare the gas-phase uranium dimer anion, U_2^-, we initially employed a conventional (one stage) laser-vaporization source, in which a pulsed laser beam ablated a depleted uranium rod to generate a plasma, which was propelled forward by a jet of supersonically-expanding helium gas. While this method made copious intensities of $U_mO_n^-$ cluster anions for m $\geq$ 2 and weaker signals of Um- cluster anions for m $\geq$ 3, U_2^- was essentially absent (see Fig. 2A). The likely culprit was the oxidized surface of the uranium rod, which provided oxygen to the plasma during laser-vaporization, in turn reacting with the Um- cluster anions to form UmOn- cluster anions. Because bare metal clusters readily react to form metal oxide cluster anions, the latter's signals prevailed in the mass spectrum, reducing the formation of U_m^- and especially of U_2^-. To suppress the effects of oxygen, we then used a two-stage (compound) laser vaporization source[284], in which two pulsed beams are crossed (see Fig. 1). The beam formed by laser vaporization of the uranium rod is perpendicular to the other beam's path which itself continues on into the main apparatus and into the anion extraction region of the time-of-flight mass analyzer/selector. The plasma formed during laser vaporization of the uranium rod is propelled by pulses of argon gas to reduce the velocities of the constituent species in that beam. The other beam is a pulsed helium jet.

The large mass differences between uranium clusters and oxidized uranium clusters caused them to travel at different speeds coming out of the laser vaporization source. By controlling the timing of the second (helium) pulsed valve, different species ions were preferentially

entrained by the helium expansion, where collisional cooling and dimer anion formation was promoted. Figure 6.2B shows a typical mass spectrum obtained by using this two-stage source. The uranium dimer anion, U_2^- is observed at a significant intensity, while the formation of uranium oxide anions is significantly reduced.

Figure 6.3 presents the negative ion photoelectron spectrum of U_2^- recorded with 3.49 eV (355 nm) photons using a magnetic bottle electron energy analyzer. The lowest electron binding energy (EBE) band in the spectrum exhibits a sharp threshold at 1.0 eV and an in-tensity maximum between EBE = 1.1 and 1.3 eV. When there is sufficient Franck–Condon overlap between the ground state of the anion and the ground state of the neutral species, and when there is negligible hot band (vibrationally-excited anion) signal, the threshold of the first EBE band signifies the electron affinity (EA) - determining transition. The vertical detach-ment energy (VDE) is the photodetachment transition energy at which the Franck–Condon overlap between the electronic ground-state wave functions of the anion and its neutral counterpart is maximal, here corresponding to EBE 1.2 eV. Thus, the EA value for neutral U_2 is revealed to be 1.0 eV, while the VDE value of the U_2^- anion is found to be 1.2 eV. A weak signal observed at EBE 0.4 eV is likely due to the subsequent photodetachment of U^-, itself generated by the photodissociation of U_2^-, as this value was observed in our previous study of the atomic uranium anion[285]. Features present at higher EBE values correspond to photode-tachment transitions to the excited vibrational and electronic states of neutral U_2. The spectral pattern observed in Fig. 3 suggests the presence of numerous underlying unresolved transitions.

6.4.2 Theoretical Results

. The experimentally-determined adiabatic electron affinity (EA) of the uranium dimer is compared to the theoretically-computed value obtained from state-of-the art electronic structure theory calculations on U_2 and U_2^-. Multi-reference wave function calculations of the

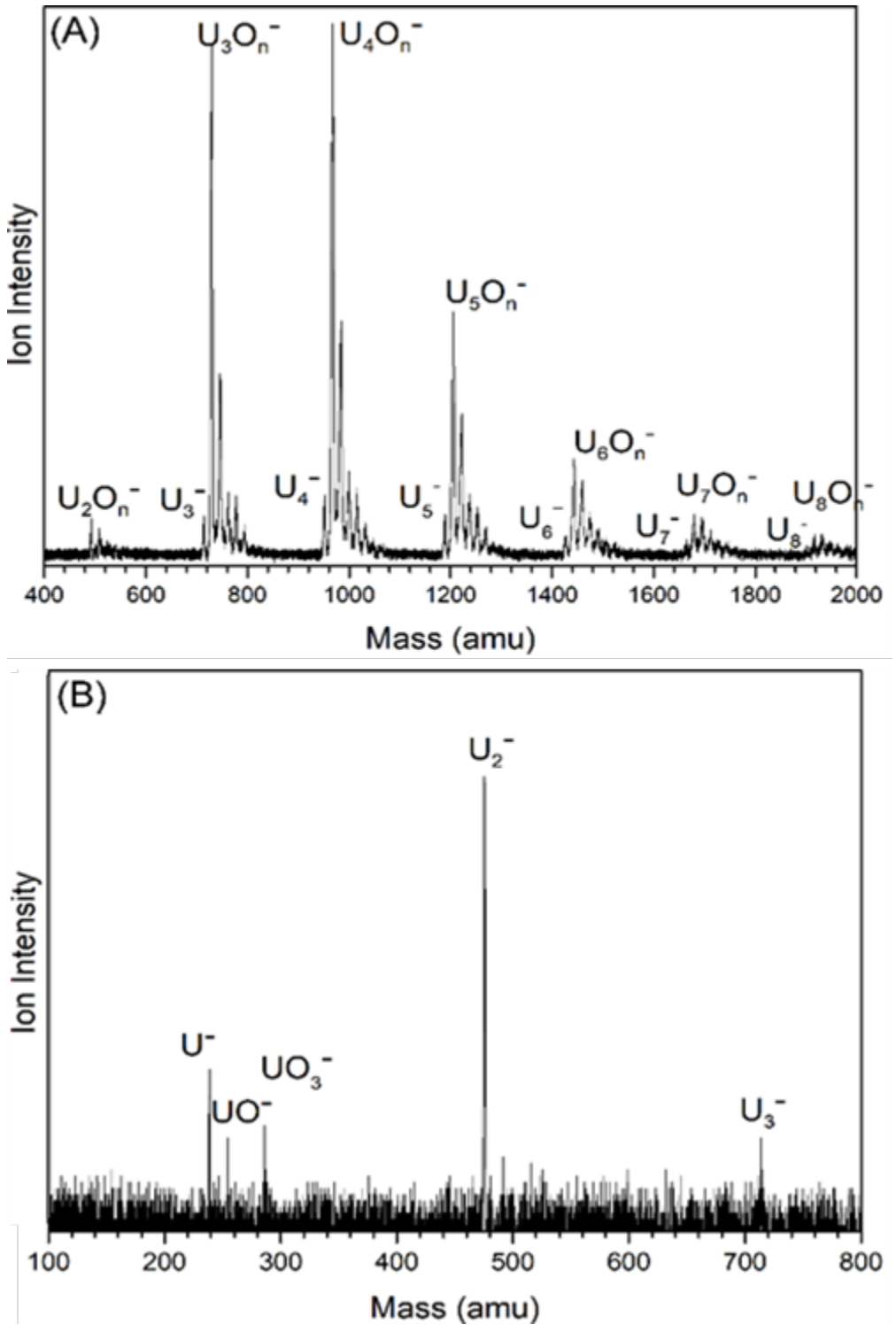

Figure 6.2: Mass spectra resulting from the use of: (A) a conventional (one-stage) laser vaporization source versus (B) using a two-stage laser vaporization source.

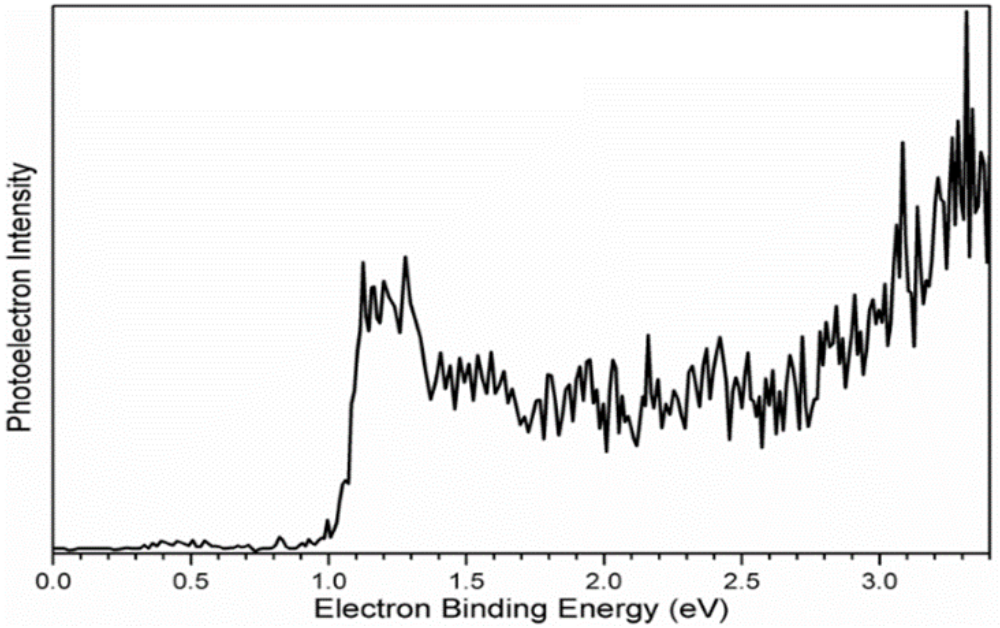

Figure 6.3: Anion Photoelectron Spectrum of the Uranium Dimer Anion, U_2^-. This spectrum was measured using the third harmonic (355 nm, 3.49 eV) of a Nd:YAG laser.

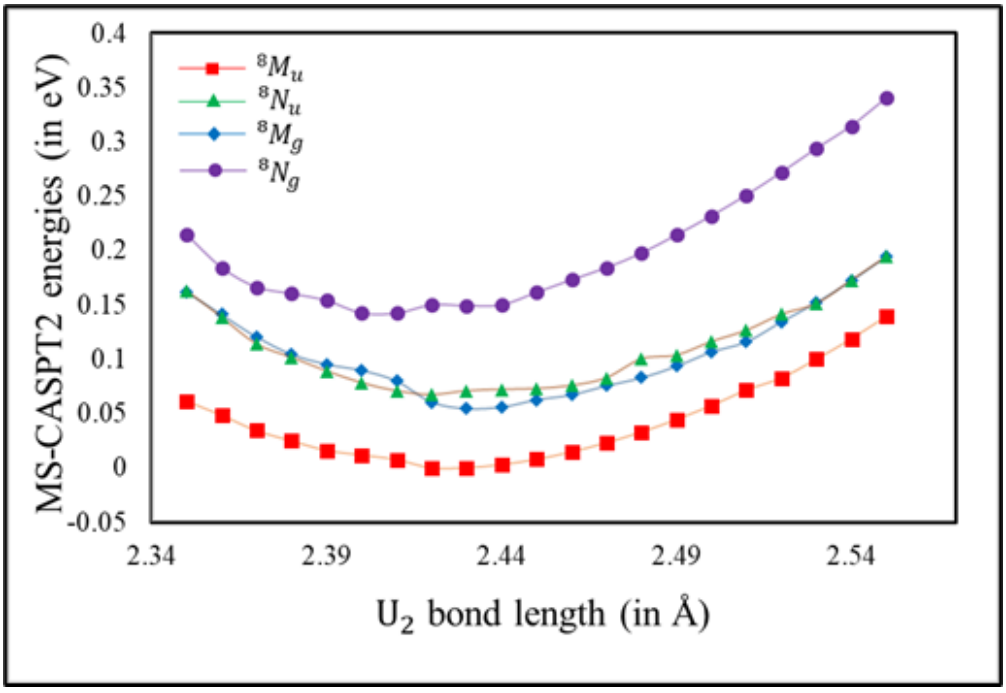

Figure 6.4: MS-CASPT2 potential energy curves for the lowest-lying elec-tronic states of U_2^- near its equilibrium geometry.

state-averaged complete active space self-consistent field (CASSCF) type[271], followed by a multi-state second order perturbation theory (MS-CASPT2) treatment[272,273] to account for both static and dynamic correlation effects, were performed to determine electronic energies (Fig. 4) at bond distances near the equilibrium bond distances of the U_2 and U_2^- systems. The ground state for U_2 is determined as $^7O_g(8_g)$, (without and with spin-orbit coupling notations) which is in agreement with the reported ground state[87]. It should be noted that although Knecht et al.[88] used fully relativistic CASSCF calculations to determine 9g as the electronic ground state and 8_g as a low-lying excited state, their calculations did not include dynamical correlation effects required to fully understand the electronic structure of U_2. (More details in SI of reference[95])

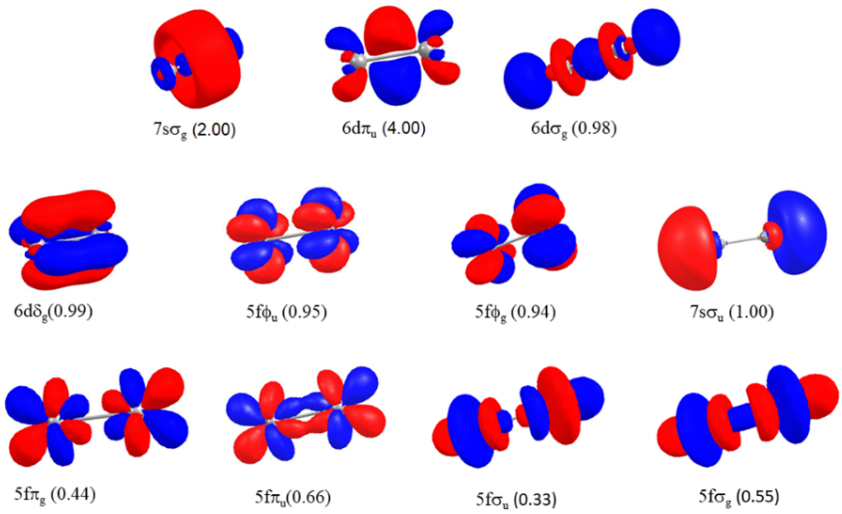

Figure 6.5: The active molecular orbitals along with the number of electrons occupying the orbitals (in brackets) for the uranium dimer anion.

Similarly to U_2, for U_2^-, the highest spin state, i.e., the octet, is found to be the most stable electronic state with an angular momentum (Λ) of 9 a.u. and ungerade symmetry. The wave-function for the ground state of U_2^- can be expressed as a linear combination of two

dominant configurations:

$$\psi = 0.736(7s\sigma_g)^2(6d\pi_u)^4(6d\sigma_g)^1(6d\delta_g)^1(5f\sigma_g)^1(5f\pi_u)^1(5f\phi_u)^1(5f\phi_g)^1(7s\sigma_u)^1$$

and

$$0.560(7s\sigma_g)^2(6d\pi_u)^4(6d\sigma_g)^1(6d\delta_g)^1(5f\sigma_u)^1(5f\pi_g)^1(5f\phi_u)^1(5f\phi_g)^1(7s\sigma_u)^1 \qquad (6.1)$$

as well as other non-dominant terms.

The bonding in U_2^- can be understood in terms of an effective bond order defined as in equation (6.2)

$$E_{ebo} = \frac{1}{2}\sum_i \left(n_{be_i} - n_{abe_i}\right) \qquad (6.2)$$

Here, n_{be_i} and n_{abe_i} represent the electron occupation numbers in the i^{th} pair of bonding and anti-bonding natural orbitals, respectively. Furthermore, the summation runs over all pairs of bonding and anti-bonding orbitals. The calculations indicate that U_2^- has a formal quadrupole bond corresponding to a calculated effective bond order of 3.7. The natural orbitals providing the main contributions to forming U_2^- are presented in Fig. 5 along with their respective occupation numbers. The wave-function for the ground state of U_2^- can be expressed as a linear combination of two dominant configurations as was shown by Gagliardi et al.[87]:

$$\psi = 0.774(7s\sigma_g)^2(6d\pi_u)^4(6d\sigma_g)^1(6d\delta_g)^1(5f\pi_u)^1(5f\delta_g)^1(5f\phi_u)^1(5f\phi_g)^1$$

and

$$0.597(7s\sigma_g)^2(6d\pi_u)^4(6d\sigma_g)^1(6d\delta_g)^1(5f\pi_g)^1(5f\delta_u)^1(5f\phi_u)^1(5f\phi_g)^1 \qquad (6.3)$$

as well as other non-dominant terms. As seen in equation (6.1), the anti-bonding $7s\sigma_u$ orbital

is occupied in all the dominant configurations of U_2^-, thereby resulting in a decrease in bond order. Thus, according to our analysis, U_2 has a formal weak quintuple bond with a bond order of 4.2, whereas U_2^- has a formal quadrupole bond with a bond order of 3.7. The formal bond orders of the two molecules differ by one unit, but the effective bond orders differ by 0.5 unit. It should be noted that although the 7su orbital has been assigned as "anti-bonding" from symmetry considerations, it has some non-bonding character. A detailed discussion on this is provided in the SI of reference[95].

Both scalar relativistic effects and spin-orbital coupling have been accounted for. Scalar relativistic effects are introduced through one-body terms in the Douglas-Kroll—Hess (DKH) Hamiltonian[275–277]. Moreover, spin-orbit (SO) coupling is added as a posteriori correction to DKH and calculated by allowing fully-optimized CASSCF states to interact under a SO Hamiltonian along with a shift in the diagonal terms to account for dynamic correction added through perturbation theory. This indicates that the effects caused due to the coupling of electronic and spin states are similar for the two species and therefore cancel out. The equilibrium distances for U_2 and U_2^- are found to be 2.42 Å and 2.43 Å, respectively. This is consistent with a photoelectron origin band that is devoid of an extended vibrational progression. The harmonic vibrational frequencies for the ground state of U_2 and U_2^- are calculated to be 265 and 220 cm^{-1}, respectively, too small to have been resolved in the present experiment. The calculated EA value of the uranium dimer, U_2, is found to be 0.71 eV (see Table S2). This computed EA value is lower than the experimentally-obtained electron affinity by 0.29 eV. We observed that even though the spin-orbit-coupling effects play a major role in altering the absolute bond energies of the uranium dimer and uranium dimer anion, they have a minimal contribution in changing the electron affinity. Our theoretical calculations predict U_2^- to have both a higher dissociation energy and a lower absolute energy than the uranium dimer, U_2, consistent with its occurrence and observation in the gas phase.

6.5 Conclusion

The original computational determination by Gagliardi and Roos[87], that the ground state of U_2 is characterized by a quintuple bond, was challenged by the computational work of Knecht, Jensen, and Saue[88], who instead found the ground state of U_2 to be described as possessing a quadrupole bond. The present work has two synergetic parts. Its new, higher level computations confirmed the original U_2 quintuple bond conclusion of Gagliardi and Roos and also found U_2^- to possess a quadrupole bond. Its experimental arm measured the anion photoelectron spectrum of U_2^-, thus providing the electron affinity of neutral U_2. Comparison of its experimentally-determined EA(U_2) value, i.e., 1.0 eV, with its computationally-determined EA(U_2) value, i.e., 0.71 eV largely supported our calculations. Because electronic structure calculations on the uranium dimer, U_2, and its anion, U_2^-, are extraordinarily demanding, perfect agreement would have been a high bar. Another way to validate our computational results is to calculate the dissociation energies of U_2^- and U_2 and to take their difference. An energetic cycle shows that EA(U_2) – EA(U) = $D_0(U_2^-)$ - $D_0(U_2)$. Knowing that EA(U_2^-) = 1.0 eV from our present experimental work and that EA(U) = 0.31 eV from our recent experimental work[285,286], implies that $D_0(U_2^-)$ - $D_0(U_2)$ is 0.69 eV. The difference between separately calculated $D_0(U_2^-)$ and $D_0(U_2)$ values in this work is 0.61 eV, in close accord with the expected value. Table S6 summaries several calculated properties of U_2 and U_2^-. Even if both calculated EA(U_2) and EA(U) values differ from the experimental ones by about 0.3 eV, the calculated difference EA(U_2) - EA(U), agrees well with the experimental one, because of error cancellation.

ACKNOWLEDGMENT

The experimental part of this material was supported by the U. S. Department of Energy (DOE), Office of Science,Basic Energy Sciences, Heavy Element Chemistry program under

award number DE-SC0019317(K.H.B.). The theoretical calculations are based on work supported by the U.S. Department of Energy(DOE),Office of Basic Energy Sciences, Division of Chemical Sciences,Geosciences, and Biosciencesundergrant no. USDOE/DE-SC002183 (L.G.). This work was completed with computing resources provided by the Minnesota Super- computing Facility (MSI) (L.G.).

CHAPTER 7

CONCLUSIONS

In this thesis, we have developed and applied electronic structure methods intended for modeling large molecules and extended materials, which are essential for advancements in materials discovery and heterogeneous catalysis. These methods, which have been applied to a wide variety of molecules and materials as presented in the preceding chapters, are based on the concept of quantum embedding and correlated wavefunction techniques, utilizing both classical and quantum computing platforms. While this divide-and-conquer strategy significantly reduces the computational cost for modeling properties, we have taken extra care not to compromise accuracy while doing so.

In Chapter 2, we introduced the state-averaged complete active space self-consistent field with density matrix embedding theory (CAS-DMET) and n-electron valence state second-order perturbation theory with density matrix embedding (NEVPT2-DMET) methods to investigate excited states in spin-defects within periodic solids, where conventional CASSCF and NEVPT2 calculations prove impractical. The excited states of these spin defects are significant due to their potential as qubit candidates in quantum computing and their roles in heterogeneous catalysis. We apply NEVPT2-DMET to study the absorption spectra of the NV^- and SiV^0 defects in diamond, and neutral oxygen vacancies (OV^0) on the surface as well as in the bulk of magnesium oxide and compare them to their experimental counterparts demonstrating reasonable accuracy only except the SiV^0 defect in diamond.

In Chapter 3, we extended our periodic DMET formalism to model surface adsorption with the goal of advancing our understanding of heterogeneous catalysis. Additionally, we introduced a memory-efficient formalism that facilitates the investigation of larger fragment subspaces, which is important for catalysis applications. We applied this to study CO adsorption on the MgO surface where our embedding formalism achieved the accuracy of conventional non-embedded calculations at a significantly cheaper computational cost, both in terms of

memory and computational time.

The need for larger embedding spaces significantly increases the computational demand of NEVPT2-DMET, as discussed in chapter 2. Therefore, in Chapter 4, we introduced the more cost-effective density matrix embedding with pair-density functional theory (DME-PDFT) method to accurately model both static and dynamic correlation in strongly correlated ground and excited states. We showcased the efficacy of DME-PDFT by applying it to study excited states of large supercells for neutral oxygen vacancies on the magnesium oxide surface.

Despite these advances, a significant challenge remains —the computational cost scales factorially with the size of the active space, thereby limiting the applicability of CAS-DMET/ NEVPT2-DMET/ DME-PDFT on problems where larger active spaces are desirable. Hence, we developed the localized active space unitary selective coupled cluster with singles and doubles (LAS-USCCSD) method, which takes an active space fragmentation approach using LASSCF as the initial wavefunction and reintroduces the correlation between fragments using a selected UCC ansatz on a quantum simulator. This method, as described in chapter 5 has only been tested on statevector simulators for molecular systems ranging from hydrogen chains to a bimetallic chromium dimer and is yet to be run on quantum hardware. When fault-tolerant quantum computers start being available, LAS-USCCSD promises to model much larger active spaces than is possible using standard classical computers without compromising accuracy.

In chapter 6, we present an application of multireference methods to studying actinide dimers, a regime of chemistry where single reference methods are insufficient. We studied metal-metal bonding in both the neutral and negatively charged uranium dimers and using state-of-the-art multireference methods, we found that U_2 has a formal quintuple bond and U_2^- has a quadruple bond. This application also showed that the use of multireference methods proves costly even for dimers.

This leads us to the future directions. Our strongly correlated quantum embedding methods are effective for multireference ground and excited states but are single-state methods in the multireference dynamic correlation regime. Hence, they will be inadequate when strong nuclear-electron coupling becomes important, such as in conical intersections, locally avoided crossings, or densely populated electronic states, as observed in the uranium dimer. To address this, CAS-DMET, NEVPT2-DMET, DME-PDFT, and LAS-USCCSD should be expanded to include multi-state versions, such as quasi-degenerate NEVPT2 (QD-NEVPT2)[287] or linearized pair-density functional theory (L-PDFT)[288,289]. Additionally, developing nuclear gradients for geometry optimization in both ground and excited states of CAS-DMET is essential. Often, to align with experimentally relevant metrics like the zero phonon line—as was necessary for the SiV^0 defect in diamond—we need the geometry for excited states. For quantum computing, an immediate next step is implementing LAS-USCCSD on quantum hardware to harness quantum advantage as fault-tolerant quantum computers become available. This approach can be extended to materials using the CAS-DMET framework, where the CASSCF solver could be replaced by a LAS-USCCSD solver to handle larger active spaces, followed by a DME-PDFT procedure to capture dynamic correlation. These developments are promising, and I hope that my thesis has contributed significantly to the field of quantum chemistry method development using both classical and quantum computers. I anticipate that these contributions will further aid in materials discovery and drug development in the future.

REFERENCES

[1] Mitra, A.; Pham, H. Q.; Pandharkar, R.; Hermes, M. R.; Gagliardi, L. Excited States of Crystalline Point Defects with Multireference Density Matrix Embedding Theory. *J. Phys. Chem. Lett* **2021**, *12*, 11688–11694.

[2] Schrödinger, E. An Undulatory Theory of the Mechanics of Atoms and Molecules. *Physical Review* **1926**, *28*, 1049–1070.

[3] Cramer, C. J. *Essentials of Computational Chemistry*; 2004.

[4] Born, M.; Oppenheimer, R. Zur Quantentheorie der Molekeln. *Annalen der Physik* **1927**, *389*, 457–484.

[5] Tully, J. C. Perspective on "Zur Quantentheorie der Molekeln". *Theoretical Chemistry Accounts* **2000**, *103*, 173–176.

[6] Tew, D. P.; Klopper, W.; Helgaker, T. Electron correlation: The many-body problem at the heart of chemistry. *Journal of Computational Chemistry* **2007**, *28*, 1307–1320.

[7] Szabo, A.; Ostlund, N. S. *Modern Quantum Chemistry: Introduction to Advanced Electronic Structure Theory*, 1st ed.; Dover Publications, Inc.: Mineola, 1996.

[8] Slater, J. C. A Generalized Self-Consistent Field Method. *Physical Review* **1953**, *91*, 528–530.

[9] Dirac, P. A. M.; Fowler, R. H. On the theory of quantum mechanics. *Proceedings of the Royal Society of London. Series A, Containing Papers of a Mathematical and Physical Character* **1926**, *112*, 661–677.

[10] Dirac, P. A. M.; Bohr, N. H. D. The quantum theory of the emission and absorption of radiation. *Proceedings of the Royal Society of London. Series A, Containing Papers of a Mathematical and Physical Character* **1927**, *114*, 243–265.

[11] Helgaker, T.; Jørgensen, P.; Olsen, J. *Molecular Electronic-Structure Theory*; Wiley, 2000.

[12] Löwdin, P.-O. Quantum Theory of Many-Particle Systems. *Phys. Rev.* **1955**, *97*, 1474–1489.

[13] Pople, J. A.; Binkley, J. S.; Seeger, R. Theoretical models incorporating electron correlation. *International Journal of Quantum Chemistry* **1976**, *10*, 1–19.

[14] Čížek, J. On the Correlation Problem in Atomic and Molecular Systems. Calculation of Wavefunction Components in Ursell-Type Expansion Using Quantum-Field Theoretical Methods. *The Journal of Chemical Physics* **1966**, *45*, 4256–4266.

[15] Bartlett, R. J. Many-Body Perturbation Theory and Coupled Cluster Theory for Electron Correlation in Molecules. *Annual Review of Physical Chemistry* **1981**, *32*, 359–401.

[16] Hampel, C.; Werner, H. Local treatment of electron correlation in coupled cluster theory. *The Journal of Chemical Physics* **1996**, *104*, 6286–6297.

[17] Raghavachari, K.; Anderson, J. B. Electron Correlation Effects in Molecules. *The Journal of Physical Chemistry* **1996**, *100*, 12960–12973.

[18] Balint-Kurti, G. G. Electron Correlation in Small Molecules. *Physics Bulletin* **1978**, *29*, 25.

[19] Marti, K. H.; Reiher, M. New electron correlation theories for transition metal chemistry. *Physical Chemistry Chemical Physics* **2011**, *13*, 6750–6759.

[20] Urban, M.; Černušák, I.; Kellö, V.; Noga, J. Electron Correlation in Molecules. *Methods in Computational Chemistry* **1987**, 117–250.

[21] Hollett, J. W.; Loos, P.-F. Capturing static and dynamic correlation with ΔNO-MP2 and ΔNO-CCSD. *The Journal of Chemical Physics* **2020**, *152*, 14101.

[22] Mok, D. K. W.; Neumann, R.; Handy, N. C. Dynamical and Nondynamical Correlation. *The Journal of Physical Chemistry* **1996**, *100*, 6225–6230.

[23] Molawi, K.; Cohen, A. J.; Handy, N. C. Left–right and dynamic correlation. *International Journal of Quantum Chemistry* **2002**, *89*, 86–93.

[24] Cohen, A. J.; Handy, N. C. Dynamic correlation. *Molecular Physics* **2001**, *99*, 607–615.

[25] Delin, K. A.; Orlando, T. P. *Electronics, Power Electronics, Optoelectronics, Microwaves, Electromagnetics, and Radar*; 2006.

[26] Roos, B. O.; Taylor, P. R.; Sigbahn, P. E. A Complete Active Space SCF Method (CASSCF) using A Density Matrix Formulated Super-CI Approach. *Chem. Phys.* **1980**, *48*, 157 – 173.

[27] Siegbahn, P. E. M.; Almlöf, J.; Heiberg, A.; Roos, B. O. The Complete Active Space SCF (CASSCF) Method in A Newton–Raphson Formulation with Application to The HNO Molecule. *J. Chem. Phys.* **1981**, *74*, 2384–2396.

[28] Siegbahn, P.; Heiberg, A.; Roos, B.; Levy, B. A Comparison of The Super-CI and The Newton-Raphson Scheme in The Complete Active Space SCF Method. *Phys. Scr.* **1980**, *21*, 323–327.

[29] Buenker, R. J.; Peyerimhoff, S. D. Individualized configuration selection in CI calculations with subsequent energy extrapolation. *Theoretica chimica acta* **1974**, *35*, 33–58.

[30] Buenker, R. J.; Peyerimhoff, S. D.; Butscher, W. Applicability of the multi-reference double-excitation CI (MRD-CI) method to the calculation of electronic wavefunctions and comparison with related techniques. *Mol. Phys.* **1978**, *35*, 771–791.

[31] Bell, A. T.; Head-Gordon, M. Quantum Mechanical Modeling of Catalytic Processes. *Annual Review of Chemical and Biomolecular Engineering* **2011**, *2*, 453–477, PMID: 22432627.

[32] Krylov, A.; Windus, T. L.; Barnes, T.; Marin-Rimoldi, E.; Nash, J. A.; Pritchard, B.; Smith, D. G. A.; Altarawy, D.; Saxe, P.; Clementi, C.; Crawford, T. D.; Harrison, R. J.; Jha, S.; Pande, V. S.; Head-Gordon, T. Perspective: Computational chemistry software and its advancement as illustrated through three grand challenge cases for molecular science. *J. Chem. Phys.* **2018**, *149*, 180901.

[33] Xu, S.; Carter, E. A. Theoretical Insights into Heterogeneous (Photo)electrochemical CO2 Reduction. *Chem. Rev.* **2019**, *119*, 6631–6669, PMID: 30561988.

[34] Dreyer, C. E.; Alkauskas, A.; Lyons, J. L.; Janotti, A.; Van de Walle, C. G. First-Principles Calculations of Point Defects for Quantum Technologies. *Annual Review of Materials Research* **2018**, *48*, 1–26.

[35] Wasielewski, M. R. et al. Exploiting chemistry and molecular systems for quantum information science. *Nat. Rev. Chem.* **2020**, *4*, 490–504.

[36] Hohenberg, P.; Kohn, W. Inhomogeneous Electron Gas. *Physical Review* **1964**, *136*, B864–B871.

[37] Kohn, W.; Sham, L. J. Self-Consistent Equations Including Exchange and Correlation Effects. *Physical Review* **1965**, *140*, A1133–A1138.

[38] Jones, R. O.; Gunnarsson, O. The density functional formalism, its applications and prospects. *Reviews of Modern Physics* **1989**, *61*, 689–746.

[39] Cohen, A. J.; Mori-Sánchez, P.; Yang, W. Insights into current limitations of density functional theory. *Science* **2008**, *321*, 792–794.

[40] Cohen, A. J.; Mori-Sánchez, P.; Yang, W. Challenges for Density Functional Theory. *Chemical Reviews* **2012**, *112*, 289–320.

[41] Su, N. Q.; Li, C.; Yang, W. Describing strong correlation with fractional-spin correction in density functional theory. *Proceedings of the National Academy of Sciences* **2018**, *115*, 9678 LP – 9683.

[42] Bednorz, J. G.; Müller, K. A. Possible highTc superconductivity in the Ba–La–Cu–O system. *Zeitschrift für Physik B Condensed Matter* **1986**, *64*, 189–193.

[43] Cramer, C. J.; Truhlar, D. G. Density functional theory for transition metals and transition metal chemistry. *Physical Chemistry Chemical Physics* **2009**, *11*, 10757–10816.

[44] Marsman, M.; Grüneis, A.; Paier, J.; Kresse, G. Second-order Møller–Plesset perturbation theory applied to extended systems. I. Within the projector-augmented-wave formalism using a plane wave basis set. *J. Chem. Phys.* **2009**, *130*, 184103.

[45] Müller, C.; Paulus, B. Wavefunction-based electron correlation methods for solids. *Phys. Chem. Chem. Phys* **2012**, *14*, 7605.

[46] Gruber, T.; Liao, K.; Tsatsoulis, T.; Hummel, F.; Grüneis, A. Applying the Coupled-Cluster Ansatz to Solids and Surfaces in the Thermodynamic Limit. *Physical Review X* **2018**, *8*, 21043.

[47] Wang, X.; Berkelbach, T. C. Excitons in Solids from Periodic Equation-of-Motion Coupled-Cluster Theory. *J. Chem. Theory Comput.* **2020**, *16*, 3095–3103.

[48] Gao, Y.; Sun, Q.; Yu, J. M.; Motta, M.; McClain, J.; White, A. F.; Minnich, A. J.; Chan, G. K.-L. Electronic structure of bulk manganese oxide and nickel oxide from coupled cluster theory. *Physical Review B* **2020**, *101*, 165138.

[49] Sun, Q.; Chan, G. K.-L. Quantum Embedding Theories. *Accounts of Chemical Research* **2016**, *49*, 2705–2712.

[50] Cortona, P. Self-consistently determined properties of solids without band-structure calculations. *Phys. Rev. B* **1991**, *44*, 8454–8458.

[51] Wesolowski, T. A.; Warshel, A. Frozen density functional approach for ab initio calculations of solvated molecules. *J. Phys. Chem.* **1993**, *97*, 8050–8053.

[52] Elliott, P.; Cohen, M. H.; Wasserman, A.; Burke, K. Density Functional Partition Theory with Fractional Occupations. *J. Chem. Theory Comput.* **2009**, *5*, 827–833, PMID: 26609589.

[53] Elliott, P.; Burke, K.; Cohen, M. H.; Wasserman, A. Partition density-functional theory. *Phys. Rev. A* **2010**, *82*, 024501.

[54] Jacob, C. R.; Neugebauer, J. Subsystem density-functional theory. *WIREs Computational Molecular Science* **2014**, *4*, 325–362.

[55] Libisch, F.; Huang, C.; Carter, E. A. Embedded Correlated Wavefunction Schemes: Theory and Applications. *Acc. Chem. Res.* **2014**, *47*, 2768–2775.

[56] Wesolowski, T. A.; Shedge, S.; Zhou, X. Frozen-Density Embedding Strategy for Multilevel Simulations of Electronic Structure. *Chem. Rev.* **2015**, *115*, 5891–5928.

[57] Fasulo, F.; Mitra, A.; Muñoz-García, A. B.; Pavone, M.; Gagliardi, L. Unveiling the Role of Surface Ir-Oxo Species in O2 Evolution at IrO2 Electrocatalysts via Embedded Cluster Multireference Calculations. *The Journal of Physical Chemistry C* **2024**, *128*, 7343–7351.

[58] Kotliar, G.; Savrasov, S. Y.; Haule, K.; Oudovenko, V. S.; Parcollet, O.; Marianetti, C. A. Electronic structure calculations with dynamical mean-field theory. *Rev. Mod. Phys.* **2006**, *78*, 865–951.

[59] Zgid, D.; Chan, G. K.-L. Dynamical mean-field theory from a quantum chemical perspective. *J. Chem. Phys.* **2011**, *134*, 094115.

[60] Chibani, W.; Ren, X.; Scheffler, M.; Rinke, P. Self-consistent Green's function embedding for advanced electronic structure methods based on a dynamical mean-field concept. *Phys. Rev. B* **2016**, *93*, 165106.

[61] Zgid, D.; Gull, E. Finite temperature quantum embedding theories for correlated systems. *New Journal of Physics* **2017**, *19*, 023047.

[62] Lan, T. N.; Zgid, D. Generalized Self-Energy Embedding Theory. *J. Phys. Chem. Lett.* **2017**, *8*, 2200–2205.

[63] Ma, H.; Sheng, N.; Govoni, M.; Galli, G. Quantum Embedding Theory for Strongly Correlated States in Materials. *J. Chem. Theory Comput.* **2021**, *17*, 2116–2125.

[64] Sheng, N.; Vorwerk, C.; Govoni, M.; Galli, G. Green's Function Formulation of Quantum Defect Embedding Theory. *J. Chem. Theory Comput.* **2022**, *18*, 3512–3522.

[65] Knizia, G.; Chan, G. K.-L. Density matrix embedding: A simple alternative to dynamical mean-field theory. *Physical review letters* **2012**, *109*, 186404.

[66] Knizia, G.; Chan, G. K.-L. Density matrix embedding: A strong-coupling quantum embedding theory. *J. Chem. Theory Comput.* **2013**, *9*, 1428–1432.

[67] Wouters, S.; Jiménez-Hoyos, C. A.; Sun, Q.; Chan, G. K.-L. A Practical Guide to Density Matrix Embedding Theory in Quantum Chemistry. *J. Chem. Theory Comput.* **2016**, *12*, 2706–2719.

[68] Wouters, S.; A. Jiménez-Hoyos, C.; K.L. Chan, G. *Fragmentation*; John Wiley & Sons, Ltd, 2017; Chapter 8, pp 227–243.

[69] Veryazov, V.; Malmqvist, P. Å.; Roos, B. O. How to select active space for multiconfigurational quantum chemistry? *International Journal of Quantum Chemistry* **2011**, *111*, 3329–3338.

[70] Li Manni, G.; Carlson, R. K.; Luo, S.; Ma, D.; Olsen, J.; Truhlar, D. G.; Gagliardi, L. Multiconfiguration Pair-Density Functional Theory. *J. Chem. Theory Comput.* **2014**, *10*, 3669–3680.

[71] Gagliardi, L.; Truhlar, D. G.; Li Manni, G.; Carlson, R. K.; Hoyer, C. E.; Bao, J. L. Multiconfiguration Pair-Density Functional Theory: A New Way To Treat Strongly Correlated Systems. *Acc. Chem. Res.* **2017**, *50*, 66–73.

[72] Zhou, C.; Hermes, M. R.; Wu, D.; Bao, J. J.; Pandharkar, R.; King, D. S.; Zhang, D.; Scott, T. R.; Lykhin, A. O.; Gagliardi, L.; Truhlar, D. G. Electronic structure of strongly correlated systems: recent developments in multiconfiguration pair-density functional theory and multiconfiguration nonclassical-energy functional theory. *Chem. Sci.* **2022**, *13*, 7685–7706.

[73] Parker, S. M.; Seideman, T.; Ratner, M. A.; Shiozaki, T. Communication: Active-space decomposition for molecular dimers. *J. Chem. Phys.* **2013**, *139*, 21108.

[74] Parker, S. M.; Seideman, T.; Ratner, M. A.; Shiozaki, T. Model Hamiltonian Analysis of Singlet Fission from First Principles. *J. Phys. Chem. C* **2014**, *118*, 12700–12705.

[75] Parker, S. M.; Shiozaki, T. Quasi-diabatic States from Active Space Decomposition. *J. Chem. Theory Comput.* **2014**, *10*, 3738–3744.

[76] Kim, I.; Parker, S. M.; Shiozaki, T. Orbital Optimization in the Active Space Decomposition Model. *J. Chem. Theory Comput.* **2015**, *11*, 3636–3642.

[77] Jiménez-Hoyos, C. A.; Scuseria, G. E. Cluster-based mean-field and perturbative description of strongly correlated fermion systems: Application to the one- and two-dimensional Hubbard model. *Phys. Rev. B* **2015**, *92*, 85101.

[78] Nishio, S.; Kurashige, Y. Rank-one basis made from matrix-product states for a low-rank approximation of molecular aggregates. *J. Chem. Phys.* **2019**, *151*, 84110.

[79] Nishio, S.; Kurashige, Y. Importance of dynamical electron correlation in diabatic couplings of electron-exchange processes. *J. Chem. Phys.* **2022**, *156*, 114107.

[80] Abraham, V.; Mayhall, N. J. Selected Configuration Interaction in a Basis of Cluster State Tensor Products. *J. Chem. Theory Comput.* **2020**, *16*, 6098–6113.

[81] Malmqvist, P. A.; Rendell, A.; Roos, B. O. The restricted active space self-consistent-field method, implemented with a split graph unitary group approach. *J. Phys. Chem.* **1990**, *94*, 5477–5482.

[82] Olsen, J.; Roos, B. O.; Jo/rgensen, P.; Jensen, H. J. A. Determinant based configuration interaction algorithms for complete and restricted configuration interaction spaces. *J. Chem. Phys.* **1988**, *89*, 2185–2192.

[83] Ma, D.; Li Manni, G.; Gagliardi, L. The generalized active space concept in multiconfigurational self-consistent field methods. *J. Chem. Phys.* **2011**, *135*, 044128.

[84] Hermes, M. R.; Gagliardi, L. Multiconfigurational Self-Consistent Field Theory with Density Matrix Embedding: The Localized Active Space Self-Consistent Field Method. *J. Chem. Theory Comput.* **2019**, *15*, 972–986.

[85] Hermes, M. R.; Pandharkar, R.; Gagliardi, L. Variational Localized Active Space Self-Consistent Field Method. *J. Chem. Theory Comput.* **2020**, *16*, 4923–4937.

[86] Alexeev, Y. et al. *Quantum-centric Supercomputing for Materials Science: A Perspective on Challenges and Future Directions*; 2023; 60 pages, 14 figures; comments welcome.

[87] Gagliardi, L.; Roos, B. O. Quantum chemical calculations show that the uranium molecule U2 has a quintuple bond. *Nature* **2005**, *433*, 848–851.

[88] Knecht, S.; Jensen, H. J. A.; Saue, T. Relativistic quantum chemical calculations show that the uranium molecule U2 has a quadruple bond. *Nature Chemistry* **2018**, *11*, 40–44.

[89] Roos, B. O.; Malmqvist, P.-Å.; Gagliardi, L. Exploring the Actinide-Actinide Bond: Theoretical Studies of the Chemical Bond in Ac2, Th2, Pa2, and U2. *Journal of the American Chemical Society* **2006**, *128*, 17000–17006.

[90] Gagliardi, L.; Roos, B. O. Multiconfigurational quantum chemical methods for molecular systems containing actinides. *Chemical Society Reviews* **2007**, *36*, 893.

[91] Bursten, B. E.; Ozin, G. A. X. alpha.-SW calculations for naked actinide dimers: existence of. vphi. bonds between metal atoms. *Inorganic Chemistry* **1984**, *23*, 2910–2911.

[92] Pepper, M.; Bursten, B. E. Ab initio studies of the electronic structure of the diuranium molecule. *Journal of the American Chemical Society* **1990**, *112*, 7803–7804.

[93] Erkoç, c.; Baştuğ, T.; Hirata, M.; Tachimori, S. Molecular-Dynamics Simulations of Uranium Microclusters. *Journal of the Physical Society of Japan* **1999**, *68*, 440–445.

[94] Gingerich, K. A. Experimental and predicted stability of diatomic metals and metallic clusters. *Faraday Symposia of the Chemical Society* **1980**, *14*, 109.

[95] Ciborowski, S. M.; Mitra, A.; Harris, R. M.; Liu, G.; Sharma, P.; Khetrapal, N.; Blankenhorn, M.; Gagliardi, L.; Bowen, K. H. Metal–Metal Bonding in Actinide Dimers: U2 and U2–. *Journal of the American Chemical Society* **2021**, *143*, 17023–17028.

[96] Mitra, A.; Hermes, M. R.; Cho, M.; Agarawal, V.; Gagliardi, L. Periodic Density Matrix Embedding for CO Adsorption on the MgO(001) Surface. *J. Phys. Chem. Lett.* **2022**, *13*, 7483–7489.

[97] Mitra, A.; Hermes, M. R.; Gagliardi, L. Density Matrix Embedding Using Multiconfiguration Pair-Density Functional Theory. *J. Chem. Theory Comput.* **2023**, *19*, 3498–3508.

[98] Mitra, A.; D'Cunha, R.; Wang, Q.; Hermes, M. R.; Alexeev, Y.; Gray, S. K.; Otten, M.; Gagliardi, L. The Localized Active Space Method with Unitary Selective Coupled Cluster. *arXiv preprint arXiv:2404.12927 [physics, physics:quant-ph]* **2024**,

[99] Haldar, S.; Mitra, A.; Hermes, M. R.; Gagliardi, L. Local Excitations of a Charged Nitrogen Vacancy in Diamond with Multireference Density Matrix Embedding Theory. *J. Phys. Chem. Lett.* **2023**, *14*, 4273–4280.

[100] Verma, S.; Mitra, A.; Jin, Y.; Haldar, S.; Vorwerk, C.; Hermes, M. R.; Galli, G.; Gagliardi, L. Optical Properties of Neutral F Centers in Bulk MgO with Density Matrix Embedding. *J. Phys. Chem. Lett.* **2023**, *14*, 7703–7710.

[101] Sun, Q.; Chan, G. K.-L. Quantum Embedding Theories. *Acc. Chem. Res.* **2016**, *49*, 2705–2712.

[102] Hohenberg, P.; Kohn, W. Inhomogeneous Electron Gas. *Phys. Rev.* **1964**, *136*, B864–B871.

[103] Kohn, W.; Sham, L. J. Self-Consistent Equations Including Exchange and Correlation Effects. *Phys. Rev.* **1965**, *140*, A1133–A1138.

[104] Knizia, G.; Chan, G. K.-L. Density Matrix Embedding: A Simple Alternative to Dynamical Mean-Field Theory. *Phys. Rev. Lett.* **2012**, *109*, 186404.

[105] Knizia, G.; Chan, G. K.-L. Density Matrix Embedding: A Strong-Coupling Quantum Embedding Theory. *J. Chem. Theory Comput.* **2013**, *9*, 1428–1432.

[106] Wouters, S.; Jiménez-Hoyos, C. A.; Sun, Q.; Chan, G. K.-L. A Practical Guide to Density Matrix Embedding Theory in Quantum Chemistry. *J. Chem. Theory Comput.* **2016**, *12*, 2706–2719.

[107] Peschel, I.; Eisler, V. Reduced Density Matrices and Entanglement Entropy in Free Lattice Models. *J. Phys. A* **2009**, *42*, 504003.

[108] Pham, H. Q.; Hermes, M. R.; Gagliardi, L. Periodic Electronic Structure Calculations with The Density Matrix Embedding Theory. *J. Chem. Theory Comput.* **2020**, *16*, 130–140.

[109] Cui, Z.-H.; Zhu, T.; Chan, G. K.-L. Efficient Implementation of Ab Initio Quantum Embedding in Periodic Systems: Density Matrix Embedding Theory. *J. Chem. Theory Comput.* **2020**, *16*, 119–129.

[110] Angeli, C.; Cimiraglia, R.; Evangelisti, S.; Leininger, T.; Malrieu, J.-P. Introduction of n-electron Valence States for Multireference Perturbation Theory. *J. Chem. Phys.* **2001**, *114*, 10252–10264.

[111] Angeli, C.; Borini, S.; Cestari, M.; Cimiraglia, R. A Quasidegenerate Formulation of The Second Order N-Electron Valence State Perturbation Theory Approach. *J. Chem. Phys.* **2004**, *121*, 4043–4049.

[112] N-electron Valence State Perturbation Theory: A Fast Implementation of The Strongly Contracted Variant. *Chem. Phys. Lett* **2001**, *350*, 297 – 305.

[113] Angeli, C.; Cimiraglia, R.; Malrieu, J.-P. N-electron Valence State Perturbation Theory: A Spinless Formulation and An Efficient Implementation of The Strongly Contracted and of The Partially Contracted Variants. *J. Chem. Phys.* **2002**, *117*, 9138–9153.

[114] Pham, H. Q.; Bernales, V.; Gagliardi, L. Can Density Matrix Embedding Theory with The Complete Activate Space Self-Consistent Field Solver Describe Single and Double Bond Breaking in Molecular Systems? *J. Chem. Theory Comput.* **2018**, *14*, 1960–1968.

[115] Bulik, I. W.; Scuseria, G. E.; Dukelsky, J. Density Matrix Embedding from Broken Symmetry Lattice Mean Fields. *Phys. Rev. B* **2014**, *89*, 035140.

[116] Tran, H. K.; Ye, H.-Z.; Van Voorhis, T. Bootstrap Embedding with An Unrestricted Mean-field Bath. *J. Chem. Phys.* **2020**, *153*, 214101.

[117] Zheng, B.-X.; Chan, G. K.-L. Ground-State Phase Diagram of The Square Lattice Hubbard Model from Density Matrix Embedding Theory. *Phys. Rev. B* **2016**, *93*, 035126.

[118] Reinhard, T. E.; Mordovina, U.; Hubig, C.; Kretchmer, J. S.; Schollwöck, U.; Appel, H.; Sentef, M. A.; Rubio, A. Density-Matrix Embedding Theory Study of The One-Dimensional Hubbard-Holstein Model. *J. Chem. Theory Comput.* **2019**, *15*, 2221–2232.

[119] Marzari, N.; Vanderbilt, D. Maximally Localized Generalized Wannier Functions for Composite Energy Bands. *Phys. Rev. B* **1997**, *56*, 12847–12865.

[120] Marzari, N.; Mostofi, A. A.; Yates, J. R.; Souza, I.; Vanderbilt, D. Maximally Localized Wannier Functions: Theory and Applications. *Rev. Mod. Phys.* **2012**, *84*, 1419–1475.

[121] Pizzi, G. et al. Wannier90 as A Community Code: New Features and Applications. *J. Phys.: Condens. Matter* **2020**, *32*, 165902.

[122] Sun, Q.; Berkelbach, T. C.; Blunt, N. S.; Booth, G. H.; Guo, S.; Li, Z.; Liu, J.; McClain, J. D.; Sayfutyarova, E. R.; Sharma, S.; Wouters, S.; Chan, G. K.-L. PySCF: The Python-Based Simulations of Chemistry Framework. *Wiley Interdiscip. Rev. Comput.* **2018**, *8*, e1340.

[123] Sun, Q. et al. Recent Developments in The PySCF Program Package. *J. Chem. Phys.* **2020**, *153*, 024109.

[124] Pham, H. Q.; Hermes, M. R.; Gagliardi, L. Periodic Electronic Structure Calculations with The Density Matrix Embedding Theory. *J. Chem. Theory Comput.* **2020**, *16*, 130–140.

[125] Pham, H. Q. pDMET: A Code for Periodic DMET Calculations. 2019; `https://github.com/hungpham2017/pDMET`, accessed Sep, 29, 2021.

[126] Pham, H. Q. pyWannier90: A Python Interface for wannier90. 2019; `https://github.com/hungpham2017/pyWannier90`, accessed Sep, 29, 2021.

[127] Goedecker, S.; Teter, M.; Hutter, J. Separable Dual-Space Gaussian Pseudopotentials. *Phys. Rev. B* **1996**, *54*, 1703–1710.

[128] Perdew, J. P.; Ruzsinszky, A.; Csonka, G. I.; Vydrov, O. A.; Scuseria, G. E.; Constantin, L. A.; Zhou, X.; Burke, K. Restoring The Density-Gradient Expansion for Exchange in Solids and Surfaces. *Phys. Rev. Lett.* **2008**, *100*, 136406.

[129] Kresse, G.; Furthmüller, J. Efficiency of Ab-initio Total Energy Calculations for Metals and Semiconductors Using A Plane-wave Basis Set. *Comput. Mater. Sci.* **1996**, *6*, 15 – 50.

[130] Kresse, G.; Furthmüller, J. Efficient Iterative Schemes for Ab initio Total-energy Calculations using A Plane-wave Basis Set. *Phys. Rev. B* **1996**, *54*, 11169–11186.

[131] Kresse, G.; Hafner, J. Ab initio Molecular Dynamics for Liquid Metals. *Phys. Rev. B* **1993**, *47*, 558–561.

[132] Kresse, G.; Joubert, D. From Ultrasoft Pseudopotentials to The Projector Augmented-wave Method. *Phys. Rev. B* **1999**, *59*, 1758–1775.

[133] Szalay, P. G.; Müller, T.; Gidofalvi, G.; Lischka, H.; Shepard, R. Multiconfiguration Self-Consistent Field and Multireference Configuration Interaction Methods and Applications. *Chem. Rev.* **2012**, *112*, 108–181.

[134] Docken, K. K.; Hinze, J. LiH Potential Curves and Wavefunctions for X1sigma+, A1sigma+, B1pi,3sigma+, and 3pi. *J. Chem. Phys.* **1972**, *57*, 4928–4936.

[135] Werner, H.; Meyer, W. A Quadratically Convergent MCSCF Method for The Simultaneous Optimization of Several States. *J. Chem. Phys.* **1981**, *74*, 5794–5801.

[136] VandeVondele, J.; Krack, M.; Mohamed, F.; Parrinello, M.; Chassaing, T.; Hutter, J. Quickstep: Fast and Accurate Density Functional Calculations using A Mixed Gaussian and Plane Waves Approach. *Comput. Phys. Commun* **2005**, *167*, 103 – 128.

[137] Wang, Z.; Wang, L. Role of Oxygen Vacancy in Metal Oxide Based Photoelectrochemical Water Splitting. *EcoMat* **2021**, *3*, e12075.

[138] Sousa, C.; Tosoni, S.; Illas, F. Theoretical Approaches to Excited-State-Related Phenomena in Oxide Surfaces. *Chem. Rev.* **2013**, *113*, 4456–4495.

[139] Richter, N. A.; Sicolo, S.; Levchenko, S. V.; Sauer, J.; Scheffler, M. Concentration of Vacancies at Metal-Oxide Surfaces: Case Study of MgO(100). *Phys. Rev. Lett.* **2013**, *111*, 045502.

[140] Domínguez-Ariza, D.; Sousa, C.; Illas, F.; Ricci, D.; Pacchioni, G. Ground- and Excited-State Properties of M-center Oxygen Vacancy Aggregates in The Bulk and Surface of MgO. *Phys. Rev. B* **2003**, *68*, 054101.

[141] Gallo, A.; Hummel, F.; Irmler, A.; Grüneis, A. A Periodic Equation-of-Motion Coupled-Cluster Implementation Applied to F-Centers in Alkaline Earth Oxides. *J. Chem. Phys.* **2021**, *154*, 64106.

[142] Henrich, V. E.; Dresselhaus, G.; Zeiger, H. J. Energy-Dependent Electron-Energy-Loss Spectroscopy: Application to the Surface and Bulk Electronic Structure of MgO. *Phys. Rev. B* **1980**, *22*, 4764–4775.

[143] Kramer, J.; Ernst, W.; Tegenkamp, C.; Pfnür, H. Mechanism and Kinetics of Color Center formation on Epitaxial Thin Films of MgO. *Surf. Sci.* **2002**, *517*, 87–97.

[144] Wu, M.-C.; Truong, C. M.; Goodman, D. W. Electron-Energy-Loss-Spectroscopy Studies of Thermally Generated Defects in Pure and Lithium-Doped MgO(100) Films on Mo(100). *Phys. Rev. B* **1992**, *46*, 12688–12694.

[145] Illas, F.; Pacchioni, G. Optical Properties of Surface and Bulk F Centers in MgO from Ab Initio Cluster Model Calculations. *J. Chem. Phys.* **1998**, *108*, 7835–7841.

[146] Weber, J. R.; Koehl, W. F.; Varley, J. B.; Janotti, A.; Buckley, B. B.; Van de Walle, C. G.; Awschalom, D. D. Quantum Computing with Defects. *Proc. Natl. Acad. Sci. U.S.A.* **2010**, *107*, 8513–8518.

[147] Gali, A.; Maze, J. R. *Ab initio* Study of The Split Silicon-Vacancy Defect in Diamond: Electronic Structure and Related Properties. *Phys. Rev. B* **2013**, *88*, 235205.

[148] Thiering, G.; Gali, A. The $(e_g \otimes e_u) \otimes E_g$ Product Jahn–Teller Effect in The Neutral Group-IV Vacancy Quantum Bits in Diamond. *Npj Comput. Mater* **2019**, *5*, 18.

[149] Ivády, V.; Abrikosov, I. A.; Gali, A. First Principles Calculation of Spin-related Quantities for Point Defect Qubit Research. *Npj Comput. Mater* **2018**, *4*, 76.

[150] Ma, H.; Govoni, M.; Galli, G. Quantum Simulations of Materials on Near-Term Quantum Computers. *Npj Comput. Mater* **2020**, *6*, 85.

[151] Ma, H.; Sheng, N.; Govoni, M.; Galli, G. First-Principles Studies of Strongly Correlated States in Defect Spin Qubits in Diamond. *Phys. Chem. Chem. Phys.* **2020**, *22*, 25522–25527.

[152] Green, B. L.; Doherty, M. W.; Nako, E.; Manson, N. B.; D'Haenens-Johansson, U. F. S.; Williams, S. D.; Twitchen, D. J.; Newton, M. E. Electronic Structure of The Neutral Silicon-Vacancy Center in Diamond. *Phys. Rev. B* **2019**, *99*, 161112.

[153] Anderson, R. J.; Shiozaki, T.; Booth, G. H. Efficient and Stochastic Multireference Perturbation Theory for Large Active Spaces within A Full Configuration Interaction Quantum Monte Carlo Framework. *J. Chem. Phys.* **2020**, *152*, 054101.

[154] Haldar, S.; Mitra, A.; Hermes, M. R.; Gagliardi, L. Local Excitations of a Charged Nitrogen Vacancy in Diamond with Multireference Density Matrix Embedding Theory. *J Phys. Chem. Lett.* **2023**, 4273–4280.

[155] Ito, T.; Wang, J. X.; Lin, C. H.; Lunsford, J. H. Oxidative Dimerization of Methane over a Lithium-Promoted Magnesium Oxide Catalyst. *J. Am. Chem. Soc* **1985**, *107*, 5062–5068.

[156] Ueda, W.; Kuwabara, T.; Ohshida, T.; Morikawa, Y. A low-pressure guerbet reaction over magnesium oxide catalyst. *J. Chem. Soc., Chem. Commun.* **1990**, 1558–1559.

[157] Kumar, D.; Reddy, V. B.; Mishra, B. G.; Rana, R.; Nadagouda, M. N.; Varma, R. S. Nanosized magnesium oxide as catalyst for the rapid and green synthesis of substituted 2-amino-2-chromenes. *Tetrahedron* **2007**, *63*, 3093–3097.

[158] Morales, E.; Lunsford, J. H. Oxidative dehydrogenation of ethane over a lithium-promoted magnesium oxide catalyst. *J. Catal.* **1989**, *118*, 255–265.

[159] Smart, R. S. C.; Slager, T. L.; Little, L. H.; Greenler, R. G. Carbon monoxide adsorption on magnesium oxide. *J. Phys. Chem.* **1973**, *77*, 1019–1023.

[160] Valero, R.; Gomes, J. R. B.; Truhlar, D. G.; Illas, F. Good performance of the M06 family of hybrid meta generalized gradient approximation density functionals on a difficult case: CO adsorption on MgO(001). *J. Chem. Phys.* **2008**, *129*, 124710.

[161] Valero, R.; Gomes, J. R. B.; Truhlar, D. G.; Illas, F. Density functional study of CO and NO adsorption on Ni-doped MgO(100). *J. Chem. Phys.* **2010**, *132*, 104701.

[162] Boese, A. D.; Sauer, J. Accurate adsorption energies of small molecules on oxide surfaces: CO-MgO(001). *Phys. Chem. Chem. Phys* **2013**, *15*, 16481–16493.

[163] Alessio, M.; Usvyat, D.; Sauer, J. Chemically Accurate Adsorption Energies: CO and H2O on the MgO(001) Surface. *J. Chem. Theory Comput.* **2019**, *15*, 1329–1344.

[164] Platero, E. E.; Scarano, D.; Spoto, G.; Zecchina, A. Dipole coupling and chemical shifts of CO and NO adsorbed on oxides and halides with rock-salt structure. *Faraday Discuss.* **1985**, *80*, 183–193.

[165] Wichtendahl, R.; Rodriguez-Rodrigo, M.; Härtel, U.; Kuhlenbeck, H.; Freund, H.-J. Thermodesorption of CO and NO from Vacuum-Cleaved NiO(100) and MgO(100). *physica status solidi (a)* **1999**, *173*, 93–100.

[166] Dohnálek, Z.; Kimmel, G. A.; Joyce, S. A.; Ayotte, P.; Smith, R. S.; Kay, B. D. Physisorption of CO on the MgO(100) Surface. *J. Phys. Chem. B* **2001**, *105*, 3747–3751.

[167] Xu, Y.; Li, J.; Zhang, Y.; Chen, W. CO adsorption on MgO(001) surface with oxygen vacancy and its low-coordinated surface sites: embedded cluster model density functional study employing charge self-consistent technique. *Surf. Sci* **2003**, *525*, 13–23.

[168] Spoto, G.; Gribov, E. N.; Ricchiardi, G.; Damin, A.; Scarano, D.; Bordiga, S.; Lamberti, C.; Zecchina, A. Carbon monoxide MgO from dispersed solids to single crystals: a review and new advances. *Prog. Surf. Sci.* **2004**, *76*, 71–146.

[169] Staemmler, V. Method of Local Increments for the Calculation of Adsorption Energies of Atoms and Small Molecules on Solid Surfaces. 2. CO/MgO(001). *J. Phys. Chem. A* **2011**, *115*, 7153–7160.

[170] Kristyán, S.; Pulay, P. Can (semi)local density functional theory account for the London dispersion forces? *Chem. Phys. Lett.* **1994**, *229*, 175–180.

[171] Wu, X.; Vargas, M. C.; Nayak, S.; Lotrich, V.; Scoles, G. Towards extending the applicability of density functional theory to weakly bound systems. *J. Chem. Phys.* **2001**, *115*, 8748–8757.

[172] Wesolowski, T. A.; Morgantini, P.-Y.; Weber, J. Intermolecular interaction energies from the total energy bifunctional: A case study of carbazole complexes. *J. Chem. Phys.* **2002**, *116*, 6411–6421.

[173] Grimme, S. Accurate description of van der Waals complexes by density functional theory including empirical corrections. *J. Comput. Chem* **2004**, *25*, 1463–1473.

[174] Kerber, T.; Sierka, M.; Sauer, J. Application of semiempirical long-range dispersion corrections to periodic systems in density functional theory. *J. Comput. Chem* **2008**, *29*, 2088–2097.

[175] Grimme, S. Semiempirical GGA-type density functional constructed with a long-range dispersion correction. *J. Comput. Chem* **2006**, *27*, 1787–1799.

[176] Grimme, S.; Huenerbein, R.; Ehrlich, S. On the Importance of the Dispersion Energy for the Thermodynamic Stability of Molecules. *ChemPhysChem* **2011**, *12*, 1258–1261.

[177] Tkatchenko, A.; Scheffler, M. Accurate Molecular Van Der Waals Interactions from Ground-State Electron Density and Free-Atom Reference Data. *Phys. Rev. Lett* **2009**, *102*, 73005.

[178] Hirata, S.; Podeszwa, R.; Tobita, M.; Bartlett, R. J. Coupled-cluster singles and doubles for extended systems. *J. Chem. Phys.* **2004**, *120*, 2581–2592.

[179] Booth, G. H.; Grüneis, A.; Kresse, G.; Alavi, A. Towards an exact description of electronic wavefunctions in real solids. *Nature* **2013**, *493*, 365–370.

[180] Jun, Y.; Weifeng, H.; Denis, U.; Devin, M.; Martin, S.; Kin-Lic, C. G. Ab initio determination of the crystalline benzene lattice energy to sub-kilojoule/mole accuracy. *Science* **2014**, *345*, 640–643.

[181] Lau, B. T. G.; Knizia, G.; Berkelbach, T. C. Regional Embedding Enables High-Level Quantum Chemistry for Surf. Sci. *J. Phys. Chem. Lett* **2021**, *12*, 1104–1109.

[182] Chulhai, D. V.; Goodpaster, J. D. Projection-Based Correlated Wave Function in Density Functional Theory Embedding for Periodic Systems. *J. Chem. Theory Comput.* **2018**, *14*, 1928–1942.

[183] Ye, H.-Z.; Berkelbach, T. C. Correlation-Consistent Gaussian Basis Sets for Solids Made Simple. *J. Chem. Theory Comput.* **2022**, *18*, 1595–1606.

[184] Pacchioni, G.; Cogliandro, G.; Bagus, P. S. Characterization of oxide surfaces by infrared spectroscopy of adsorbed carbon monoxide: a theoretical investigation of the frequency shift of CO on MgO and NiO. *Surf. Sci* **1991**, *255*, 344–354.

[185] Neyman, K. M.; Rösch, N. CO bonding and vibrational modes on a perfect MgO(001) surface: LCGTO-LDF model cluster investigation. *Chem. Phys.* **1992**, *168*, 267–280.

[186] Ugliengo, P.; Damin, A. Are dispersive forces relevant for CO adsorption on the MgO(001) surface? *Chem. Phys. Lett.* **2002**, *366*, 683–690.

[187] Nolan, S. J.; Gillan, M. J.; Alfè, D.; Allan, N. L.; Manby, F. R. Calculation of properties of crystalline lithium hydride using correlated wave function theory. *Phys. Rev. B* **2009**, *80*, 165109.

[188] Usvyat, D.; Sadeghian, K.; Maschio, L.; Schütz, M. Geometrical frustration of an argon monolayer adsorbed on the MgO (100) surface: An accurate periodic ab initio study. *Phys. Rev. B* **2012**, *86*, 45412.

[189] Christlmaier, E. M.; Kats, D.; Alavi, A.; Usvyat, D. Full configuration interaction quantum Monte Carlo treatment of fragments embedded in a periodic mean field. *J. Chem. Phys.* **2022**, *156*, 154107.

[190] Georges, A.; Kotliar, G.; Krauth, W.; Rozenberg, M. J. Dynamical Mean-Field Theory of Strongly Correlated Fermion Systems and The Limit of Infinite Dimensions. *Rev. Mod. Phys.* **1996**, *68*, 13–125.

[191] Nusspickel, M.; Booth, G. H. Systematic Improvability in Quantum Embedding for Real Materials. *Phys. Rev. X* **2022**, *12*, 11046.

[192] Faulstich, F. M.; Kim, R.; Cui, Z.-H.; Wen, Z.; Kin-Lic Chan, G.; Lin, L. Pure State v-Representability of Density Matrix Embedding Theory. *J. Chem. Theory Comput.* **2022**, *18*, 851–864.

[193] Mitra, A. pDMET: A Code for Periodic DMET Calculations. 2022; `https://github.com/mitra054/pDMET`, accessed February, 24, 2022.

[194] Beebe, N. H. F.; Linderberg, J. Simplifications in the generation and transformation of two-electron integrals in molecular calculations. *Int. J. Quantum Chem* **1977**, *12*, 683–705.

[195] Vahtras, O.; Almlöf, J.; Feyereisen, M. W. Integral approximations for LCAO-SCF calculations. *Chem. Phys. Lett.* **1993**, *213*, 514–518.

[196] Koch, H.; Sánchez de Merás, A.; Pedersen, T. B. Reduced scaling in electronic structure calculations using Cholesky decompositions. *J. Chem. Phys.* **2003**, *118*, 9481–9484.

[197] Røeggen, I.; Wisløff-Nilssen, E. On the Beebe-Linderberg two-electron integral approximation. *Chem. Phys. Lett.* **1986**, *132*, 154–160.

[198] Hartwigsen, C.; Goedecker, S.; Hutter, J. Relativistic separable dual-space Gaussian pseudopotentials from H to Rn. *Phys. Rev. B* **1998**, *58*, 3641–3662.

[199] Nygren, M. A.; Pettersson, L. G. M.; Barandiarán, Z.; Seijo, L. Bonding between CO and the MgO(001) surface: A modified picture. *J. Chem. Phys.* **1994**, *100*, 2010–2018.

[200] Helgaker, T.; Jørgensen, P.; Olsen, J. *Molecular Electronic-Structure Theory*; 2014; pp 1–908.

[201] Vorwerk, C.; Sheng, N.; Govoni, M.; Huang, B.; Galli, G. Quantum embedding theories to simulate condensed systems on quantum computers. *Nature Computational Science* **2022**, *2*, 424–432.

[202] Muechler, L.; Badrtdinov, D. I.; Hampel, A.; Cano, J.; Rösner, M.; Dreyer, C. E. Quantum embedding methods for correlated excited states of point defects: Case studies and challenges. *Phys. Rev. B* **2022**, *105*, 235104.

[203] Klüner, T.; Govind, N.; Wang, Y. A.; Carter, E. A. Periodic density functional embedding theory for complete active space self-consistent field and configuration interaction calculations: Ground and excited states. *J. Chem. Phys.* **2001**, *116*, 42–54.

[204] Tran, H. K.; Van Voorhis, T.; Thom, A. J. W. Using SCF metadynamics to extend density matrix embedding theory to excited states. *The Journal of Chemical Physics* **2019**, *151*, 34112.

[205] Welborn, M.; Tsuchimochi, T.; Van Voorhis, T. Bootstrap embedding: An internally consistent fragment-based method. *The Journal of Chemical Physics* **2016**, *145*, 74102.

[206] Sharma, P.; Bao, J. J.; Truhlar, D. G.; Gagliardi, L. Multiconfiguration Pair-Density Functional Theory. *Annu. Rev. Phys. Chem.* **2021**, *72*, 541–564.

[207] Gagliardi, L.; Truhlar, D. G.; Li Manni, G.; Carlson, R. K.; Hoyer, C. E.; Bao, J. L. Multiconfiguration Pair-Density Functional Theory: A New Way To Treat Strongly Correlated Systems. *Acc. Chem. Res.* **2017**, *50*, 66–73.

[208] Pandharkar, R.; Hermes, M. R.; Truhlar, D. G.; Gagliardi, L. A New Mixing of Nonlocal Exchange and Nonlocal Correlation with Multiconfiguration Pair-Density Functional Theory. *J. Phys. Chem. Lett.* **2020**, *11*, 10158–10163.

[209] King, D. S.; Hermes, M. R.; Truhlar, D. G.; Gagliardi, L. Large-Scale Benchmarking of Multireference Vertical-Excitation Calculations via Automated Active-Space Selection. *J. Chem. Theory Comput.* **2022**, *18*, 6065–6076.

[210] Yan, Z.; Chinta, S.; Mohamed, A. A.; Fackler, J. P.; Goodman, D. W. The Role of F-Centers in Catalysis by Au Supported on MgO. *J. Am. Chem. Soc.* **2005**, *127*, 1604–1605.

[211] González, R.; Monge, M. A.; Santiuste, J. E. M.; Pareja, R.; Chen, Y.; Kotomin, E.; Kukla, M. M.; Popov, A. I. Photoconversion of F-type centers in thermochemically reduced MgO single crystals. *Phys. Rev. B* **1999**, *59*, 4786–4790.

[212] Rinke, P.; Schleife, A.; Kioupakis, E.; Janotti, A.; Rödl, C.; Bechstedt, F.; Scheffler, M.; Van de Walle, C. G. First-Principles Optical Spectra for F Centers in MgO. *Phys. Rev. Lett.* **2012**, *108*, 126404.

[213] Perdew, J. P.; Ernzerhof, M.; Burke, K. Rationale for mixing exact exchange with density functional approximations. *J. Chem. Phys.* **1996**, *105*, 9982–9985.

[214] Cui, Z.-H.; Zhai, H.; Zhang, X.; Chan, G. K.-L. Systematic electronic structure in the cuprate parent state from quantum many-body simulations. *Science* **2022**, *377*, 1192–1198.

[215] Hermes, M. R. mrh: GPL research code of Matthew R. Hermes. 2018; `https://github.com/MatthewRHermes/mrh`, accessed December, 13, 2023.

[216] Domínguez-Ariza, D.; Sousa, C.; Illas, F.; Ricci, D.; Pacchioni, G. Ground- and excited-state properties of M-center oxygen vacancy aggregates in the bulk and surface of MgO. *Phys. Rev. B* **2003**, *68*, 54101.

[217] White, S. R. Density matrix formulation for quantum renormalization groups. *Phys. Rev. Lett.* **1992**, *69*, 2863–2866.

[218] Chan, G. K.-L.; Head-Gordon, M. Highly correlated calculations with a polynomial cost algorithm: A study of the density matrix renormalization group. *J. Chem. Phys.* **2002**, *116*, 4462–4476.

[219] Stein, C. J.; Reiher, M. autoCAS: A Program for Fully Automated Multiconfigurational Calculations. *J. Comput. Chem.* **2019**, *40*, 2216–2226.

[220] Li, J.; Otten, M.; Holmes, A. A.; Sharma, S.; Umrigar, C. J. Fast semistochastic heat-bath configuration interaction. *J. Chem. Phys* **2018**, *149*, 214110.

[221] Li, J.; Yao, Y.; Holmes, A. A.; Otten, M.; Sun, Q.; Sharma, S.; Umrigar, C. Accurate many-body electronic structure near the basis set limit: Application to the chromium dimer. *Phys. Rev. Res.* **2020**, *2*, 012015.

[222] Tubman, N. M.; Lee, J.; Takeshita, T. Y.; Head-Gordon, M.; Whaley, K. B. A deterministic alternative to the full configuration interaction quantum Monte Carlo method. *J. Chem. Phys.* **2016**, *145*, 044112.

[223] Tubman, N. M.; Freeman, C. D.; Levine, D. S.; Hait, D.; Head-Gordon, M.; Whaley, K. B. Modern Approaches to Exact Diagonalization and Selected Configuration Interaction with the Adaptive Sampling CI Method. *J. Chem. Theory Comput.* **2020**, *16*, 2139–2159.

[224] Booth, G. H.; Thom, A. J. W.; Alavi, A. Fermion Monte Carlo without fixed nodes: A game of life, death, and annihilation in Slater determinant space. *J. Chem. Phys.* **2009**, *131*, 54106.

[225] Mitra, A.; Pham, H. Q.; Pandharkar, R.; Hermes, M. R.; Gagliardi, L. Excited states of crystalline point defects with multireference density matrix embedding theory. *J. Phys. Chem. Lett.* **2021**, *12*, 11688–11694.

[226] Otten, M.; Hermes, M. R.; Pandharkar, R.; Alexeev, Y.; Gray, S. K.; Gagliardi, L. Localized Quantum Chemistry on Quantum Computers. *J. Chem. Theory Comput.* **2022**, *18*, 7205–7217.

[227] Pandharkar, R.; Hermes, M. R.; Cramer, C. J.; Gagliardi, L. Localized Active Space-State Interaction: a Multireference Method for Chemical Insight. *J. Chem. Theory Comput.* **2022**, *18*, 6557–6566.

[228] Bartlett, R. J.; Kucharski, S. A.; Noga, J. Alternative coupled-cluster ansätze II. The unitary coupled-cluster method. *Chem. Phys. Lett.* **1989**, *155*, 133–140.

[229] Taube, A. G.; Bartlett, R. J. New perspectives on unitary coupled-cluster theory. *Int. J. Quantum Chem.* **2006**, *106*, 3393–3401.

[230] Arute, F. et al. Hartree-Fock on a superconducting qubit quantum computer. *Sci.* **2020**, *369*, 1084–1089.

[231] Kim, Y.; Eddins, A.; Anand, S.; Wei, K. X.; van den Berg, E.; Rosenblatt, S.; Nayfeh, H.; Wu, Y.; Zaletel, M.; Temme, K.; Kandala, A. Evidence for the utility of quantum computing before fault tolerance. *Nat.* **2023**, *618*, 500–505.

[232] Yu, H.; Zhao, Y.; Wei, T.-C. Simulating large-size quantum spin chains on cloud-based superconducting quantum computers. *Phys. Rev. Res.* **2023**, *5*.

[233] Chen, E. H.; Zhu, G.-Y.; Verresen, R.; Seif, A.; Bäumer, E.; Layden, D.; Tantivasadakarn, N.; Zhu, G.; Sheldon, S.; Vishwanath, A.; Trebst, S.; Kandala, A. Realizing the Nishimori transition across the error threshold for constant-depth quantum circuits. 2023; `https://arxiv.org/abs/2309.02863`.

[234] Farrell, R. C.; Illa, M.; Ciavarella, A. N.; Savage, M. J. Scalable Circuits for Preparing Ground States on Digital Quantum Computers: The Schwinger Model Vacuum on 100 Qubits. 2023; `https://arxiv.org/abs/2308.04481`.

[235] Shtanko, O.; Wang, D. S.; Zhang, H.; Harle, N.; Seif, A.; Movassagh, R.; Minev, Z. Uncovering Local Integrability in Quantum Many-Body Dynamics. 2023; `https://arxiv.org/abs/2307.07552`.

[236] Yu, H.; Zhao, Y.; Wei, T.-C. Simulating large-size quantum spin chains on cloud-based superconducting quantum computers. *Phys. Rev. Res.* **2023**, *5*, 013183.

[237] Lee, J.; Huggins, W. J.; Head-Gordon, M.; Whaley, K. B. Generalized Unitary Coupled Cluster Wave functions for Quantum Computation. *J. Chem. Theory Comput.* **2018**, *15*, 311–324.

[238] Hoffmann, M. R.; Simons, J. A unitary multiconfigurational coupled-cluster method: Theory and applications. *J. Chem. Phys.* **1988**, *88*, 993–1002.

[239] McArdle, S.; Endo, S.; Aspuru-Guzik, A.; Benjamin, S. C.; Yuan, X. Quantum computational chemistry. *Rev. Mod. Phys.* **2020**, *92*, 015003.

[240] Kandala, A.; Mezzacapo, A.; Temme, K.; Takita, M.; Brink, M.; Chow, J. M.; Gambetta, J. M. Hardware-efficient variational quantum eigensolver for small molecules and quantum magnets. *Nat.* **2017**, *549*, 242–246.

[241] Grimsley, H. R.; Economou, S. E.; Barnes, E.; Mayhall, N. J. An adaptive variational algorithm for exact molecular simulations on a quantum computer. *Nat. Commun.* **2019**, *10*, 3007.

[242] Tang, H. L.; Shkolnikov, V.; Barron, G. S.; Grimsley, H. R.; Mayhall, N. J.; Barnes, E.; Economou, S. E. Qubit-ADAPT-VQE: An Adaptive Algorithm for Constructing Hardware-Efficient Ansätze on a Quantum Processor. *PRX Quantum* **2021**, *2*, 020310.

[243] Ryabinkin, I. G.; Lang, R. A.; Genin, S. N.; Izmaylov, A. F. Iterative Qubit Coupled Cluster Approach with Efficient Screening of Generators. *J. Chem. Theory Comput.* **2020**, *16*, 1055–1063.

[244] Ryabinkin, I. G.; Yen, T.-C.; Genin, S. N.; Izmaylov, A. F. Qubit coupled-cluster method: A systematic approach to quantum chemistry on a quantum computer. *J. Chem Theory Comput.* **2018**, *14*, 6317–6326.

[245] Peruzzo, A.; McClean, J.; Shadbolt, P.; Yung, M.-H.; Zhou, X.-Q.; Love, P. J.; Aspuru-Guzik, A.; O'Brien, J. L. A variational eigenvalue solver on a photonic quantum processor. *Nat. Commun.* **2014**, *5*, 4213.

[246] D'Cunha, R.; Otten, M.; Hermes, M. R.; Gagliardi, L.; Gray, S. K. State preparation in quantum algorithms for fragment-based quantum chemistry. *arXiv* **2023**, *abs/2305.18110*.

[247] Fedorov, D. A.; Alexeev, Y.; Gray, S. K.; Otten, M. J. Unitary Selective Coupled-Cluster Method. *Quantum* **2022**, *6*, 1–17.

[248] Ryabinkin, I. G.; Yen, T.-C.; Genin, S. N.; Izmaylov, A. F. Qubit Coupled Cluster Method: A Systematic Approach to Quantum Chemistry on a Quantum Computer. *J. Chem. Theory Comput.* **2018**, *14*, 6317–6326.

[249] Kottmann, J. S.; Anand, A.; Aspuru-Guzik, A. A feasible approach for automatically differentiable unitary coupled-cluster on quantum computers. *Chem. Sci.* **2021**, *12*, 3497–3508.

[250] Lang, R. A.; Ryabinkin, I. G.; Izmaylov, A. F. Unitary Transformation of the Electronic Hamiltonian with an Exact Quadratic Truncation of the Baker-Campbell-Hausdorff Expansion. *J. Chem. Theory Comput.* **2020**, *17*, 66–78.

[251] Mehendale, S. G.; Peng, B.; Govind, N.; Alexeev, Y. Exploring Parameter Redundancy in the Unitary Coupled-Cluster Ansätze for Hybrid Variational Quantum Computing. *J. Phys. Chem. A* **2023**, *127*, 4526–4537.

[252] Sim, S.; Romero, J.; Gonthier, J. F.; Kunitsa, A. A. Adaptive pruning-based optimization of parameterized quantum circuits. *Quantum Sci. Technol.* **2021**, *6*, 025019.

[253] Halder, D.; Mondal, D.; Maitra, R. Noise-independent route toward the genesis of a COMPACT ansatz for molecular energetics: A dynamic approach. *J. Chem. Phys.* **2024**, *160*, 124104.

[254] Qiskit: An Open-source Framework for Quantum Computing. `https://qiskit.org/`, Accessed: 12/13/2023.

[255] Ostmeyer, J. Optimised Trotter decompositions for classical and quantum computing. *J. Phys. A: Math. Theor.* **2023**, *56*, 285303.

[256] Hatano, N.; Suzuki, M. *Lecture Notes in Physics*; Springer Berlin Heidelberg, 2005; p 37–68.

[257] Fradkin, E. Jordan-Wigner transformation for quantum-spin systems in two dimensions and fractional statistics. *Phys. Rev. Lett.* **1989**, *63*, 322–325.

[258] BROYDEN, C. G. The Convergence of a Class of Double-rank Minimization Algorithms 1. General Considerations. *IMA J. Appl. Math* **1970**, *6*, 76–90.

[259] Fletcher, R. A new approach to variable metric algorithms. *Comput. J.* **1970**, *13*, 317–322.

[260] Goldfarb, D. A family of variable-metric methods derived by variational means. *Math. Comp.* **1970**, *24*, 23–26.

[261] Shanno, D. F. Conditioning of quasi-Newton methods for function minimization. *Math. Comp.* **1970**, *24*, 647–656.

[262] Hermes, M. R.; Pandharkar, R.; Gagliardi, L. Variational Localized Active Space Self-Consistent Field Method. *J. Chem. Theory Comput.* **2020**, *16*, 4923–4937.

[263] Mitra, A. LAS-USCC: A code to perform localized active space unitary selected coupled cluster calculations. 2023; `https://github.com/mitra054/LAS-USCC`, accessed January, 29, 2024.

[264] Kong, L.; Nooijen, M.; Mukherjee, D. An algebraic proof of generalized Wick theorem. *J. Chem. Phys.* **2010**, *132*, 234107.

[265] Yamaguchi, K.; Takahara, Y.; Fueno, T. In *Applied Quantum Chemistry*; Smith, V. H., Schaefer, H. F., Morokuma, K., Eds.; Springer: Berlin, 1986; pp 155–184.

[266] Weigend, F.; Ahlrichs, R. Balanced basis sets of split valence, triple zeta valence and quadruple zeta valence quality for H to Rn: Design and assessment of accuracy. *Phys. Chem. Chem. Phys.* **2005**, *7*, 3297–3305.

[267] Magoulas, I.; Evangelista, F. A. CNOT-Efficient Circuits for Arbitrary Rank Many-Body Fermionic and Qubit Excitations. *J. Chem. Theory Comput.* **2023**, *19*, 822–836.

[268] Burton, H. G. A.; Marti-Dafcik, D.; Tew, D. P.; Wales, D. J. Exact electronic states with shallow quantum circuits from global optimisation. *npj Quantum Inf.* **2023**, *9*, 75.

[269] Lemonick, S. Uranium Dimer Loses a Bond. *C&EN Global Enterprise* **2018**, *96*, 9–9.

[270] Ho, J.; Ervin, K. M.; Lineberger, W. C. Photoelectron spectroscopy of metal cluster anions: Cu-n, Ag-n, and Au-n. *The Journal of Chemical Physics* **1990**, *93*, 6987–7002.

[271] Roos, B. O. The Complete Active Space Self-Consistent Field Method and its Applications in Electronic Structure Calculations. 1987; http://dx.doi.org/10.1002/9780470142943.ch7.

[272] Andersson, K.; Malmqvist, P. A.; Roos, B. O.; Sadlej, A. J.; Wolinski, K. Second-order perturbation theory with a CASSCF reference function. *The Journal of Physical Chemistry* **1990**, *94*, 5483–5488.

[273] Finley, J.; Malmqvist, P.-Å.; Roos, B. O.; Serrano-Andrés, L. The multi-state CASPT2 method. *Chemical Physics Letters* **1998**, *288*, 299–306.

[274] Fdez. Galván, I. et al. OpenMolcas: From Source Code to Insight. *Journal of Chemical Theory and Computation* **2019**, *15*, 5925–5964.

[275] Douglas, M.; Kroll, N. M. Quantum Electrodynamical Corrections to the Fine Structure of Helium. *Annals of Physics (New York)* **1974**, *82*, 89–155.

[276] Hess, B. A. Relativistic Electronic-Structure Calculations Employing a Two-Component No-Pair Formalism with External-Field Projection Operators. *Physical Review A* **1986**, *33*, 3742–3748.

[277] Heß, B. A.; Marian, C. M.; Wahlgren, U.; Gropen, O. A Mean-Field Spin-Orbit Method Applicable to Correlated Wavefunctions. *Chemical Physics Letters* **1996**, *251*, 365–371.

[278] Malmqvist, P. A.; Roos, B. O.; Schimmelpfennig, B. The Restricted Active Space (RAS) State Interaction Approach with Spin-Orbit Coupling. *Chemical Physics Letters* **2002**, *357*, 230–240.

[279] Almlöf, J.; Taylor, P. R. General Contraction of Gaussian Basis Sets. I. Atomic Natural Orbitals for First- and Second-Row Atoms. *Journal of Chemical Physics* **1987**, *86*, 4070–4077.

[280] Ghigo, G.; Roos, B. O.; Malmqvist, P. A. A Modified Definition of the Zeroth-Order Hamiltonian in Multiconfigurational Perturbation Theory (CASPT2). *Chemical Physics Letters* **2004**, *396*, 142–149.

[281] Gorokhov, L. N.; Emelyanov, A. M.; Khodeev, Y. S. Mass-Spectroscopic Investigation of Stability of Gaseous Molecules of U2O2 and U2. *High Temperature* **1974**, *12*, 1156–1158.

[282] Heaven, M. C.; Barker, B. J.; Antonov, I. O. Spectroscopy and Structure of the Simplest Actinide Bonds. *Journal of Physical Chemistry A* **2014**, *118*, 10867–10881.

[283] Devienne, F. M.; Combarieu, R.; Teisseire, M. Action of Different Gases, Specially Nitrogen, on the Formation of Uranium Clusters; Comparison with Niobium and Tantalum Clusters. *Surface Science* **1981**, *106*, 204–211.

[284] Lu, Y. J.; Lehman, J. H.; Lineberger, W. C. A Versatile, Pulsed Anion Source Utilizing Plasma-Entrainment: Characterization and Applications. *Journal of Chemical Physics* **2015**, *142*, 044201.

[285] Ciborowski, S. M.; Liu, G.; Blankenhorn, M.; Harris, R. M.; Marshall, M. A.; Zhu, Z.; Bowen, K. H.; Peterson, K. A. The Electron Affinity of the Uranium Atom. *Journal of Chemical Physics* **2021**, *154*, 224307.

[286] Liu, G.; Ciborowski, S. M.; Bowen, K. H. Photoelectron Spectroscopic and Computational Study of Pyridine-Ligated Gold Cluster Anions. *Journal of Physical Chemistry A* **2017**, *121*, 5817–5822.

[287] Angeli, C.; Borini, S.; Cestari, M.; Cimiraglia, R. A quasidegenerate formulation of the second order N-electron valence state perturbation theory approach. *J. Chem. Phys.* **2004**, *121*, 4043–4049.

[288] Hennefarth, M. R.; Hermes, M. R.; Truhlar, D. G.; Gagliardi, L. Linearized Pair-Density Functional Theory. *J. Chem. Theory Comput.* **2023**, *19*, 3172–3183.

[289] Hennefarth, M. R.; King, D. S.; Gagliardi, L. Linearized pair-density functional theory for vertical excitation energies. *J. Chem. Theory Comput.* **2023**, *19*, 7983–7988.